Internal Wave Drift of a Neutrally Buoyant Sphere

by

A thesis submitted to the

School of Graduate Studies

in partial fulfilment of the

requirements for the degree of

Master of *Science*

Department of *Physics and Physical Oceanography*

Memorial University of Newfoundland

May 2014

St. John's Newfoundland

Abstract

We studied the motion of neutrally buoyant spheres induced by internal waves in a linearly stratified fluid with moderate Reynolds numbers (200-300). The characteristic scale of the sphere is much smaller than the wavelength ($D/\lambda < 0.05$), so we apply Morison's equation, which is a semi-empirical formula to estimate the force on underwater structures, to model the drag force and motion of the sphere. In our 5-metre long wave tank, a mode-1 internal wave was generated by a wave generator to study the motion of the spheres. Experimental results show that, similar to surface waves, there exists a wave induced drift of the sphere resulting from the phase lag between the motion of the sphere and the fluid. The magnitude and direction of the drift velocity u_d can be affected by many parameters, including the initial phase of the wave generator, depth of the sphere, and frequency of the internal waves. An empirical formula for u_d will be introduced and will be compared to the theoretical results from a numerical simulation. For the vertical motion of the sphere, both the experiment and numerical simulation show that at low frequency of the internal waves ($\omega/N < 0.2$), a series of harmonics of ω appear in the vertical motion.

Acknowledgements

Thanks to my farther and mother for their support during my study far from home. Special thanks to my supervisor James Munroe for the support and supervising. I've learned a lot from him. Thanks to Professor Entcho Demirov, Professor Yakov Afanassiev, Prajvala Kurtakoti, Yang Zhang, Yi Sui for the advice and help. And to all the graduate students and faulty members and staff, thanks for their help and suggestions!

"This work was funded by a Research Development Corporation of Newfoundland an Labrador Ignite Research and Development grant"

Contents

List of Tables

List of Figures

Chapter 1

Introduction

1.1 Stratified Fluid

Most fluids in our daily life are homogeneous with uniform density, but a stratified fluid is the one that density changes with depth. In stratified fluids, many physical processes can be different, such as waves.

The main reason for density stratification in the ocean are changes in temperature and salinity. Stratification could be caused by either one of these or both. Typically, the top few tens of metres are uniform in density. Beneath this mixed layer is a strongly stratified region called the pycnocline. A similar structure can occur in lakes where temperature alone controls the density. Below several hundred meters, the ocean is weakly stratified. Density changes with depth allow water parcels to perform vertical oscillations in the fluid due to variable buoyancy forces. This makes the motion in a stratified fluid much different than in homogeneous fluid.

1.2 Internal Gravity Waves

Surface waves in a homogeneous fluid are commonly observed. Internal gravity waves, or simply internal waves, are different from what we are familiar with. Internal waves are baroclinic waves that exist in stratified fluid and are hard to observe in our daily life. Baroclinic means the gradient of pressure and the gradient of density are not aligned. The restoring force of internal waves is the reduced gravity, which means the net force of gravity and buoyancy. Internal waves in the ocean usually have large amplitudes and long periods.

1.2.1 Internal Wave Equations

1.2.1.1 Derivation of the Equations

The internal wave equation can be derived from the basic equations of fluid dynamics based on some assumptions. We will assume the fluid to be incompressible and inviscid. The fluid also satisfies the Boussinesq approximation, which means the mean density could be described as the background density plus a variation

$$\rho = \rho_0 + \bar{\rho}(z) \tag{1.1}$$

where ρ_0 is the characteristic density and $\bar{\rho}(z)$ is the density variation with depth, where $\bar{\rho}(z) \ll \rho_0$.

The momentum, conservation of internal energy and mass equations [Sutherland, 2010] are

$$\rho_0 \frac{Du}{Dt} = -\frac{\partial p}{\partial x} \tag{1.2}$$

$$\rho_0 \frac{Dw}{Dt} = -\frac{\partial p}{\partial z} - \rho g \tag{1.3}$$

$$\frac{D\rho}{Dt} = -w\frac{d\bar{\rho}}{dz} \tag{1.4}$$

$$\bigtriangledown \cdot \vec{u} = 0 \tag{1.5}$$

The $\frac{D}{Dt}$ symbol means the material derivative which expands to $\frac{D}{Dt} = \frac{\partial}{\partial t} + \vec{u} \cdot \bigtriangledown$. For small amplitude motions, we can linearize the equations, neglect non-linear terms and get:

$$\rho_0 \frac{\partial u}{\partial t} = -\frac{\partial p}{\partial x} \tag{1.6}$$

$$\rho_0 \frac{\partial w}{\partial t} = -\frac{\partial p}{\partial z} - \rho g \tag{1.7}$$

$$\frac{\partial \rho}{\partial t} = -w\frac{d\bar{\rho}}{\partial z} \tag{1.8}$$

$$\bigtriangledown \cdot \vec{u} = 0 \tag{1.9}$$

Combine the four equations above, eliminate pressure from them and bring in the streamfunction ψ :

$$\frac{\partial \psi}{\partial z} = -u, \quad \frac{\partial \psi}{\partial x} = w \tag{1.10}$$

Finally through rearrangement we can get the internal wave equation expressed by the streamfunction as

$$\frac{\partial^2}{\partial t^2}(\nabla^2 \psi) + (-\frac{g}{\rho_0}\frac{d\bar{\rho}}{dz})\psi_{xx} = 0 \tag{1.11}$$

1.2.1.2 Buoyancy Frequency

Now we introduce the buoyancy frequency, also known as the Brunt-Väisälä frequency, N, from equation (1.11) where ρ_0 is the background density, g is the gravity acceleration, and $\bar{\rho}$ is the density variation. It can be understood as the angular frequency of a water parcel which naturally oscillates vertically in a stratified fluid. The expression

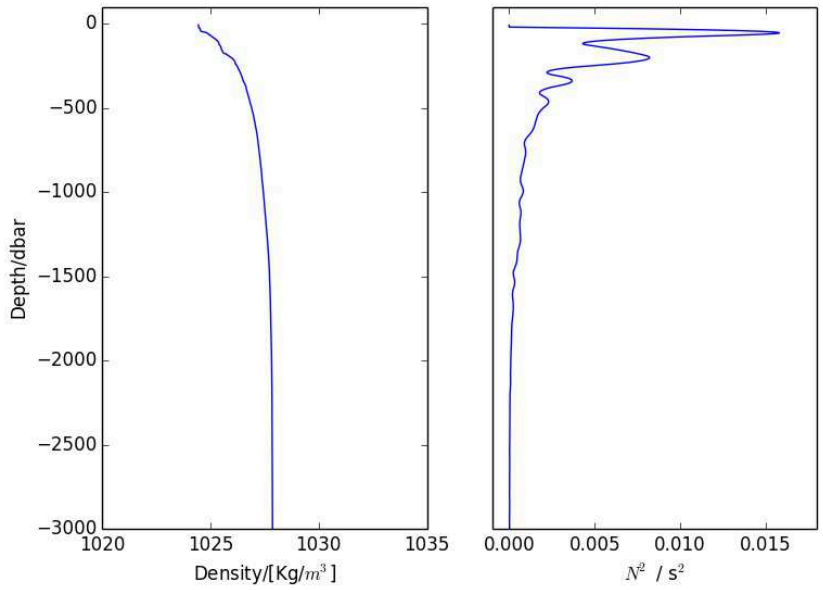

Figure 1.1: Density and Buoyancy frequency square, N^2, in the ocean [Talley, 2011]

of buoyancy frequency square is

$$N^2 = -\frac{g}{\rho_0}\frac{\partial \bar{\rho}}{\partial z} \tag{1.12}$$

From the expression, we can see that N^2 represents the stability of the stratification, if $N^2 < 0$ heavy fluid is over light fluid, which means the fluid unstable. If $N^2 > 0$ means stable stratification. For non-linear stratification, the buoyancy frequency also could be a function of depth written as $N(z)$.

We can replace $(-\frac{g}{\rho_0}\frac{d\bar{\rho}}{dz})$ with N^2 and get the simpler equation:

$$\frac{\partial^2}{\partial t^2}(\nabla^2\psi) + N^2\psi_{xx} = 0 \tag{1.13}$$

Figure 1.1 shows the density and buoyancy frequency as a function of depth in the Pacific ocean [Talley, 2011]. As can be seen from the figure, the density is strongly stratified within the first 200 meters below the surface and is nonlinear. But after

reaching a depth of about 350 meters deep the stratification become weak and density increases linearly with depth.

1.2.1.3 Dispersion Relation

We look for a wavelike solution for 2D internal waves of the form $\psi = Ae^{i(k_x x + k_z z - \omega t)}$, where ω, k_x and k_z represents the frequency of the wave and the horizontal and vertical wavevector of the wave. Substituting ψ into the internal wave equation (1.13), we can get the dispersion relation as:

$$\omega^2 = N^2 \frac{k_x^2}{k_x^2 + k_z^2} \tag{1.14}$$

This shows the relation of the frequency of the internal wave and wave numbers. For a fixed frequency, a wave can only have phase lines with a certain angle $\theta = \tan^{-1}(\frac{k_z}{k_x})$ and we have another expression for the dispersion relation [Sutherland, 2010]:

$$\omega = N \cos\theta \tag{1.15}$$

From equation (1.15), we can see that for an internal wave freely propagating in a stratified fluid, the frequency of the wave must not exceed the buoyancy frequency. The magnitude of horizontal and vertical wavevector k_x and k_z also related by the dispersion relation as:

$$k_z^2 = k_x^2(\frac{N_0^2}{\omega^2} - 1) = k_x^2 \tan^2\theta \tag{1.16}$$

Through the dispersion relation, we can find phase velocity $\vec{c_p}$ and group velocity of the $\vec{c_g}$ of the internal wave as well. If we use $\vec{k}$ to represent the total wave vector, the magnitude of $\vec{k}$ is $k = \sqrt{k_x^2 + k_z^2}$, the phase velocity is

$$\vec{c_p} = \frac{\omega}{k}\frac{\vec{k}}{|\vec{k}|} = sign(k_x)\frac{Nk_x}{|k|^3}(\vec{k_x}, \vec{k_z}) \tag{1.17}$$

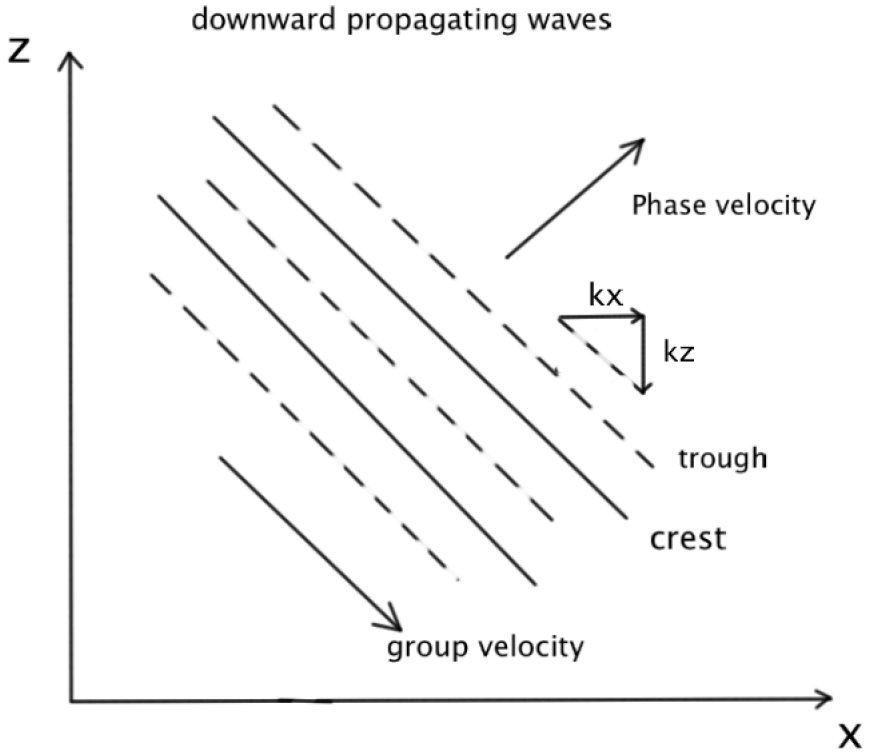

Figure 1.2: Vertical structure of internal waves

and the group velocity is

$$\vec{c_g} = \nabla_k \omega = (\frac{\partial \omega}{\partial k_x}, \frac{\partial \omega}{\partial k_x}) = \frac{N k_z}{|k|^3}(\vec{k_z}, -\vec{k_x}) \tag{1.18}$$

Through equations above, we can see that $\vec{c_p} \cdot \vec{c_g} = 0$, which means they are perpendicular to each other. The direction of those velocities determines the propagating direction of the internal wave.

Figure 1.2 shows the vertical structure of a downward propagating internal wave. The angle of propagation is given by equation (1.15). We can see how the wave propagates and the phase changes in a wave packet. Even though the lines of constant phase move up and to the right, the wave packet as a whole (i.e. the energy) moves

down and to the right.

1.2.1.4 Wave Modes

If we bound an internal wave in a 2D rectangular domain with $0 \leq z \leq H$ and $0 \leq x \leq L$, we can have wave modes. The no normal-flow condition requires that the vertical velocity $w = 0$ at the upper and lower boundaries and the horizontal velocity $u = 0$ at left and right boundaries. To express this with the streamfunction $\psi(x, z, t)$ [Sutherland, 2010], we should write:

$$\psi(x, 0, t) = \psi(x, H, t) = 0 \quad 0 \leq x \leq L, t > 0 \tag{1.19}$$

$$\psi(0, z, t) = \psi(L, z, t) = 0 \quad 0 \leq z \leq H, t > 0 \tag{1.20}$$

which means ψ is constant along all the boundaries. Substitute these boundary conditions to the internal wave equation (1.13), and still assume there are wave like solutions $Ae^{i(k_x x + k_z z - \omega t)}$ and substitute into equation (1.13). Unlike an unbounded domain, the existence of boundary conditions restrict the allowable internal waves that can occur in this domain: "only the superposition of left-right and up-down propagating waves with fixed nodes at the boundaries."[Sutherland, 2010] This means only waves with certain wave vectors can exist in the domain. The streamfunction could be written as:

$$\psi(x, z, t) = \sum_{i=1}^{\infty} \sum_{j=1}^{\infty} A_{ij} \sin(ik_{x0}x) \sin(jk_{z0}z) e^{-i\omega t} \tag{1.21}$$

in which $k_{x0} = \pi/L$ and $k_{z0} = \pi/H$ represents the basic wave number (longest wavelength), and $i, j = 1, 2, 3, ...$ A_{ij} is the amplitude of streamfunction for $i - j$th

mode. And through the dispersion relation we can find the frequency by:

$$\omega_{ij} = N_0[1 + (\frac{jL}{iH})^2]^{-\frac{1}{2}} \quad i, j = 1, 2, 3, ... \tag{1.22}$$

Wave modes are important because in our lab the tank we use is a rectangular box as described above, with a wave generator on the left side of the tank. Most of our experiments are carried out in a mode-1 internal wave field.

1.2.2 Internal Waves in the Ocean

The ocean is a naturally stratified system, where multiple types of waves exist, including internal waves. Diving through tens of meters of mixed layer, we will reach the thermocline, which is strongly stratified in the ocean with a buoyancy frequency of $N = 0.01\text{s}^{-1}$[Wunsch and Ferrari, 2004]. A few hundreds of meters below the surface is the abyss, where the stratification is weaker than the thermocline. The buoyancy frequency can be as small as $N = 10^{-4}\text{s}^{-1}$ [Wunsch and Ferrari, 2004] in the abyss which means the period of one oscillation can be a few hours.

Internal waves in the ocean can be generated by many sources such as surface waves or tidal flow over topography. Vertical displacement of the water parcels can be tens of meters typically with the time scale from tens of minutes to hours. The horizontal displacement of internal waves could be as long as a kilometer with a current speed at 0.5 ms^{-1} [Garrett and Munk, 1979]. As the earth is rotating, for waves having periods exceeding tens of hours the rotation effects are important [Sutherland, 2010]. Using the Coriolis frequency $f = 2\Omega \sin(\phi)$ [Garrett and Munk, 1979], where Ω is the earth rotation angular velocity and ϕ is the latitude, the dispersion relation will change to a combination of the vertical and horizontal structure [Garrett and

Munk, 1979]:

$$\omega^2 = N^2 \cos^2\theta + f^2 \sin^2\theta \tag{1.23}$$

The limit for an internal waves to exist in the ocean is $f \leq \omega \leq N$. When ω is slightly greater than f, the motion of water particles will tend to be closer to horizontal and circular, and if ω is close to N, the water particles tend to move more vertically and the trace would be more elliptical.

The stratification is non-uniform in the ocean, a downward propagating internal wave with frequency ω may encounter an interface where $\omega > N$, the wave will experience a reflection [Garrett and Munk, 1979]. Combined with the reflection at a upper interface with $\omega > N$, there will be two vertical boundaries of the internal waves which means there would be wave modes in the ocean as well.

The dissipation of internal waves is usually due to the shear instability, which mainly caused by the superposition of different waves making the local Richardson number $N^2/(\frac{\partial u}{\partial z})^2$ down below $\frac{1}{4}$ [Sutherland, 2010]. The breaking internal waves will cause mixing and lose energy and finally dissipate. It is an open research question to determine what fraction of internal wave energy results in diapycnal mixing [Ivey and Koseff, 2008].

1.3 Autonomous Underwater Vehicles

Autonomous underwater vehicles are robots that travel underwater with limited human control during a mission. AUVs, as is type of unmanned underwater vehicles, are different from those non-autonomous remotely controlled underwater vehicles called ROVs. ROVs require cables from a surface ship and only conduct missions in a lim-

ited area. The first AUV was developed at the Applied Physics Laboratory at the University of Washington at 1957 and was named 'Special Purpose Underwater Research Vehicle'. It was mostly used for the study of diffusion, acoustic transmission and submarine wakes [Mark Sibenac and Thomas, 2004]. Some other institutes also developed some early AUVs, such as MIT in the 1970s and in the Soviet Union. At that time, AUVs were mainly produced for military use [Mark Sibenac and Thomas, 2004].

Today, many types of AUVs have been designed, from the underwater gliders to the tons heavy deep water AUVs. Large AUVs such as Sentry from Woods Hole Oceanographic Institute, whose dimensions are $290 \times 220 \times 180$ CM^3, weigh about 1250 Kg, is able to dive to 4500 meters with various scientific sensors. The REMUS 100 represents the typical small size AUVs which is about 19 CM in diameter and about 37 Kg in mass, having a maximum operation depth of 100 M. Launching and recycling REMUS could be a one person job, to reduce cost. AUVs, usually are equipped with various modules to deal with different underwater environments. They have onboard batteries, computing systems, control systems and dynamic systems. With the pre-programmed mission system, AUVs are able to report and adapt their routine instantly. The development of battery technology allows AUVs to fly in the ocean for many months.

AUVs are becoming a very effective tool in ocean research scientifically and commercially with developing manufacture technology and decreasing cost. For instance, the oil and gas industry are using AUVs to map the seafloor to detect mineral resources before the construction of a platform. AUVs are still active in the military area, which usually are employed in anti-submarine warfare, and to aid in the detec-

tion of submarines [B.Curtin, 2005]. Sensors equipped with AUVs are able to collect data of the ocean current and flow of the local area. They have potential to be a very effective underwater technology in the frontier of physical oceanography and geophysics for various scales of surveys and projects.

Different types of gliders also have been designed for long term use [B.Curtin, 2005]. These gliders are able to travel with minimum power during a mission. The feature will be of great benefit if we need to collect data for a very long time in the ocean.

1.3.1 Equations of simplified AUV Models

An AUV model is a mathematical simulation of AUV motion in fluid for both engineering and science. Such models are found useful in testing and improving vehicle performance.

1.3.1.1 3-DOF Equations

Usually a 6-DOF (degrees of freedom) model will be used to describe the AUV motion, but for our simplification of the derivation, we will introduce a 3-DOF model for simplicity. More details on the 6-DOF equations are included in Appendix A.1. As an AUV has a certain shape, the orientation will contribute to the hydrodynamics of the vehicle, so the system equations are usually derived and solved in 2-sets of coordinate systems: the earth-fixed coordinate system (X-Y-Z) and the vehicle body fixed coordinate system (x-y-z). Newton's 2nd law for translational motion and Euler's law for rotation are written in the body-fixed coordinate and are transformed into the inertial coordinate system in the 3-DOF situation. The system contains various

forces and torques from each part of the vehicle, so some simplifying assumptions are made. In the derivation of the equations, we consider the classic added mass effect to be included in the inertial mass system and we will discuss later what added mass contribute to the motion of a submerged object.

The AUV geometry (Figure 1.3) we use here is an ellipsoid shaped hull body with control surfaces on both sides of the body within $x-y$ plane. We restrict the motion of the AUV in the $x-z$ plane and neglect the rotation along x axis, thus only the translational motion in x and z direction and the rotational motion along y axis needs to be considered. With the setup above we reduce the 9 equations (including the kinematic relation) down to 3. Forces and torques on the control surface are out of the $x-z$ plane but they still contribute to the motion in the vertical plane.

The system of equations [Nahon, 1996] are:

$$m(\dot{u}+qw) = -(G-B)sin\theta + F_{cx} + F_{hx}, \tag{1.24}$$

$$m(\dot{w}-qu) = -(G-B)cos\theta + F_{cz} + F_{hz}, \tag{1.25}$$

$$I_{yy}\dot{q} = M_{cy} + M_{hy}, \tag{1.26}$$

where u and w represents the velocity along $[x, z]$ axis and q represents the angular velocity around y axis. In the equations above, the first two represent the translational motion and the third one describes the rotation. We assume the center of gravity and buoyancy overlap each other at the same point and we choose that to be the origin point of the vehicle body fixed reference frame. θ is the Euler angle for the rotation along y axis. G and B represents gravity and buoyancy, respectively. $\vec{F_c}$ and $\vec{F_h}$ represents the control forces and the hydrodynamic forces on the vehicle. On the right hand side of the equations are the force and torque terms and on the left

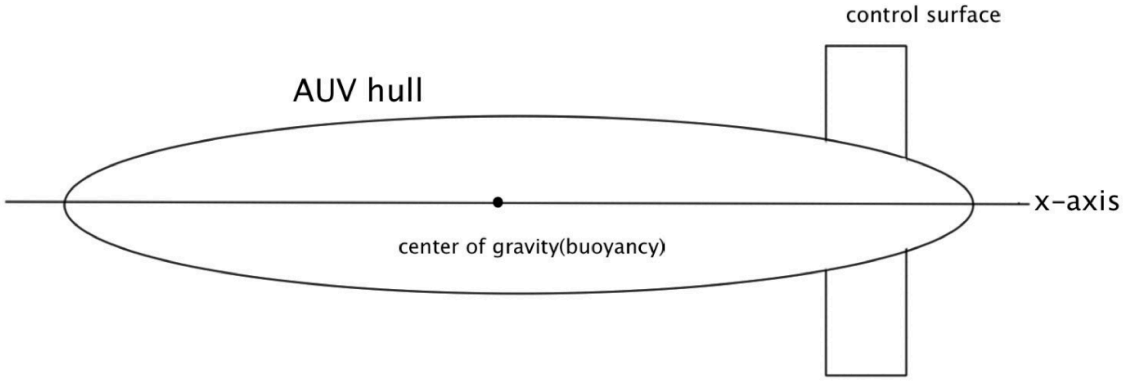

Figure 1.3: AUV schematic used for the motion equation

side are the linear and angular accelerations. These three equations are written in body-fixed reference frame which itself is a rotating reference frame, so the Coriolis terms appear in the translational motion with the form of $+qw$ and $-qu$. To get the spatial information of the vehicle in the inertial-reference coordinate system, we will decompose the velocity vector into X and Z direction in the inertial-reference frame.

The transform equation [Fossen, 2011] is:

$$\begin{bmatrix} U \\ W \\ Q \end{bmatrix} = \begin{bmatrix} \cos\theta & -\sin\theta & 0 \\ \sin\theta & \cos\theta & 0 \\ 0 & 0 & 1 \end{bmatrix} \begin{bmatrix} u \\ w \\ q \end{bmatrix} \tag{1.27}$$

which gives us the expression for the velocity vector $[U, W, Q]$ where U and W are the translational velocities and Q is the angular velocity in the inertial reference frame. By integrating over time we can obtain the spatial and orientation information of the vehicle in the inertial $X - Z$ plane.

1.3.1.2 Hydrodynamic Forces on the Vehicle

Gravity and buoyancy forces on the AUV can be obtained accurately from the features of the AUV, and they are considered to be constant. We also neglect thruster force which is considered as a constant force along x axis in body-fixed coordinates. For the solution in the body-fixed coordinate system, expressions of hydrodynamic forces on the vehicle hull and the control surfaces are essential. It contains drag and lift force when an object is moving in the fluid. The mathematical form of these forces may vary as a function of the Reynolds number and Froude number which are of vital importance. For our system, we introduce a quadratic drag and lift law which has been tested through many experiments for different objects. The general form [Fossen, 2011] of lift L and drag D forces are

$$L = \frac{1}{2}\rho V_r^2 A_f C_L \tag{1.28}$$

$$D = \frac{1}{2}\rho V_r^2 A_f C_D \tag{1.29}$$

for which A_f is the relevant reference area for each part of the vehicle and ρ is the density of the fluid. V_r is the velocity relative to the flow for a rigid shape. C_L and C_D are the lift and drag coefficients which will be different under different conditions.

The lift and drag forces share the same formula but the coefficients are different. Most formula of coefficients here are discussed by Nahon [1996]. For the vehicle geometry, the two control planes are symmetric along x axis which prevent rotation around x axis from happening. These control planes affect the angular velocity of the vehicle.

The lift coefficient of each control plane [Nahon, 1996] is given by the formula:

$$C_L = C_{l\alpha}\frac{a}{a + [2(a+4)/(a+2)]}\alpha \tag{1.30}$$

in which a means the aspect ratio of the plane, $C_{l\alpha}$ is the slope of the 2-D lift curve, and α is the angle of attack of the plane. The aspect ratio used here is usually low (0.4) in the calculation of the lift force on the plane.

The drag coefficient of each plane is estimated [Nahon, 1996] using the formula:

$$C_D = C_{D0} + \frac{C_L^2}{\pi A e} \tag{1.31}$$

We can see from the formula that the drag coefficient has some relationship with the lift coefficient. And from which C_{D0} is the parasite drag coefficient related to the shape and skin friction of the object, e is the Oswald efficiency factor which usually has a value about $0.8 - 0.9$.

The lift and drag coefficients on the AUV hull body [Nahon, 1996] is given by the formula:

$$C_{L\alpha} = \frac{2(k_2 - k_1)S_o}{V_h^{2/3}} \tag{1.32}$$

where $k_2 - k_1$ is an added mass factor related to the shape of the body which will approach 1 if the AUV body is elongated, S_o is the cross section area of the hull, and V_h is the volume of the hull.

The drag coefficient of the hull body is:

$$C_D = C_f[1 + 60(D_h/l_h)^3 + 0.0025 \times (l_h/D_h)] \tag{1.33}$$

where C_f is a function of Reynolds number, and D_h and l_h represent the hull's diameter and length.

With the forces on the vehicle, we can calculate the moment of each force during the motion. As gravity and buoyancy are considered to be at the origin of the body-fixed coordinate system, the moments on the hull body will be zero. To get moments on each control surface, we have to define the reference points of each plane which are usually located at the hydrodynamic center of the plane. The model requires the center (x_i, z_i) information for each plane and the relative velocity V_i of the surrounding flow. These coordinates should be known from the AUV design. The relative velocity is calculated by the equation below from the body-fixed coordinate:

$$V_i = \sqrt{u^2 + (w - qx_i)^2} \tag{1.34}$$

thus we can get the angle of attack [Nahon, 1996] for each control plane:

$$\alpha_i = \tan^{-1} \frac{w - qx_i}{u + qz_i} \tag{1.35}$$

which will be substituted into equation (1.30) to solve for the hydrodynamic force on the plane. The control force of the vehicle comes from the rotation δ_i of the control plane. And this factor should be added to the calculation of the hydrodynamic force on the plane as:

$$\alpha_i' = \alpha_i + \delta_i \tag{1.36}$$

We have a simplified mathematical model for a ellipsoid shaped autonomous underwater vehicle in 2 dimension with 3 degrees of freedom. We can use the equations to model the motion of the vehicle in the fluid.

1.3.1.3 Added Mass

In the discussion above, we included the added mass effect in the inertial mass. In fluid dynamics, added mass is important for marine vehicles because it affects the

motion in the fluid.

If an object is unsteadily moving in fluid, and with acceleration, the fluid parcels around it will also move. This phenomenon is due to friction and drag between fluid parcel and the object body. For vehicle manufacturer, the added effect must be considered in vehicle design.

Added mass coefficients are determined by the geometry and motion of the vehicle and have been investigated and tested for many years. Viscosity is also very important for the added mass effect, and although some research was been done for the added mass effect in stratified fluid [Ermanyuk and Gavrilov, 2003], it need more effort to establish a complete theory about added mass in stratified fluid.

1.3.2 Scale

Scaling is another extremely important factor in fluid dynamics. To get the correct scale parameters is the first step to design our experiments. In the ocean, waves can have wavelengths up to hundreds of meters, while autonomous underwater vehicles are typically only a few meters in length. Compared to most of the waves in the ocean, the size of the vehicles are small compare to the waves. We are going to introduce some dimensionless numbers which are used in the dynamic laws to write our equations.

1.3.2.1 Reynolds Number

Reynolds number (Re) is a dimensionless number which represents the ratio of inertial force to viscous force. For an object moving in a wave field, it determines the form of drag law for the motion. The definition of Reynolds number is [Cushman-Roisin

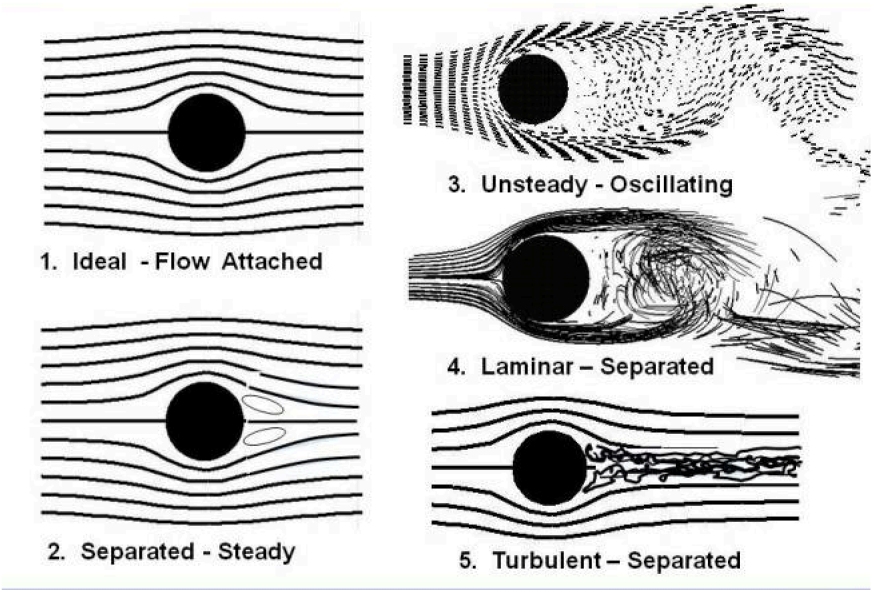

Figure 1.4: Flow past a cylinder with increasing Reynolds Number from 1 to 5 [NASA, 2010]

and Beckers, 2011]:

$$\mathrm{Re} = \frac{\rho v L}{\mu} = \frac{v L}{\nu} \tag{1.37}$$

in which v is the relative velocity of the object to the fluid, L is the characteristic length of the object (for a sphere it will be the diameter), ν is the kinematic viscosity and $\mu = \rho\nu$ is the dynamic viscosity. ρ is the density of the fluid.

For $Re \ll 1$, the flow would be purely laminar, the dynamic force on the object will be just skin friction from the fluid, which means if a small sphere falls in laminar flow, it will reach its terminal velocity (gravity and buoyancy balanced by the skin friction force which usually proportional to the relative velocity as terminal velocity) after a short time after the process begins. When $Re < 0.1$, the drag force on the sphere will be a linear drag which is proportional to the velocity.

For $1 < Re < 10^2$, it will be in a regime where the drag force from the fluid

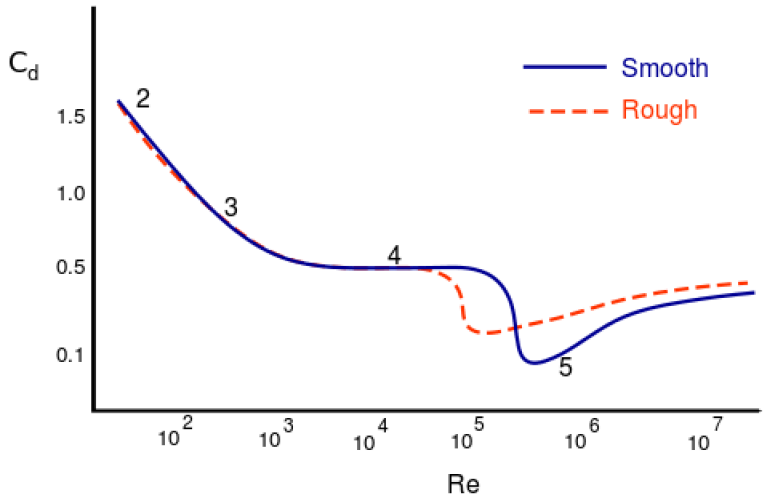

Figure 1.5: The drag coefficient for a sphere as a function of Re for rough and smooth surface [NASA, 2010]

between the linear drag law to a quadratic drag law, the flow around the object (using sphere as an example) is neither purely turbulent nor purely laminar. In this regime, usually we represent the drag law in the form of a quadratic one as:

$$F = \frac{1}{2}\rho C_D A V_r^2 \tag{1.38}$$

which we have introduced for hydrodynamic force on the AUV. In this range, to get a unified formula, we usually set the drag coefficient, C_D, to be a function of Re shown as figure 1.4. For this project, finding the drag coefficient which best describe the scenario is valuable.

For $Re \gg 10^3$, the flow around the object is purely turbulent, and the drag law could be best represented by equation (1.38) with a uniform drag coefficient C_D.

1.3.2.2 Froude Number

The Froude number (Fr), defined as the ratio of the characteristic velocity to the fastest wave speed [Sutherland, 2010]. In a uniformly stratified fluid with depth H, the formula for Froude number would be

$$\mathrm{Fr} = \frac{U_0}{\sqrt{g'H}} = \frac{U_0}{N_0 H} \tag{1.39}$$

where U_0 is the characteristic velocity and g' is the reduced gravity, we suppose the horizontal scale is much longer than the vertical and $c = \sqrt{g'H}$ represents the speed of the wave.

Froude number is a dimensionless number that describes the importance of stratification, also can be understood as the ratio of a body's inertial to gravitational force. For different sizes of object, the same Froude number means they have the same dynamics.

1.3.3 Internal Waves and AUV

If we take all factors into consideration, the marine vehicle motion equation should include the hydrodynamic forces and all the other effects from the environment such as the wind force and the wave force. In the interior of the ocean, internal waves are common waves strongly connected to the energy transportation.

For an AUV travelling underwater during the mission, the vehicle will encounter internal waves with certain amplitude; the amplitude can be hundreds of meters. The interaction between waves and the vehicle is of great interest to us. Waves can change the trajectory of the vehicle and we need to figure out the dynamics of the interaction to predict the vehicle motion in a given internal wave field.

The knowledge for internal wave and AUV interaction still needs to be studied. The wave effect is often simulated as periodical perturbations that have been neglect in homogeneous fluid. But in a stratified fluid, internal waves also have vertical structure.

In most textbooks and research papers, the numerical simulation of AUV in surface waves have been studied a little bit and most of the waves have been treated as mean flows. The internal wave may generate a non-linear flow field and it has a natural system frequency as the buoyancy frequency, which could be the most interesting part.

1.3.3.1 Drift of Floating Objects in Surface Waves

An AUV can be treated as a neutrally buoyant object when it is not travelling in the ocean, and AUV in internal waves can be described as the motion of a neutrally buoyant object in an internal wave field. Before we study the internal wave case, some research already been done on floating objects in surface waves, which similar to our project. Conclusions from surface wave drift problem can be useful in our experiments and numerical simulations.

Stokes drift is a classical phenomena in deep water surface waves, which is caused by the non-linearity of the wave equations. The magnitude of fluid parcels will increase as the fluid gets deeper. If we average the velocity of a fluid parcel over one period, we will get a mean velocity which is the same direction as the phase velocity of the wave. Small sized floating objects also have been studied numerically and experimentally, which is related to the motion of icebergs in the sea. The numerical study of the drift of floating objects have shown that, for the difference in viscosity and the added

mass effect, the motion of the object is different from the fluid parcels [Grotmaack and Meylan, 2006]. The conclusion from numerical models show that the object will have a transient motion due to different initial conditions, and finally the object will drift to the same direction as the Stokes drift. Some recent experimental results have been published by [Huang and Huang, 2011] for different shapes of objects in regular surface waves. The drift of the object is different from the Stokes drift of the fluid parcels. In the experiment, they did not observe the transient process of the object, this is probably because the frequency of the wave is as high as 1 Hz. In the transient process we supposed to see positive drift or negative drift depending on the initial condition of the experiment.

In this thesis, we are going to study the motion of a neutrally buoyant sphere in an internal wave field. Which is the simplified model of an AUV. Chapter 2 is the setup of our experiment and the experimental results. Chapter 3 is the analysis of the experiment data where we discover the drift motion of the sphere. Some numerical study about the motion of the sphere will be presented in Chapter 4. And Chapter 5 is the discussion and conclusion session.

Chapter 2

Experiments and Results

2.1 Apparatus

To study the effect of internal waves on floating objects, laboratory experiments can be used to test the theory. In our laboratory, we have the ability to generate internal waves in a 5 m long and 60 cm deep tank with a wave generator with variable frequencies. Using a technique called synthetic schilieren, we can visualize and measure the internal wave field in the tank.

2.1.1 Tank

The tank we used to run the experiments is $498 \times 45 \times 60$cm (length×width×depth). It is made in three sections and combined together in a aluminum frame with the side walls of transparent acrylic material. The length of the tank ensures a clear view of the propagation of the wave. The tank is divided into two parts along the length direction about 30 cm and 15 cm each in width. The purpose of this is to make the

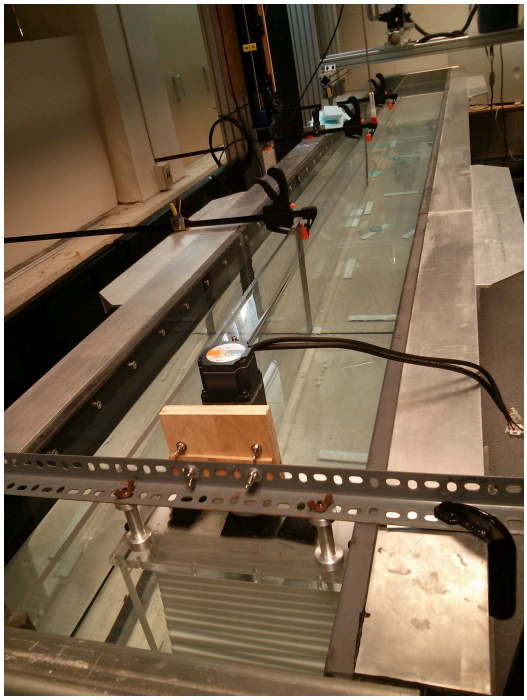

Figure 2.1: The tank we used for the experiments

30cm channel the same width as the wave generator, and have a 2D wave pattern in this channel.

2.1.2 Camera and Lens

The camera used to capture the motion of the fluid and the object in the fluid is a Manta G-125B from Allied Vision Technologies. It is a low cost GigE Vision camera with a Sony ICX445 sensor. The camera can run at 30fps at a resolution of 1000×1000, and capture and transfer data simultaneously. The lens mounted on the camera is HF25SA-1 from Fujinon. It is a high resolution lens (5 megapixel) with a focal length of 25 and a aperture of F1.4. The camera is connected to a Mac Pro through GigE to transfer data. When placed about 2.5 m away, the camera can obtain a vision

Figure 2.2: Camera model Manta G-125B

window about 60 cm × 45 cm (width×height). Almost all of our experimental data are acquired with this camera.

2.1.3 Pumps

The pumps used in our lab are two industrial peristaltic pumps from MasterFlex with model number $7592-40$ which have a angular velocity ranged from 6 rpm to 600 rpm. The pumps can be used with 3 diameters of tubes and have digital motor controllers. Each size of the tubes has a max flow rate. The pumps are capable of running for a long period with a constant flow rate. They need to be calibrated before the start of an experiment.

Figure 2.3: MasterFlex industrial pumps

2.1.4 Double Bucket Setup

We used a double bucket setup [Oster,1965] to generate a linearly stratified density profile in the tank. To fill the tank with a volume of about 1200 L, we need the two buckets to be at least 650 L each to maintain enough water in the mixing bucket.

If we define the flow rate from the freshwater bucket to the saltwater bucket as Q_1, and the other as Q_2 from saltwater bucket to the tank, then to generate a linearly stratified profile, these two flow rate should have the relation

$$Q_2 = 2Q_1 \tag{2.1}$$

To create a stratified fluid, it is important to prevent mixing from happening. So the flow rate Q_2 should not be too fast, and there is a float made of sponge and foam placed at the end of the tube in the tank to reduce mixing. A homogeneous bottom layer will be generated before the mixer is turned on to offer some buoyancy force to

Figure 2.4: The double bucket system

the float.

For the size of the tank, Q_2 has been set to as fast as 5 L/min thus Q_1 is 2.5 L/min, and the mixer is on during the whole process. For a volume of 1200 L, the filling process takes about 4 hours to complete. But usually Q_2 will be slower to get a better stratification, so the filling process can take more than half a day.

The stratified fluid is maintained for 1-2 weeks to carry out different experiments under various conditions. The volume of the tank allows the stratification to remain mostly unchanged after each experiment. Before every experiment, the stratification is measured by a conductivity probe.

2.1.4.1 Stratification Measurement

The stratification of the fluid is measured by a MTSCI fast conductivity probe (Precision Measurement Engineering) which is mounted on a motorized linear slide that

moves vertically above the tank as shown in Figure 2.6. The probe is connected with the computer through a LabJack U3, and a multimeter is also connected to read the voltage from the probe directly. The multimeter is used to calibrate the probe each time. The calibration tends to drift over time and so the probe is recalibrated before each experiment.

The calibration procedure is to record the voltage drop of four different solutions with different densities which have been measured accurately with an *Anton Paar DMA35* density meter. A parabolic fit is used to estimate the conductivity (voltage)-density relation and to plot the density stratification measurement as a function of depth.

After the calibration, the probe is controlled by a Python script to move down automatically and measure the density simultaneously. The density is plotted as a function of depth to calculate the buoyancy frequency, N^2. Each time we measure the stratification, there will be a record stored according to a timestamp for further analysis.

2.2 Wave Generator

The wave generator used in our project generates different types of internal waves [Mercier et al., 2010]. For vertically trapped, mode-1 waves, the generator forces a sinusoidal boundary condition that varies in time. By solving the wave equation analytically or numerically, we can predict the waves in the tank forced by this wave generator.

The wave generator we have is made of high density polyethalene. There are

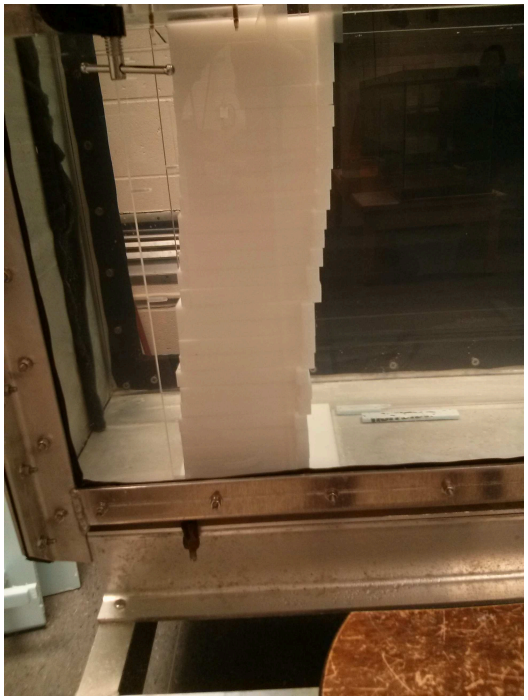

Figure 2.5: Wave generator with vertical resolution of 2 cm

26 plates in generator and each of them is about 2 cm in height, for a total height of 52cm. The resolution of 2 cm is small enough to create waves with a vertical wavelength of 100cm. The wave generator is about 56 cm in height, including a 2cm thick bottom plate and an outer transparent plastic box made of acrylic. A central shaft though all the plates is rotated by a motor. Twenty-six cams are mounted along the shaft with different phases to drive the plates to give sinusoidal motion in time.

We used a brushless DC motor with a 200:1 gearbox which could rotate with a angular frequency ω ranging from 0.04 rpm-25 rpm, which satisfies the internal wave generation requirement as $\omega < N$. The motor is mounted above the wave generator and connected with gear box. A digital motor controller is able to set the rotation rate within 0.001 rpm of the target frequency.

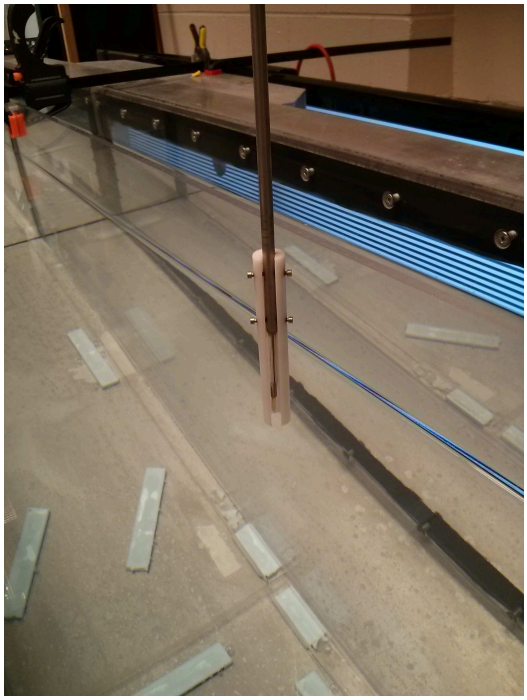

Figure 2.6: Conductivity probe for stratification measurement

2.2.1 Equations of the Wave Generator in Stratified Fluid

Linear theory allows us to predict the wave pattern generated by a given wave generator. This is very important in simulation and construction of a wave generator. The result from the wavemaker equations could also be a supplement to the measurement of the waves in the tank.

In stratified fluid, treating the fluid as inviscid, the internal wave equation in terms of stream function is:

$$\frac{\partial^2 \nabla^2 \varphi}{\partial t^2} + N^2 \frac{\partial^2 \varphi}{\partial x^2} = 0 \tag{2.2}$$

as introduced in Chapter 1.

We will review how to solve this equation under the boundary conditions.

$$\varphi_x = 0 \quad z = 0, H \tag{2.3}$$

$$\varphi_z = 0 \quad x \to \infty \tag{2.4}$$

$$\varphi_z = \xi'(t) \quad x = 0 \tag{2.5}$$

In which $\xi(t) = A\cos(mz)\cos(\omega t)$ is the profile of the wave generator, m is the vertical wave vector. In our experiments, we usually use a linear stratification and choose N^2=1.0 s^{-2}.

To get the solution for the stream function, we can use a Laplace transform to eliminate time derivative, from equation (2.2).

$$\hat{f}(s) = \int_0^\infty f(t)e^{st}dt \tag{2.6}$$

The transformed time equation (2.2), is written in terms of spatial derivatives only and we can use separation of variables to solve the equation. Then use the inverse Laplace transform to get the solution.

$$f(s) = \frac{1}{2\pi i}\int_{\epsilon-i\infty}^{\epsilon+i\infty} \hat{f}(s)e^{st}ds \tag{2.7}$$

Using all the steps above we can get the solution for the internal wave stream-function as:

$$\varphi(x,z,t) = -\frac{\omega A}{m}\sin(mz)\cos(\omega t - \frac{m\omega x}{\sqrt{1-\omega^2}}) \tag{2.8}$$

if we use the dispersion relation in chapter 1, eqn (1.16) and consider that N=1.0 s^{-2}, we can get the solution form:

$$\varphi(x,z,t) = -\frac{\omega A}{m}\sin(mz)\cos(\omega t - k_x x) \tag{2.9}$$

If we neglect the damping from the side wall, the internal wave in the tank should be a mode-1 wave whose vertical wave number depends on the vertical profile of the wave generator. The forcing frequency of the wave generator would be the frequency

of the system as well. We expect from our setup a 2D wave which does not vary along the y axis, but this needs to be tested in the real experiment. In the lab experiment, the solution above for internal waves may not be the best result to describe the wave field because viscosity does play a role in the wave propagation. There would be a decay of the wave amplitude as a function of the wave vector which we neglect. But in the near wave field area, we still can get good results from this model.

2.3 Neutrally Buoyant Sphere in Internal Waves

A sphere is the most common object to begin with in many hydrodynamic research projects for its advantage of total symmetry. By neglecting the weak rotation of the sphere while in a slow translational motion regime as well as the internal wave field, it is valuable to acquire some general knowledge about object-wave interaction through spheres given that many hydrodynamic characteristics of spheres are already well known.

The simplest but most effective scenario is to start with a neutrally buoyant sphere in stratified fluids. We can eliminate gravity and buoyancy force together from the equation of motion for the sphere. For a spherical shape, we can remove the concern about orientation of the object based on the assumption of weak rotation which can be neglected. The spheres we use are plastic spheres from AQUAFINA company, which are originally designed for wax storage. The spheres are hollow and can be opened with threads in the middle part. To create neutrally buoyant spheres, we submerge 2 parts of a sphere under the salt water solution of a certain density, and screw the sphere underwater. Then we have spheres that can neutrally buoyant at a

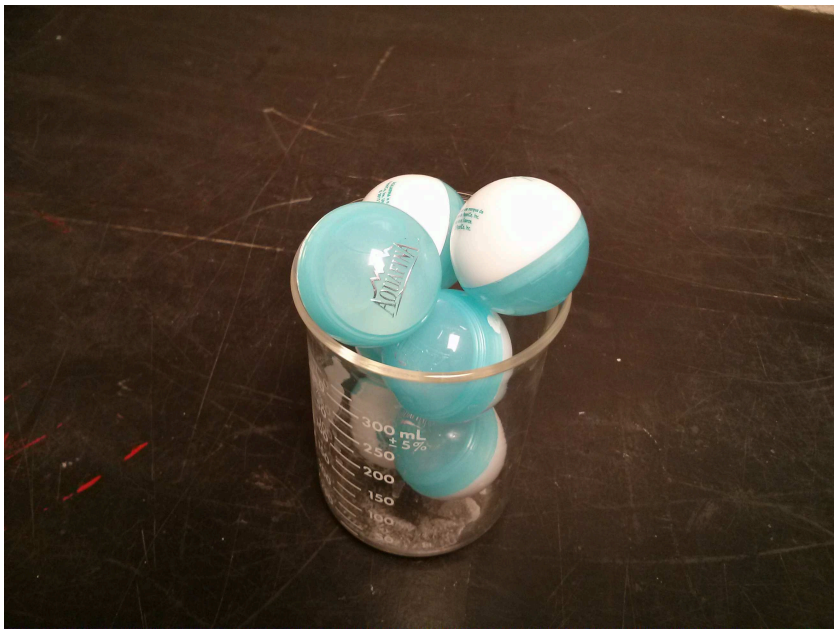

Figure 2.7: Spheres (plastic) used in the experiments

certain depth in stratified fluids.

If we apply the motion equations in Chapter 1 to the sphere, we will have the following equations:

$$m\dot{u} = F_{hx} \tag{2.10}$$

$$m\dot{w} = F_{hz} + (-G + B) \tag{2.11}$$

which is simpler than the expression before. And it would be a great help for the experiment and analysis.

2.3.1 Experiment Setup

The spheres we use are shown in Figure 2.7, they are plastic, hollow spheres that are connected by screws in the middle. These spheres, which are about 39.5mm in diameter, are filled with different densities of salt water solution to control their

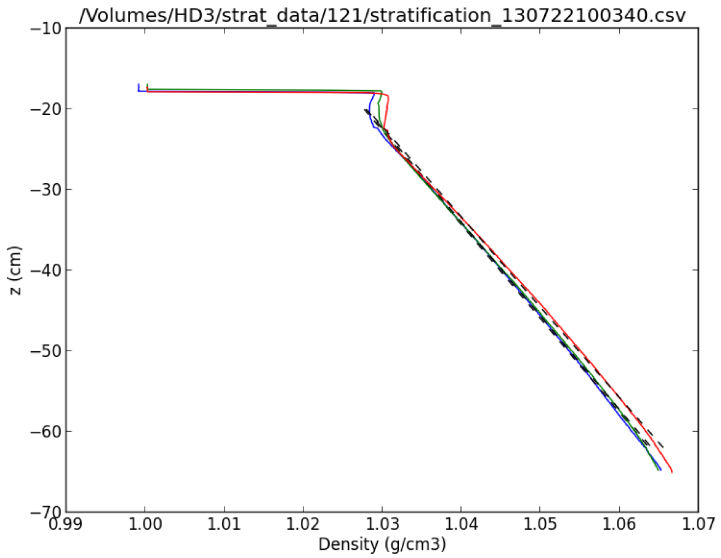

Figure 2.8: Stratification measured of the same fluid on: blue (July,16th), green (July,20th) and red (July,22nd)

mass, which allows them to be neutrally buoyant at different depths as required experimentally.

The tank is filled with stratified fluid using the double bucket setup, mostly we choose the buoyancy frequency N=1.0 s^{-1} as the default option. The buoyancy frequency plays a role in the time scale of the wave propagation . We want to avoid reflected waves from the far end of the tank that have a great effect on the motion of the sphere. The surface of the fluid is covered with styrofoam when not in use; this is to prevent the evaporation, which causes mixing of the top layer of the stratified fluid. After filling the tank, there will always be a mixed layer about 2 cm and will deepen as many experiments have been conducted. Figure 2.8 shows the change of stratification between July, 16th and July, 22nd. We can see that as there is a mixed layer and the layer is getting deeper with time. Data shows that the deepening rate

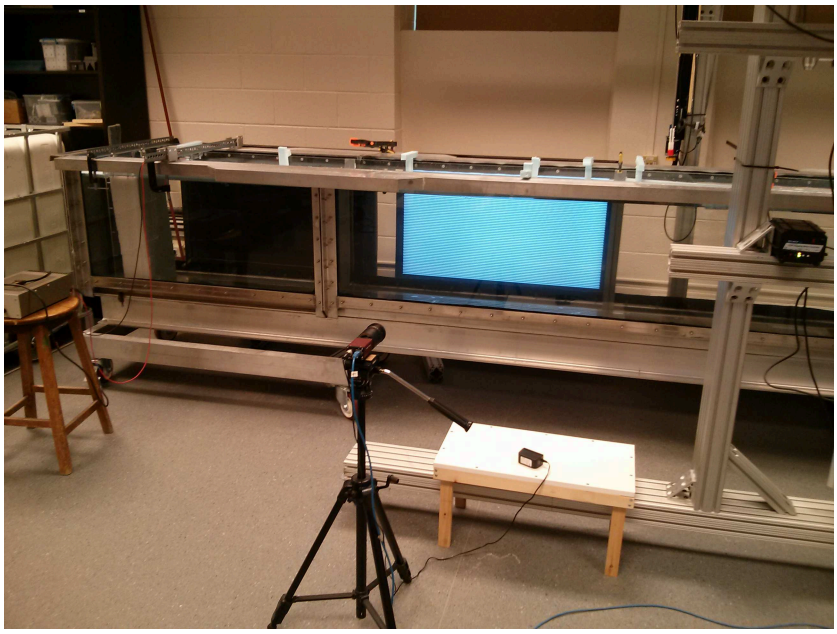

Figure 2.9: Basic experiment setup

of the mixing layer is 1 cm per 3 days approximately with the styrofoam on top. The change in stratification will change the boundary condition of the internal wave equations, which means internal waves generated by the wave generator with the same frequencies and amplitudes will be different. As a result, the data for experiments on different dates need to be compared carefully.

As the bottom plate of our wave generator is unmovable, fluids will be pushed out by the upper plates and fall down from the bottom plate, which will generate a strong internal wave beam across the whole tank. In initial experiments, the wave field in the tank was a superposition of the wave beam and a mode-1 wave which is not what we expected. To eliminate this we build acrylic bottoms which have the same height with the bottom plate. The bottom is made of a acrylic plates with thickness about 1.2 cm and many stryofoam feet about 0.8 cm in height, which just adds up to 2 cm,

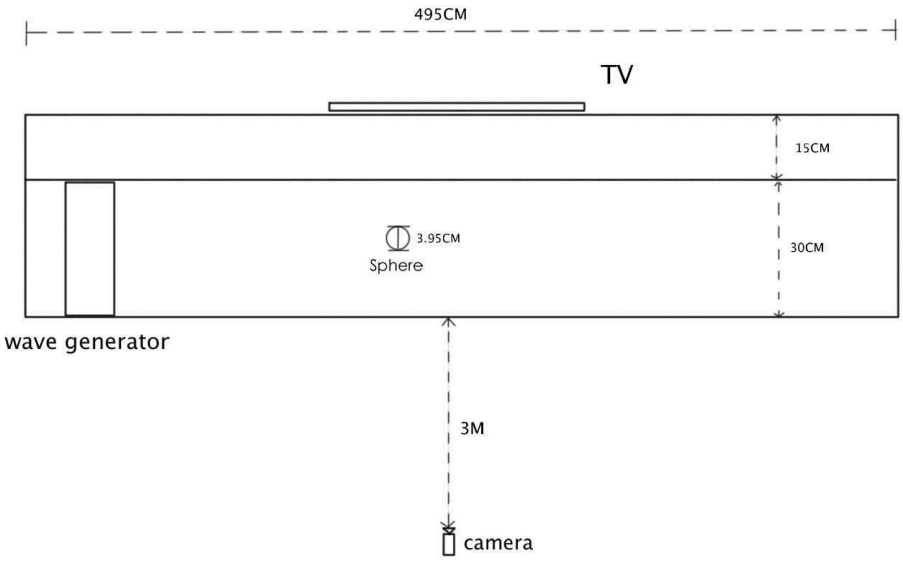

Figure 2.10: Schematic of the experiment setup

same as the thickness of the bottom plate. The acrylic bottom covers up to about 3 m in length and just the width of the front channel of the tank, which means there will be an internal wave beam generated at the end of the bottom.

Figure 2.9 shows roughly the setup of the experiments, (the camera is positioned much further back in an actual experiment). Figure 2.10 is the schematic of the experiment setup from a top view. The tank is filled with linearly stratified fluid with N $\approx$0.96 s^{-1}. The tank is divided into two channels with different width, about 30 cm for the front channel and 15 cm for the back channel. The 2 channel design should have the advantage that if we can reflect waves to the back channel at the end of the tank, we can greatly reduce the effect of reflected waves. This still needs to be achieved for future version of the experiment. The wave generator is placed near the left end of the tank in the front channel. A 49″ television placed behind the tank

about 95 cm away from the wave generator, is used as a bright background with a image of black and white lines. The black and white line image is set for the synthetic schlieren method [Sutherland.B.R and Linden.P.F, 1999] when the wave information is needed. The camera is placed about 3 m away from the front wall of the tank. Figure 2.11 gives a sample picture from our experiments. We can obtain a field of view about 75 cm $\times$ 48 cm, including the surface of the fluid. Spheres with different densities float in the tank according to the experiment requirements.

Table 2.1: Combination of parameters

N (s^{-1})	ω (s^{-1})	A (cm)	ϕ
1.0	0.2, 0.25, 0.3, 0.35, 0.4, 0.45, 0.5, 0.55, 0.6	2.0	0, $\frac{1}{3}\pi$,$\frac{1}{2}\pi$, π, $\frac{4}{3}\pi$, $\frac{3}{2}\pi$
0.7	0.1047, 0.2, 0.3, 0.4, 0.5	2.0	0, π

There are many parameters that affect the motion of a sphere in an internal wave field, but we just have the ability to change the internal waves. As a result, parameters related to the features of internal waves will be our main variables, including the buoyancy frequency N, the internal wave frequency ω, the initial phase of the wave generator ϕ, amplitude of the wave generator A and the initial position of the sphere (x_0, z_0).

Table 2.1 shows combinations of parameters that change in the experiments. We carried out most experiments with buoyancy frequency N$\approx$1.0 s^{-1} and some are done with N $\approx$0.7 s^{-1}. The buoyancy frequency is determined while filling the tank, and remains the same over succesive experiments.

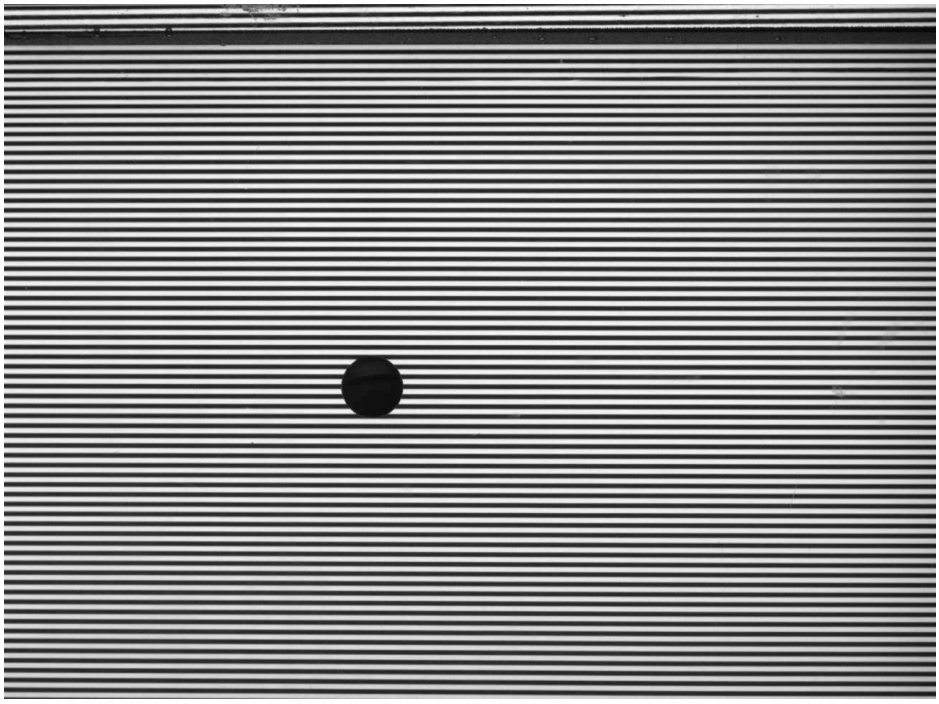

Figure 2.11: Raw image sample from our experiments

The frequency of the internal wave ω will be the same as the frequency of the wave generator, which can be set using the digital motor controller before turn on the motor. As the display on the controller is in rpm, and we have a 200 : 1 reduction gearbox to slow down the spin of the shaft, the transformation from rpm to s^{-1} considering the gearbox ratio will be given in Appendix A (Table A.1).

The initial phase of the internal waves is determined by the shape of the wavemaker profile when we turn on the motor. The shape of the wave generator is a half cosine profile, and the initial phase of the wavemaker is shown as Figure 2.12. The motion of the wavemaker can be described as $A\cos(\frac{\pi}{H}z - \omega t)$, where A is the amplitude of the plates, H=52 cm is the height of the wave generator and ω is the frequency.

The initial position of the sphere (x_0, z_0) is measured and recorded manually before

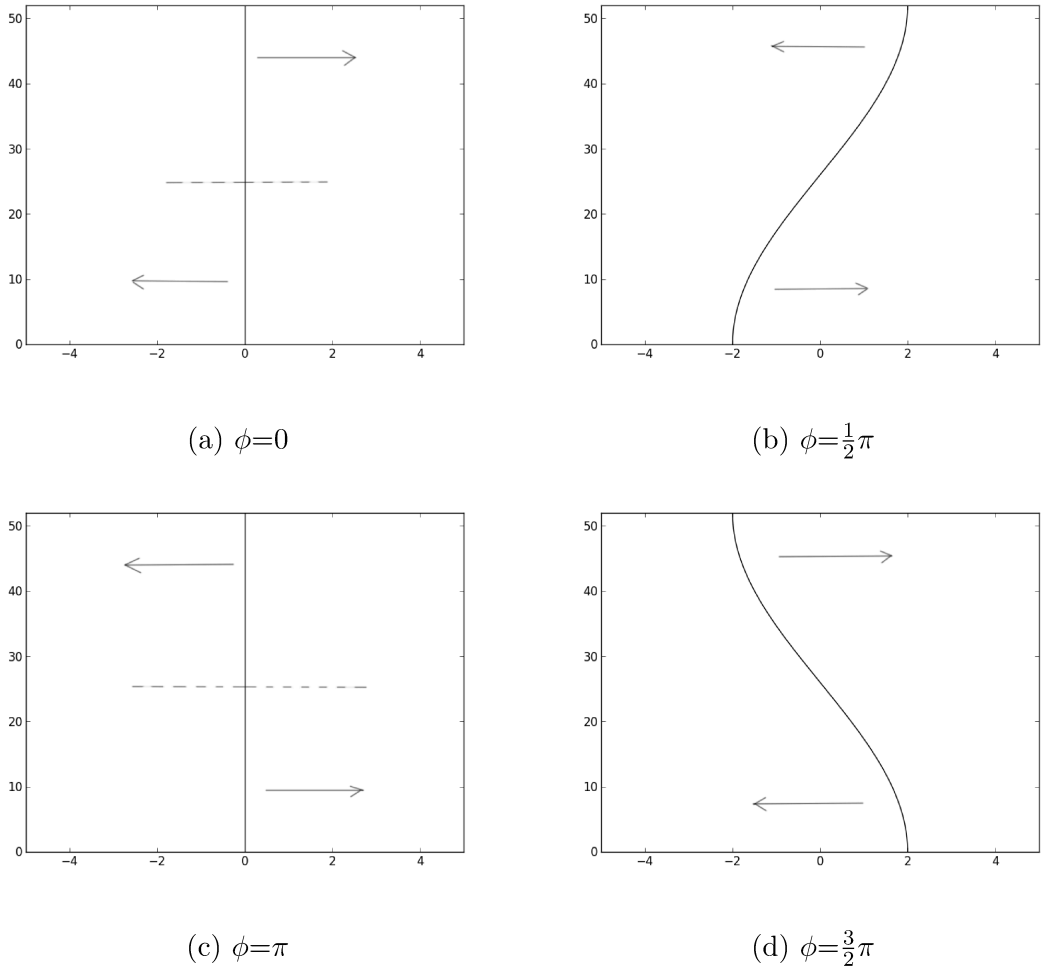

(a) ϕ=0

(b) ϕ=$\frac{1}{2}\pi$

(c) ϕ=π

(d) ϕ=$\frac{3}{2}\pi$

Figure 2.12: Initial phase of the wave generator, arrows represent directions of motion of the plates

each experiment. x_0 is the horizontal distance away from the middle plane of the wave generator ($\phi = \frac{1}{2}\pi$). And z_0 is the distance from the surface and is negative. The initial position of the sphere is hard to control as there will always be disturbance when the sphere is placed into the stratified fluid, including the motion of the sphere and the motion of the fluid. It would take some time for the sphere to be at rest in the fluid.

The camera starts recording 30 s before the wave generator turned on in each experiment, which is to record the motion (if any) without internal waves. As we mainly want data for the motion of spheres with rightward propagating internal waves, the reflected waves will come back about 120 s later (theoretical prediction based on the group velocity), so about 200 s video is enough for each experiment. After each experiment, the wave need time to dissipate and the sphere has to return to rest. For lower frequencies, the time for the tank to calm down is no more than half an hour, but for higher frequencies ($\omega/N > 0.5$), as more energy have been transferred to the fluid, the time can be as long as an hour.

2.3.2 Results

2.3.2.1 Horizontal Motion

The raw data is shown as Figure 2.11. We have to evaluate the position information for center of the sphere from a series of pictures with a Python script. A sample plot of the path data is shown as Figure 2.13 with the buoyancy frequency N=0.920 s^{-1}, wave generator frequency ω=0.45 s^{-1} and the phase of the wave generator $\phi = \frac{1}{2}\pi$. The first 2 plots show the horizontal (X) and vertical (Z) motion as a function of

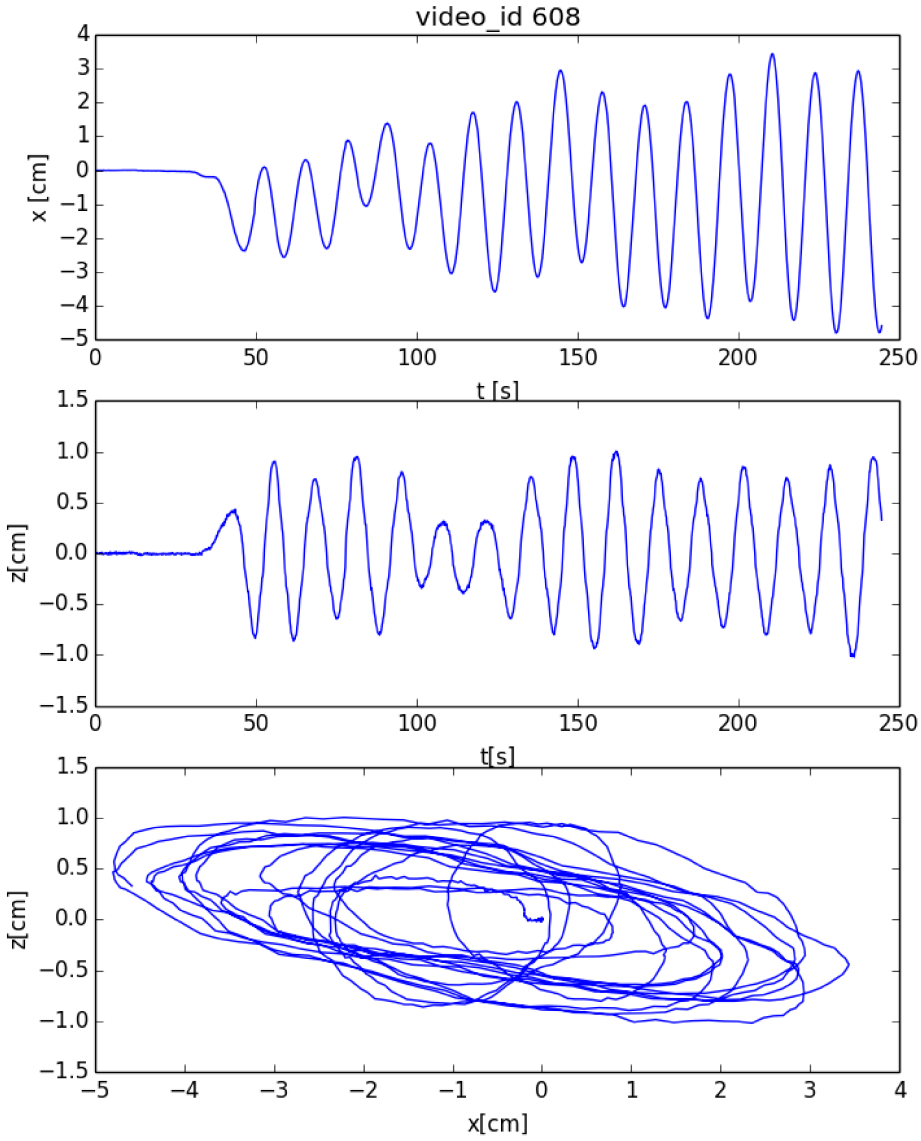

Figure 2.13: Sample data plot:N=0.920s^{-1}, ω=0.45s^{-1}, (x_0, z_0)=(143 cm,-13.0 cm), $\phi = \frac{1}{2}\pi$, x axis in the first 2 plots represents time in seconds

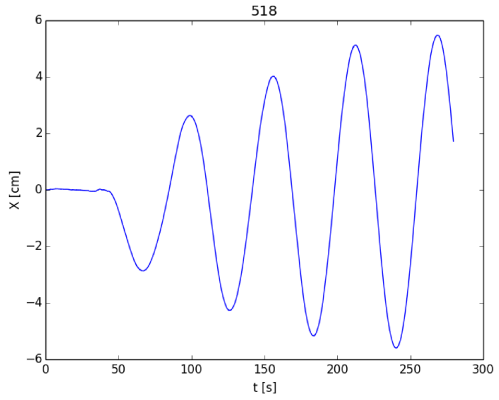

(a) ω=0.1047 s^{-1},z_0=-7.0 cm,N=0.909s^{-1}

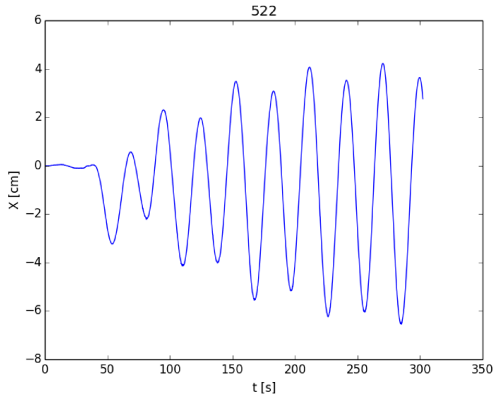

(b) ω=0.2 s^{-1},z_0=-7.0 cm,N=0.909s^{-1}

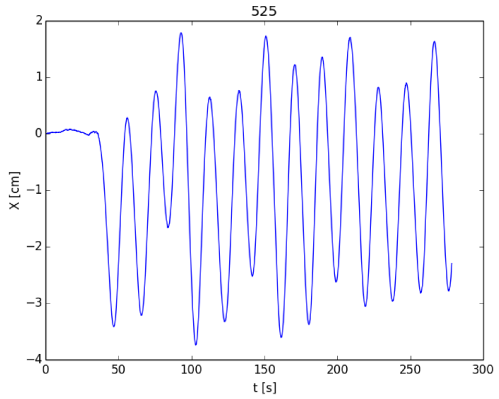

(c) ω=0.3 s^{-1},z_0=-7.0 cm,N=0.909s^{-1}

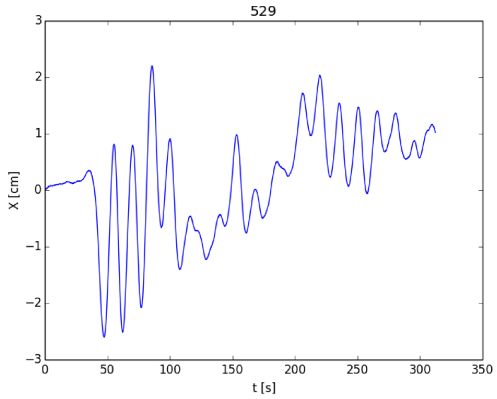

(d) ω=0.4 s^{-1},z_0=-7.0 cm,N=0.909s^{-1}

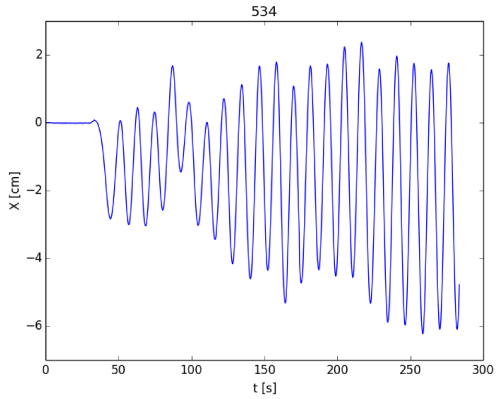

(e) ω=0.5 s^{-1},z_0=-7.0 cm,N=0.918s^{-1}

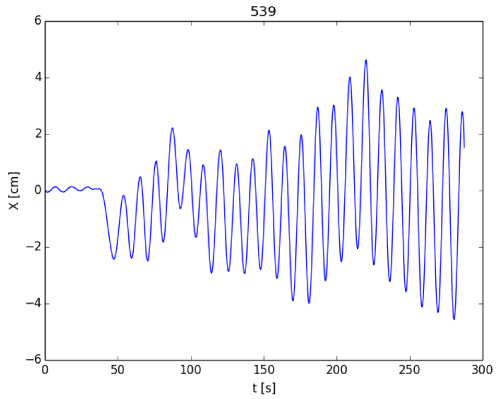

(f) ω=0.54 s^{-1},z_0=-7.0 cm,N=0.918s^{-1}

Figure 2.14: Horizontal motion with different frequencies ω, initial phase ϕ=$\frac{1}{2}\pi$

time and the third one plot the spatial path of the sphere center.

From the plot, we can see that for horizontal motion between $50-100$ s which only a right propagating internal waves exists, the path tend to indicate a slightly rightward drift for the sphere, but after the reflected waves come back and encounter the sphere, the motion becomes unpredictable and arbitrary at this frequency. A long time later, waves in the tank will be the superposition of the internal waves, reflected waves, effect of the unflat bottom and the standing waves which makes analysis challenging. The vertical motion of the sphere is relatively simple compared to the horizontal motion. Due to the existence of buoyancy force, the sphere cannot get too far from its equilibrium position vertically. But at relatively low ω/N, we can observe some harmonics of ω in the spectrum of the vertical motion, which require an explanation from the theory. The spatial path shows that the sphere is moving elliptically in the wave field, which is close to the motion of the fluid parcels, but the drift in horizontal indicates that the dynamics of these two kind of motions are different.

Figure 2.14 shows the path plots with ω as the variable parameter. We keep the depth of the sphere and the initial phase of the wave generator the same, although the buoyancy frequency changes because the last two experiments are done on a different day. The horizontal initial position of the sphere is not that important as the phase when the wave approaches the sphere is determined by the initial phase ϕ and the group velocity $\vec{c_g}$.

With the internal wave theory summarized by [Sutherland, 2010], internal waves are dispersive waves which means waves with longer wavelengths travel faster. In our experiment, the vertical structure of the internal wave is the same as the vertical

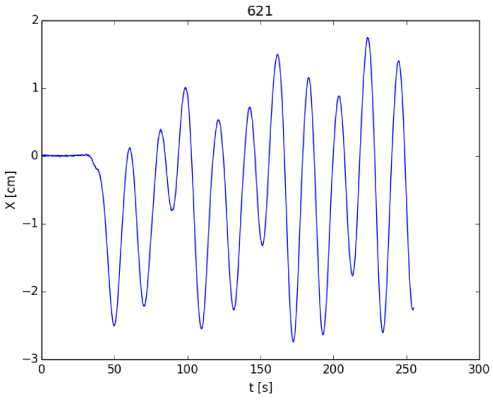

(a) ω=0.3 s^{-1},z_0=-14.0 cm, ϕ=0

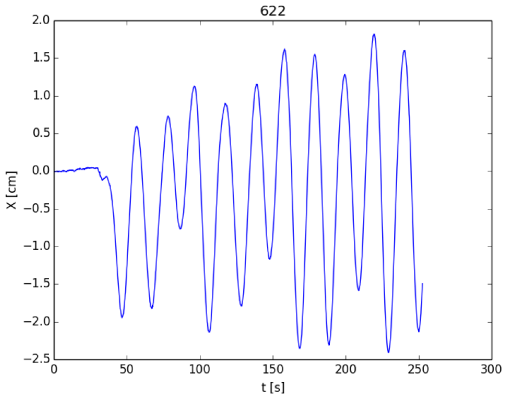

(b) ω=0.3 s^{-1},z_0=-14.0cm, $\phi=\frac{1}{3}\pi$

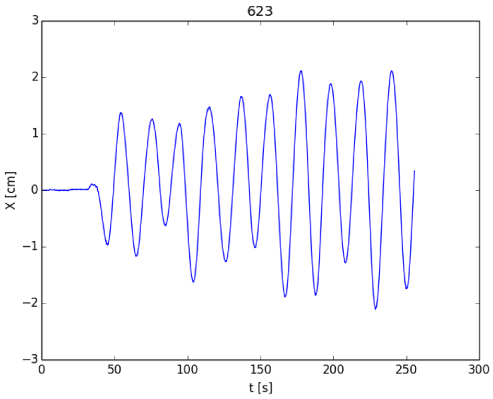

(c) ω=0.3 s^{-1},z_0=-14.0cm, $\phi=\frac{1}{2}\pi$

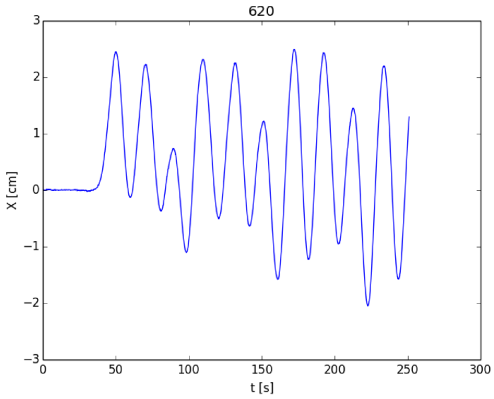

(d) ω=0.3s^{-1},z_0=-14.0cm, $\phi=\pi$

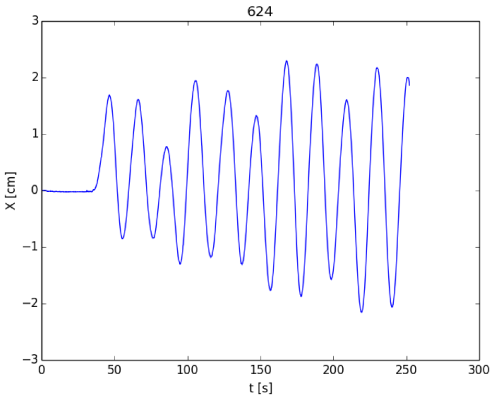

(e) ω=0.3 s^{-1},z_0=-14.0cm, $\phi=\frac{4}{3}\pi$

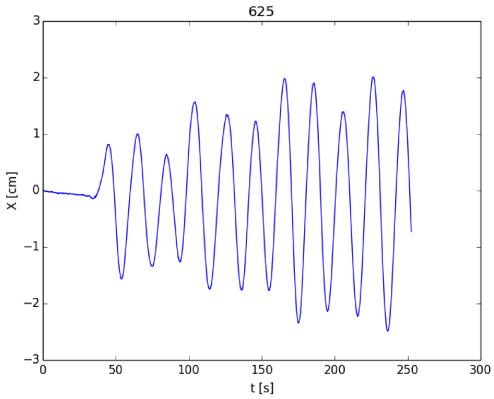

(f) ω=0.3 s^{-1},z_0=-14.0cm, $\phi=\frac{3}{2}\pi$

Figure 2.15: Horizontal motion with different initial phases ϕ, N=0.920 s^{-1}

structure of the wave generator, which means the vertical wave vector k_z=$\frac{\pi}{H}$=0.0604 cm^{-1} is constant. From equation (1.16), we can get the expression of k_x as

$$k_x = \frac{k_z}{\sqrt{\frac{N^2}{\omega^2} - 1}} \tag{2.12}$$

N is considered to be constant, and we can see from equation (2.12) with the growth of ω, k_x is decreasing, which means the horizontal wavelength $\lambda \propto \frac{1}{k_x} \propto \omega$, the lower the frequency, the faster the wave travels. This will greatly affect our experiment at low frequencies such as ω=0.1047 s^{-1}. From figure 2.14a, we can see that the sphere is moving as a fluid parcel, partly because the wave period is very long and the reflected waves come back at about 60 s after the recording starts. More detailed data about group velocity and frequency will be given in the Appendix. A.

From figure 2.14, we can see that the sphere is driven by the internal wave field, so the frequency of its horizontal motion is almost the same as the wave generator, as we expected. Figure 2.14d is different from the other path at frequency ω=0.4s^{-1}. This is probably because when the wave generator starts for this frequency, there are waves from the previous experiments in the tank. We can observe the sphere is moving to the right before the wave generator starts. The path for figure 2.14d should be a result of superposition of internal wave fields from different experiments. This can be the reason for the non-linearity of figure 2.14d. And within the first 100 s, when the internal wave is mainly propagating to the right, we can see a clear rightward drift of the sphere with ϕ=$\frac{1}{2}\pi$. Also, we can observe a growth in amplitude when the internal wave first approached the sphere, which indicates there is a transition process of the wave-object interaction.

Figure 2.15 shows the dependence of the horizontal motion on the initial phase

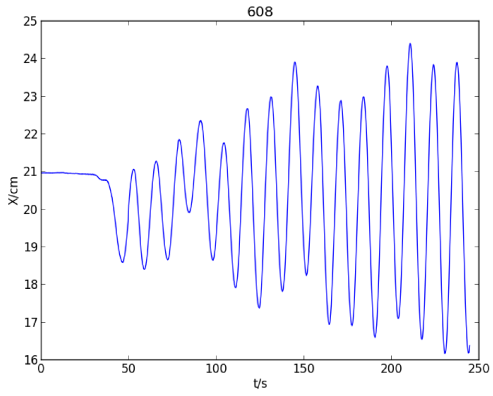

(a) ω=0.45 s^{-1}, z_0=-13.0 cm, ϕ=$\frac{1}{2}\pi$

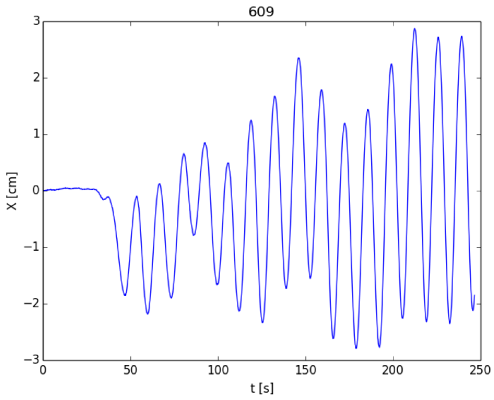

(b) ω=0.45 s^{-1}, z_0=-16.5 cm, ϕ=$\frac{1}{2}\pi$

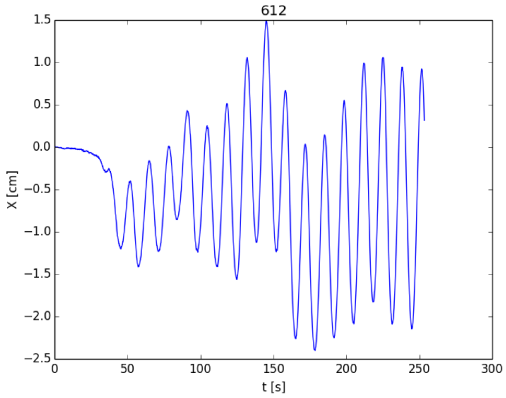

(c) ω=0.45 s^{-1}, z_0=-21.0 cm, ϕ=$\frac{1}{2}\pi$

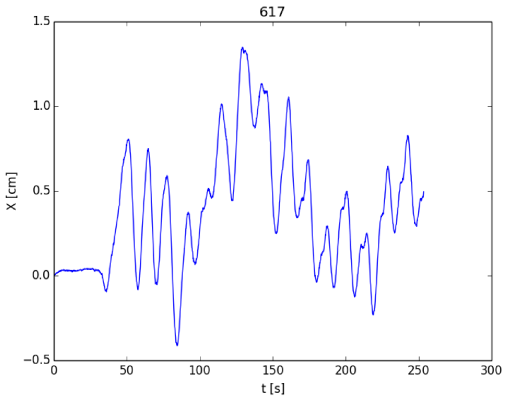

(d) ω=0.45 s^{-1}, z_0=-29.0cm, ϕ=$\frac{1}{2}\pi$

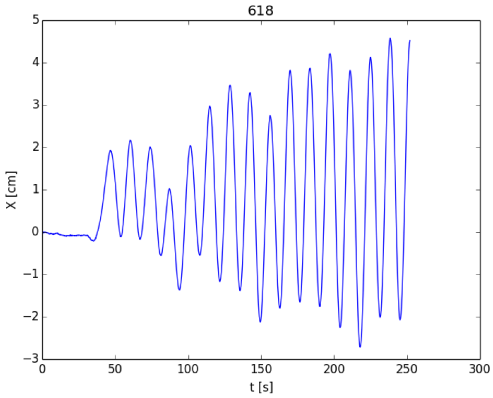

(e) ω=0.45 s^{-1}, z_0=-34.5cm, ϕ=$\frac{1}{2}\pi$

Figure 2.16: Horizontal motion with different depth z_0, N=0.920 s^{-1}

of the wave generator. The sphere stays at the same depth and we use a moderate frequency ω=0.3 s^{-1}. As the figure shows, we can see that the initial motion direction of the sphere are strongly related to ϕ as well as the drift direction. Roughly, we can say the drift direction is always opposite the initial direction of the wave or sphere motion. The value of the drift velocity may be related to ϕ depending on the data we obtained from each experiment.

Figure 2.16 shows the dependence of horizontal motion on depth of the sphere z_0. The change in depth will also affect the starting phase of the sphere, but the main difference in the change of depth is the change of vertical displacement of the wave field, which we suppose to have a impact on the magnitude of the drift velocity. Figure 2.16d show a different pattern than the rest, it is probably because at the depth of 29 cm under the surface, it is close to the interface where the wave generator does not move much. At this region, the wave field is not always uniform and some high vertical wave number structure may generated by the instability of the waves. So we see a relatively outlier path of the sphere.

We can observe the existence of the drift from the graphs above, but to understand and predict the internal wave induced drift, we need more analysis to show the relation of the direction and magnitude of the drift and all the parameters we introduced. This will be discussed in Chapter 3.

2.3.2.2 Vertical Motion

Figure 2.17 shows the vertical motion with different frequencies.The vertical motion of the spheres are relatively close to the motion of the fluid parcels, but we can see a slight difference with different frequencies. At low frequencies the vertical displacement is

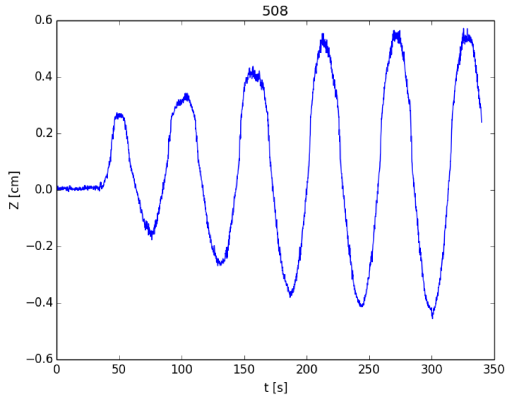

(a) ω=0.1047 s^{-1}, z_0=-18.5cm, ϕ=$\frac{1}{2}\pi$

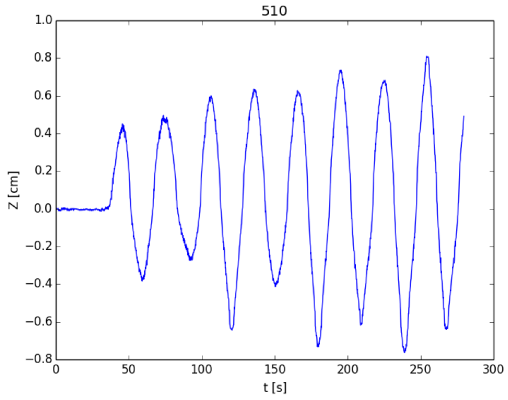

(b) ω=0.2 s^{-1}, z_0=-18.5cm, ϕ=$\frac{1}{2}\pi$

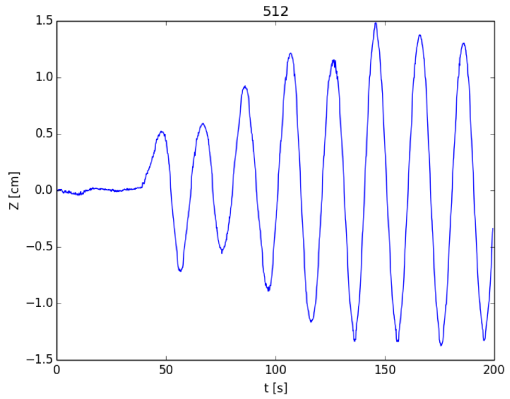

(c) ω=0.3 s^{-1}, z_0=-18.5cm, ϕ=$\frac{1}{2}\pi$

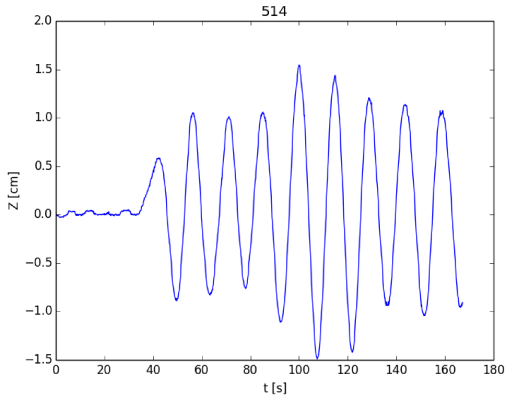

(d) ω=0.4 s^{-1}, z_0=-18.5cm, ϕ=$\frac{1}{2}\pi$

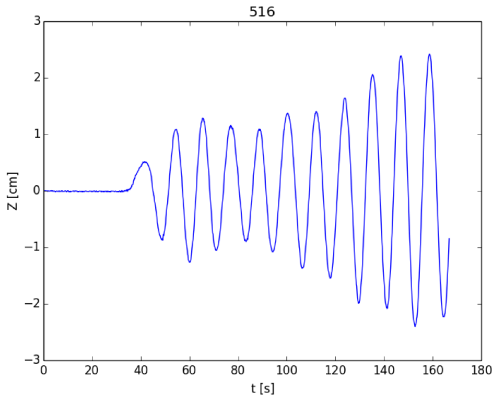

(e) ω=0.5 s^{-1}, z_0=-18.5cm, ϕ=$\frac{1}{2}\pi$

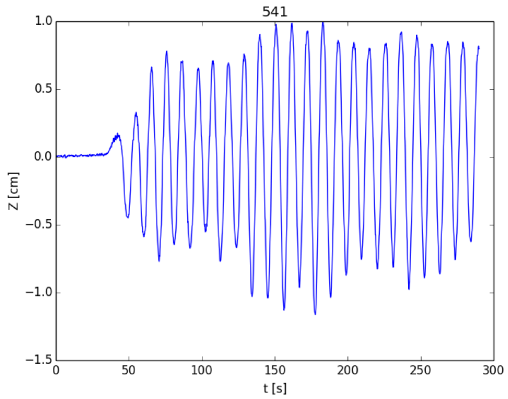

(f) ω=0.56 s^{-1}, z_0=-7.0cm, ϕ=$\frac{1}{2}\pi$

Figure 2.17: Vertical motion with different frequency ω

not as smooth as at high frequencies. This is in part because how we measure position from the raw image. There maybe a little error when we read vertical position of the sphere, but that only explains the mussy part of the curve. The irregular, non-sinusoidal shape at low frequencies can not be explained by the deviation from our tools. The sphere must oscillate around levels of neutral buoyancy. As the reflected waves reach the sphere, the amplitude of the vertical motion may increase as the result of superposition. Fourier analysis will not have a simple estimation of the amplitude information. We need some other methods to evaluate the information in the vertical motion.

Chapter 3

Analysis

3.1 Drift in the Horizontal Direction

When only the rightward propagating internal wave exist, we observe a wave induced drift of the horizontal motion of the sphere. From the experimental results, we observe that the magnitude and direction of the drift are related to many parameters such as the frequency of the wave, initial depth of the sphere and initial phase of the wave generator. We are going to explore an empirical formula for the drift velocity and dynamics of this phenomena.

3.1.1 Evaluation of Velocity and Drift Velocity

To get the information of the sphere motion, we need to choose a subinterval from the time series we recorded. Reflected waves from the far end of the tank also affect the motion of the sphere. Selection of the time domain depends on the group velocity of the wave c_g, which is determined from the dispersion relation of the wave. According

Table 3.1: c_{gx} and time for reflected internal waves reach the wave generator

$\omega(s^{-1})$	N(s^{-1})	c_{gx}(cm/s)	wavelength(cm)	time (s)
0.2	1.0	15.58	510.0	55.7
0.3	1.0	14.39	331.0	60.3
0.4	1.0	12.76	238.6	68.0
0.5	1.0	10.77	180.4	80.6
0.6	1.0	8.50	138.9	102.2

to equation (1.18), c_{gx} decreases as frequency of the wave generator increases, the reflected waves will reach the sphere earlier at lower frequencies.

Table 3.1 represents c_{gx} for each frequency and roughly calculates the time for an internal wave to travel along the tank and return after reflection. L=434 cm represents the distance from the wave generator to the end of the tank, and time is calculated from the formula $2L/c_{gx}$. As the sphere is located some distance away from the wave generator, the actual time domain will be shorter than that shown in Table 3.1.

In Chapter 2, the streamfunction for a mode-1 internal wave is given by equation (2.9), so the theoretical horizontal velocity of the wave should be:

$$u = -\frac{\partial \psi}{\partial z} = \omega A \cos(k_z Z) \cos(k_x X - \omega T) \tag{3.1}$$

and for the vertical velocity is:

$$w = \frac{\partial \psi}{\partial x} = \frac{k_x}{k_z} \omega A \sin(k_z Z) \sin(k_x X - \omega T) \tag{3.2}$$

for a internal waves propagating in a unbounded box. Although our tank has a

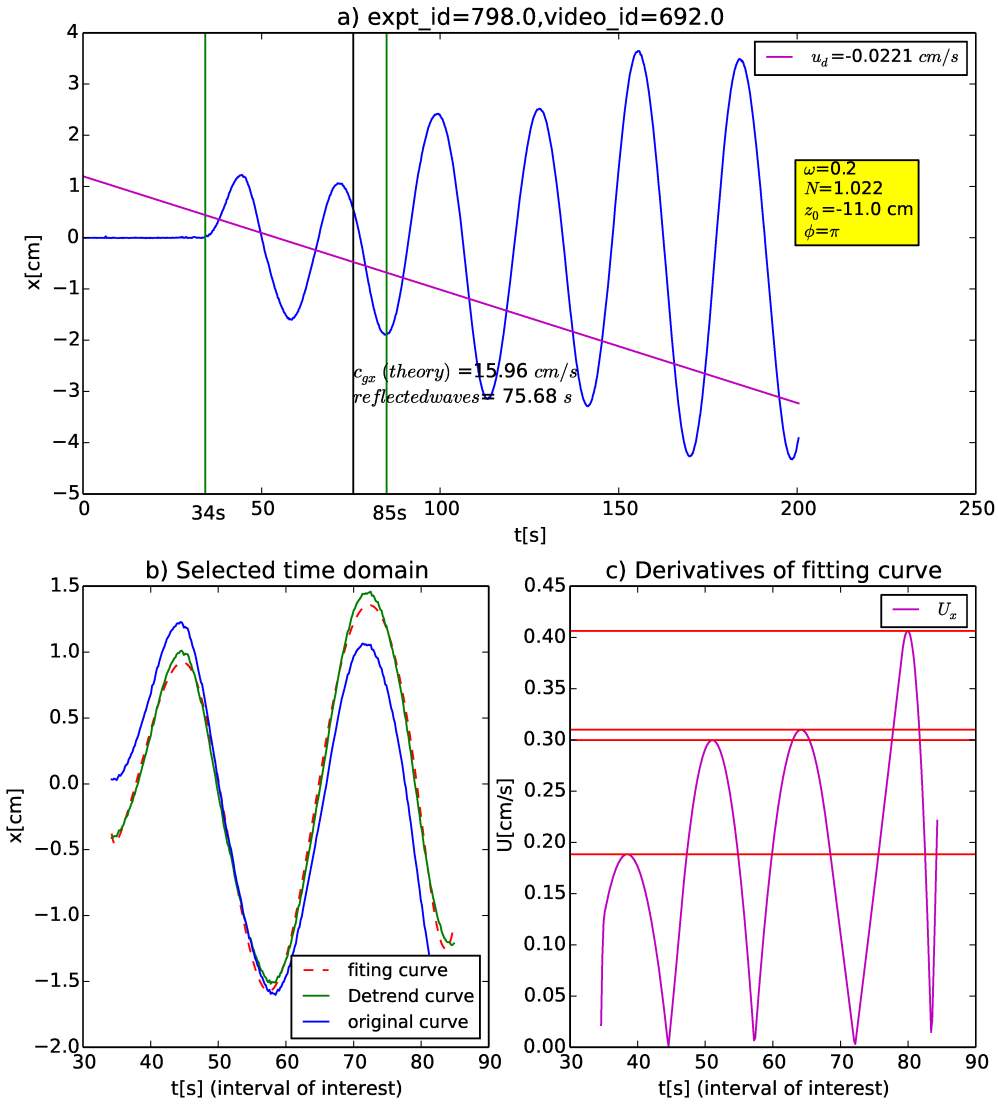

Figure 3.1: Evaluating velocity and drift velocity

right boundary, before the reflected wave reaches the sphere, the formula above can describe the motion of the fluid properly.

As the sphere motion is driven by the internal waves, we suppose the velocity of the sphere and the fluid should be close. We can use equation (3.1) to represent the major motion of the sphere, both for the maximum velocity and the amplitude. Figure 3.1 shows how we evaluate the motion velocity and drift velocity with this information and theoretical assumptions. The time interval (green vertical lines) is selected within the beginning of the motion to a completed wavelength near the time the reflected waves (black vertical line) reach the sphere, shown in the t-X graph in Figure 3.1a. The method we use to evaluate the drift velocity from the data is a linear fit of the data, as has been used by [Shen and Zhong, 2001] for the numerical study of the drift of small floating bodies in surface waves. A transient process for the growth of the amplitude needs to be considered, and the error need to be estimated for each experiment. In Figure 3.1, the sphere starts 11 cm below the surface of the fluid, frequency ω of the wave generator is 0.2 s^{-1} and the buoyancy frequency N=1.0 s^{-1}, the wave generator starts at $\phi = \pi$ where the velocity is negative maximum at the start. We can see from Figure 3.1a that the sphere is moving sinusoidally horizontally with an increasing amplitude, which is probably caused by the superposition of the propagating waves and the reflected waves. Without the reflected waves, there is a weak leftward trend for the motion of the sphere. The amplitude of the horizontal motion is close to the prediction from theory, where X_{amp}=$A\cos(k_z Z_0) \approx 1.57$ cm. To obtain the velocity amplitude of the sphere, we eliminate the drift with the estimated u_d and compute the derivative of the selected curve to get the maximum value. As shown in figure 3.1b, the selected t-x graph, the blue curve is from original data and

the green one is where we eliminate the drift, the red dash curve is a spline fit curve that we can use to estimate derivatives. In figure 3.1c the computed derivatives are given an absolute value showing derivatives of fitting curve. We average the peak values (red lines) to get the amplitude of horizontal velocity U as U_{amp}. For figure 3.1c, U_{amp}=0.34 cm/s.

Figures 3.2 and 3.3 shows U_{amp} acquired at a depth 7 cm and 11 cm below the surface. Green dots are computed from the experiment data and black squares are the theoretical predictions. The theoretical value is calculated using equation (3.1) as the amplitude is $U_{amp}=\omega A\cos(k_z Z_0)$ for a mode-1 wave, where ω and A=2.0 cm are the frequency and amplitude of the wave generator. The theoretical value is linear with ω at a given depth. Due to buoyancy, the sphere must oscillate around a neutrally buoyant depth. We can use this depth Z_0 as the parameter to estimate the velocity amplitude which is a sinusoid curve as a function of depth at constant ω. For the sphere at 7 cm below the surface, it is closer to the mixed layer and will encounter a larger viscous force as the frequency increase. At higher frequency, the measured velocities are lower than the theoretical ones, this may because at higher frequencies, the scale of vertical motion grows larger and it will easily moves into the mixed layer. While in Figure 3.3, the sphere stays far from the mixed layer, we can see a better consistent with the theoretical predictions.

From figures 3.2 and 3.3, we can see that the experimental data show a consistent trend with the theoretical results in both trend and value at these two depths. The error bars of the experimental data are computed from the difference of the mean value and the maximum or minimum values for each experiment. A better estimation of the velocity amplitude could be an average value of 2 consecutive peaks within one

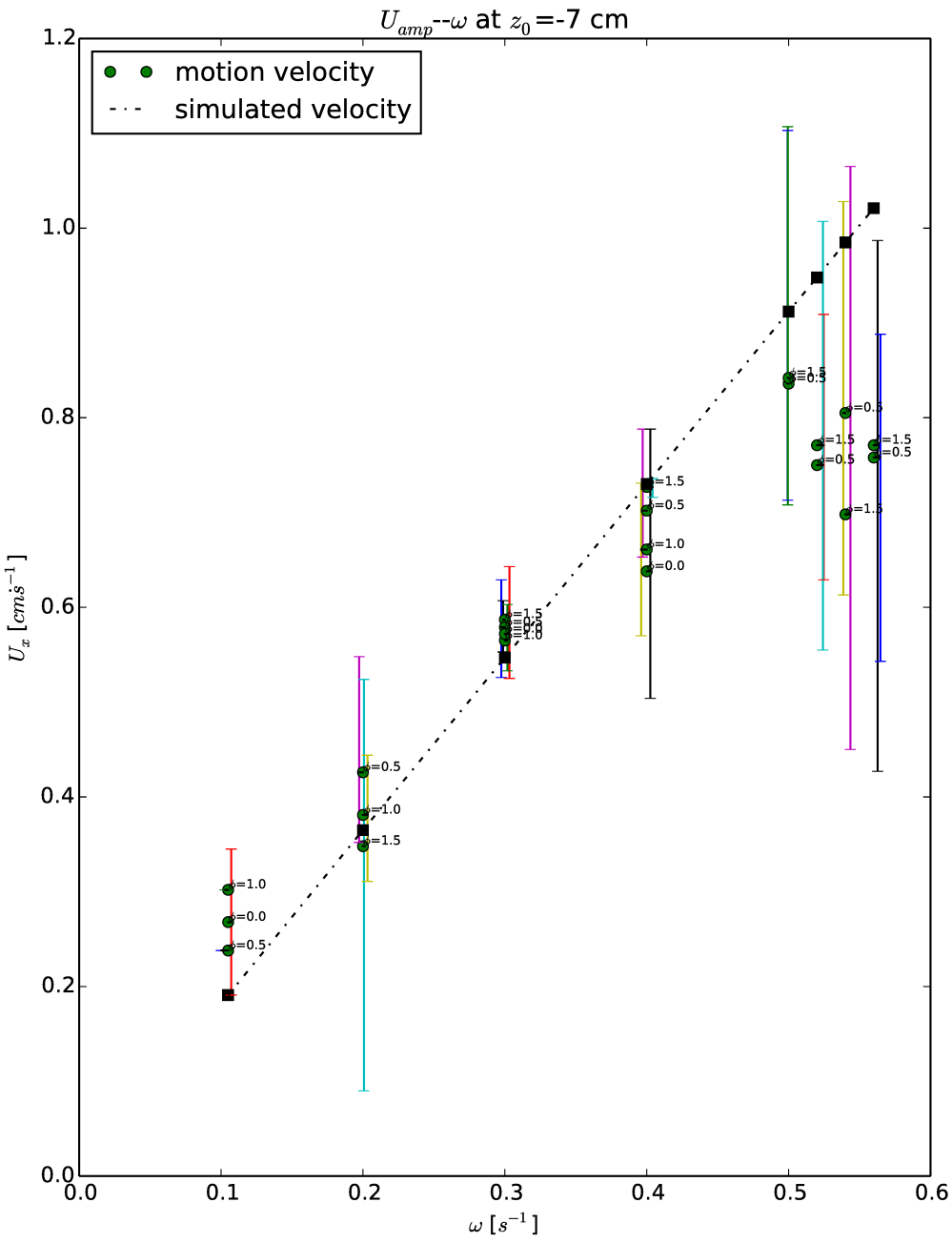

Figure 3.2: Evaluating of U_{amp} at z_0=-7.0cm, labels are phases of each experiment

wavelength, but the problem is for low frequency waves with higher c_g, we do not have enough data for such an analysis. Beside the error bar issue, the mean values from the experiments show great consistency with the theoretical values because the average can greatly eliminate the difference in peaks. The motion of the sphere can be roughly represented by the theoretical motion of the fluid, because the sphere is neutrally buoyant and the scale is relatively small compare to the wavelength.

Our experiments are carried out in the moderate frequency range from 0.2 s^{-1} to 0.6 s^{-1}, which satisfies the internal wave propagating condition that $\omega < N$. The streamfunction in Chapter 2 is derived without viscosity, which means at higher frequencies, the velocity deviates from the theoretical prediction and become smaller in value. And at higher frequencies, more mixing is generated greatly affect the experimental results.

3.1.2 Distribution of Drift Velocity

Although the general motion characteristics of the sphere can be described by the fluid parcel motion, the drag forces on the sphere will lead to different behaviours of the motion, such as a mean drift. The wave drift phenomena has been studied for surface waves for sea ice problems in the past. Most of the studies are focused on numerical simulations for small sized objects. Although some research have been done on the drift problem, we still lack knowledge in describing and understanding in this problem, especially for drift induced by internal waves.

Figures 3.4 and 3.5 shows drift velocity u_d as a function of ω/N with ω be the wave generator frequency and N the buoyancy frequency. u_d for all the experiments

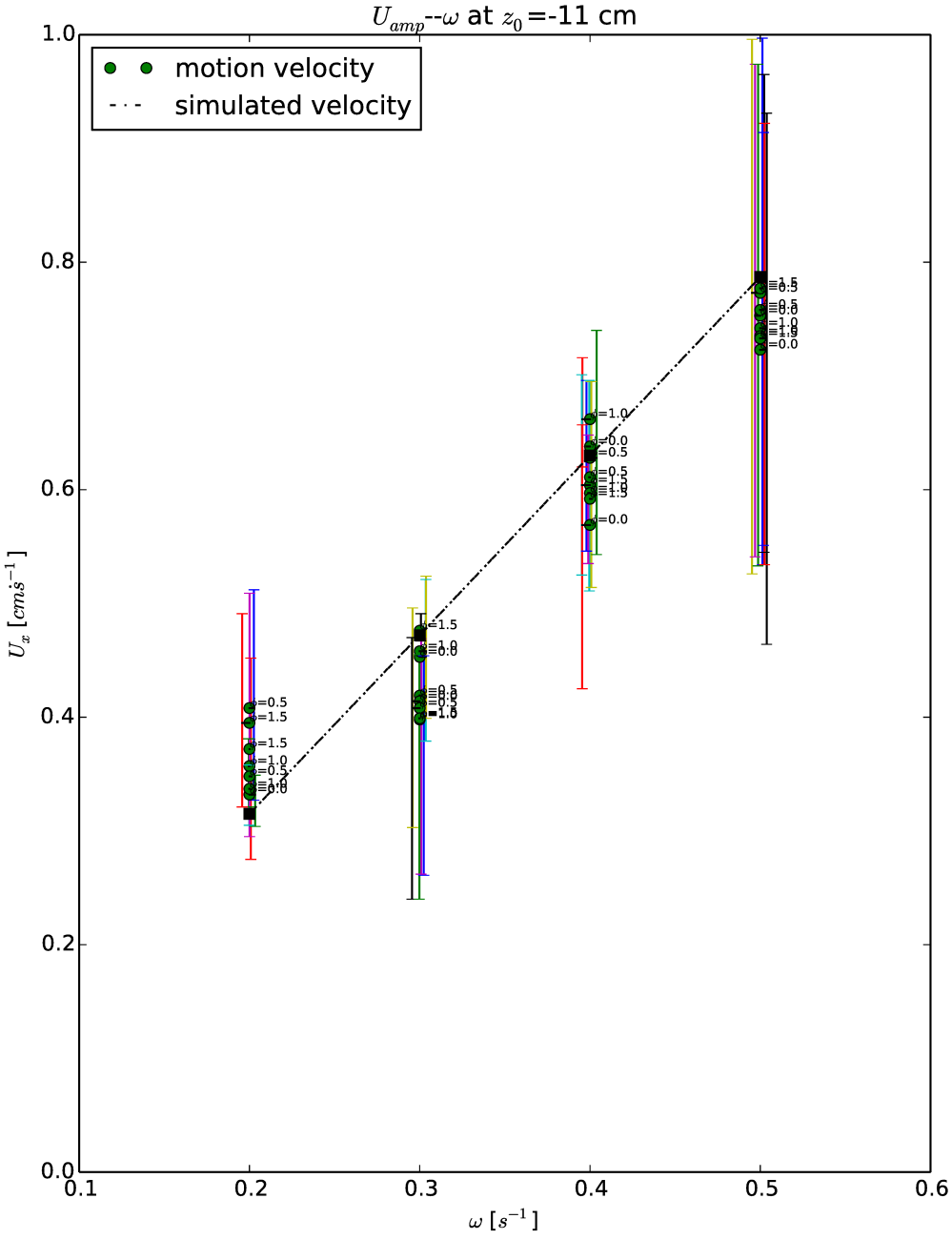

Figure 3.3: Evaluating of U_{amp} at z_0=-11.0cm, labels are phases of each experiment

are evaluated with a linear fit method within the time interval of only a rightward propagating mode-1 internal wave acting on the sphere. The sphere sits at different depths will have different values of u_d with the same ω/N, as the horizontal velocity U is dependent on Z_0. Different colors and types of dots represent different starting phase ϕ of the wave generator, which can be considered to be one of the initial conditions.

We can see from figures 3.4 and 3.5 that at both depth, u_d tends to show a decreasing trend in absolute value with increasing ω/N in the moderate range. We abandon the data where $\omega/N < 0.2$ as the group velocity is relatively large and the time domain for recording is not enough for analysis. And for higher frequencies, $\omega/N > 0.6$, the mixing generated near the wave maker spreads and the sphere motion is not smooth. The drift of the sphere is a small behaviour compared to the major elliptical motion, and it can be greatly affected by the wave state and the initial condition of each experiment, such as the initial phase of the wave generator or the initial velocity of the sphere. As we introduced before, there is usually a mixed layer at the top of the tank and this slightly change the wave field. For those experiments at Z_0=-7.0 cm, the initial velocity of the sphere is not strictly 0 because the waves in the tank did not disappear, which may cause some scatter of the points. But they are still showing the overall trend. For the experiments at Z_0=-11.0 cm, they were better designed and the initial velocities were strictly 0. We can see a more consistent distribution of u_d as a function of ω/N or ϕ. Although the motion velocity U_x is increasing with ω/N, u_d is decreasing as frequency ω increase in the first few wave periods with a constant N. As we consider the drift behaviour created by the phase lag between the motion of the sphere and the fluid, the phase velocity c_p can also be

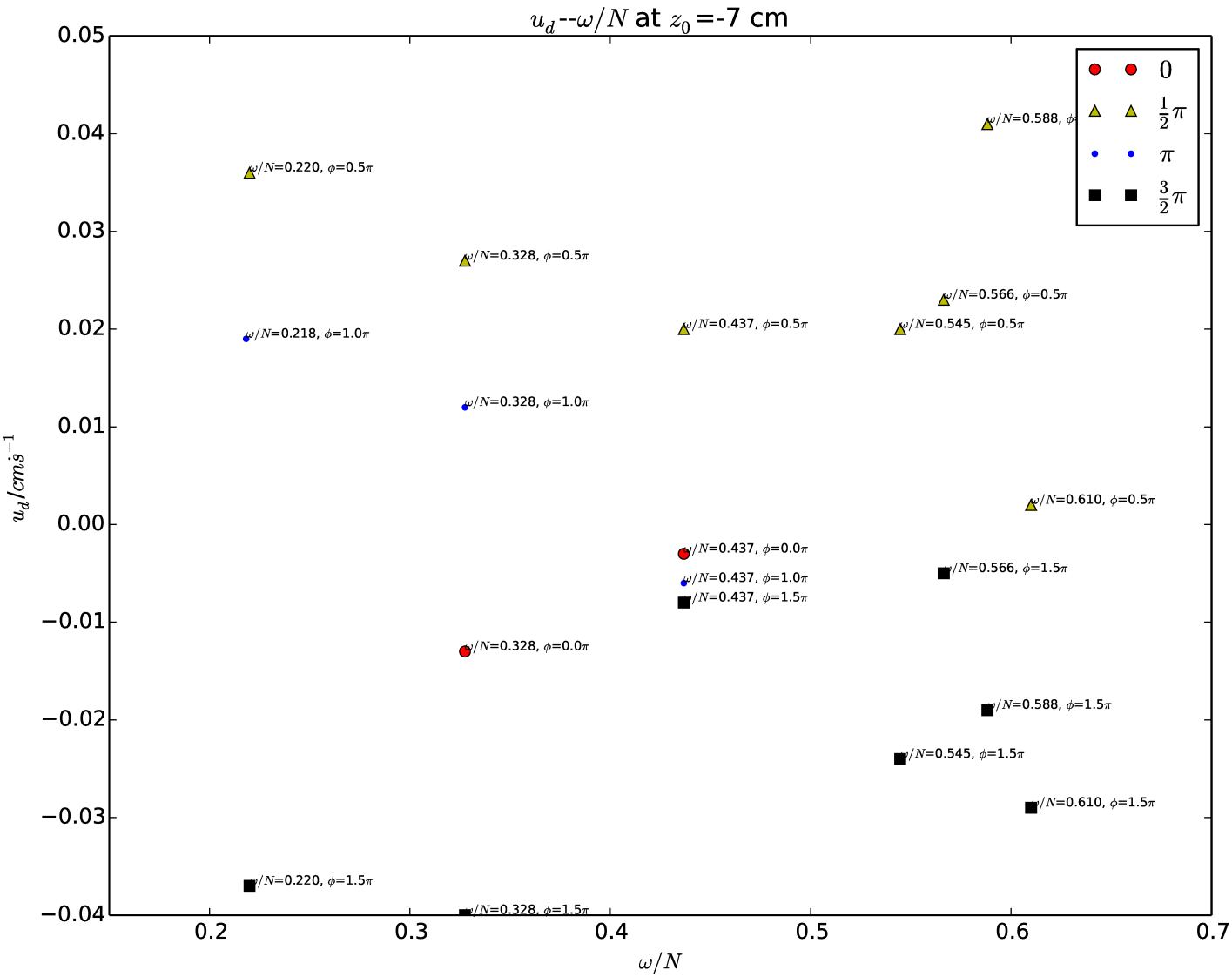

Figure 3.4: Distribution of u_d as a function of ω at z_0=-7.0 cm

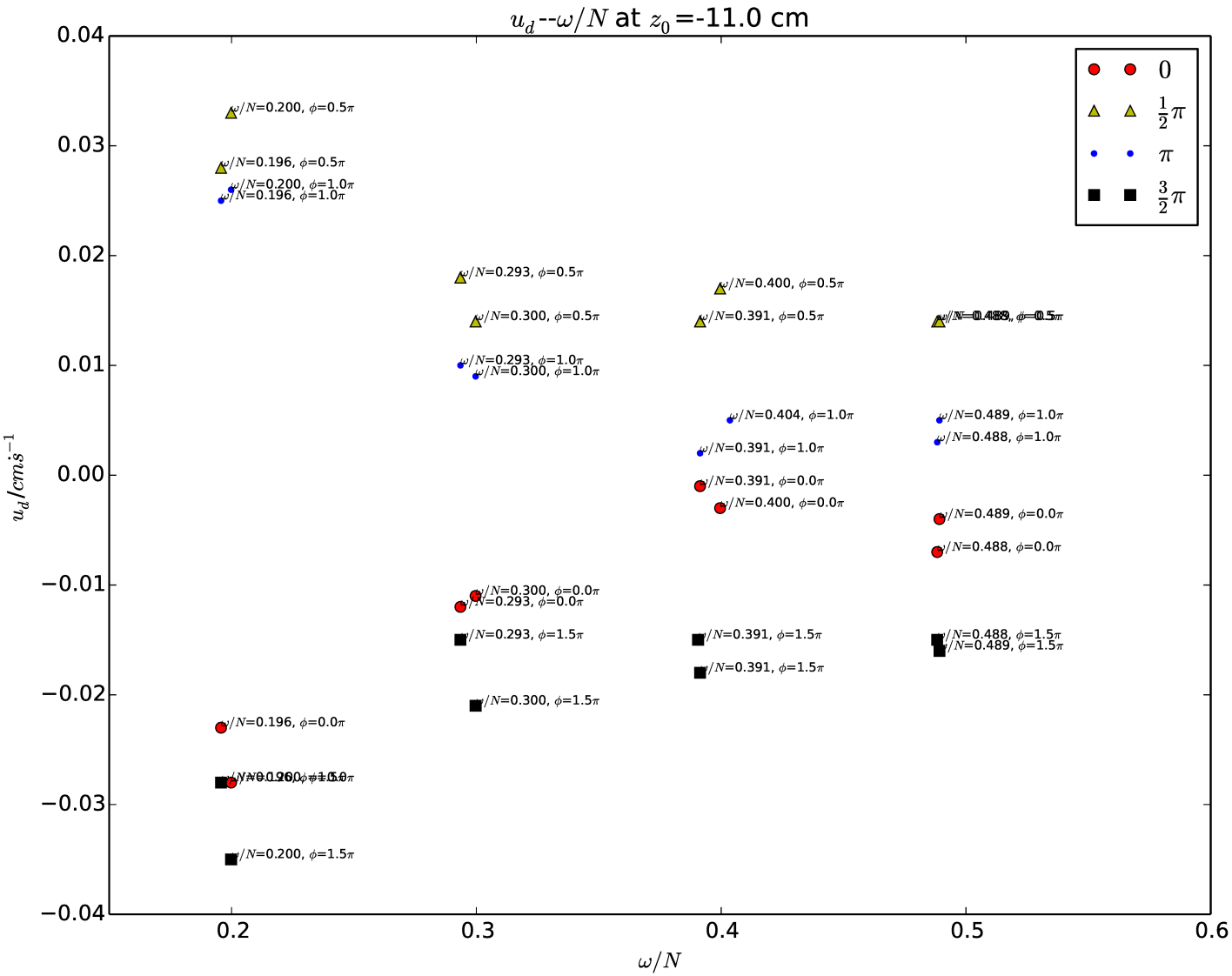

Figure 3.5: Distribution of u_d as a function of ω at z_0=-11.0 cm

a reason of this phenomena, which will be discussed later. Near the high frequency part, we can observe a slight increasing trend in u_d, which can not be explained by our result. For the hydrodynamics of the sphere, the change in frequency will lead to a change in Reynolds number and Richardson number, which may lead to a totally different expression of the hydrodynamic force. As the drift motion is sensitive to many conditions, it is hard to derive a general expression.

Figures 3.4 and 3.5 show that the initial phase is also a factor for u_d. Figure 3.6 shows that the difference in ϕ lead to a variation in both value and direction of u_d. Although at Z_0=-7.0 cm the points do not show as clear a pattern, at Z_0=-11.0 cm we can see a sinusoid distribution on ϕ. The values of ϕ are not representative values that demonstrate the amplitude distribution of u_d versus ϕ, but should be a continuous curve that describes the dependence of u_d on ϕ. What the phase really changes is the relative initial velocity U_{r0}=$u_0 - U_0$, where u_0 is the initial velocity of fluid parcels and U_0 be the initial velocity of the sphere. In our experiments, the sphere is designed to start at U_0=0, so U_{r0}=u_0, thus this can be controlled by the phase of the wave generator. Within the first few wave periods, u_d is greatly dependent on U_{r0} in both magnitude and direction in a mode-1 internal wave field.

Figure 3.7a shows the data for u_d at different depths Z_0. ω for every experiment is 0.45s^{-1} and ϕ=$\frac{1}{2}\pi$, thus the theoretically U_{r0}=0 for all of them. The only variable should be the velocity amplitude U_{amp} and the direction of U_{r0} after time zero. The difference in U_{r0} is caused by the shape of the wave generator, and the distribution of U_{amp} can be described by the theoretical formula U_{amp}=$\omega A \cos(k_z Z_0)$. This means U_{amp} should be maximum in value near the surface and bottom and zero in the middle part of the fluid. From the distribution of the dots we can observe a similar trend for

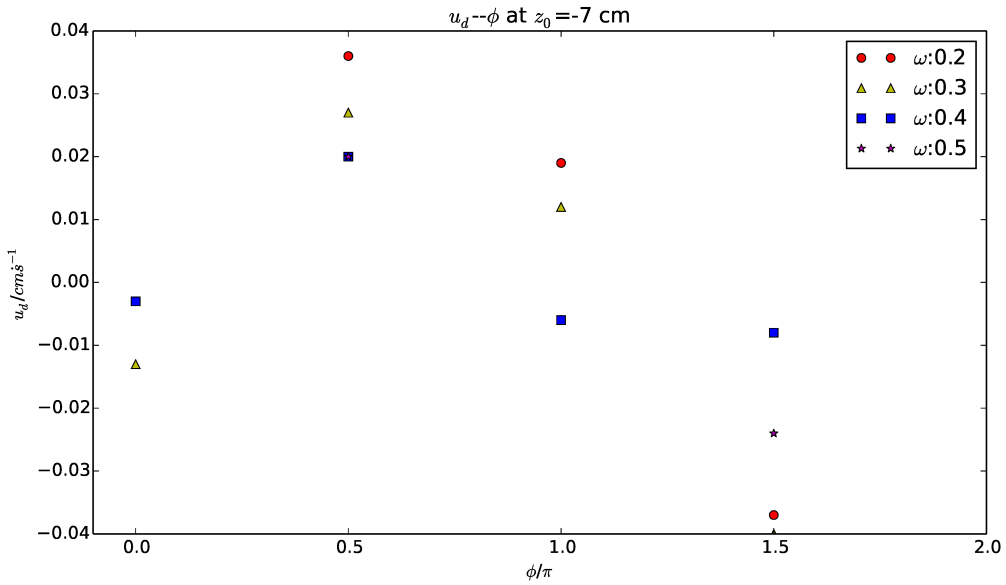

(a) u_d as a function of ϕ at Z_0=-7.0 cm

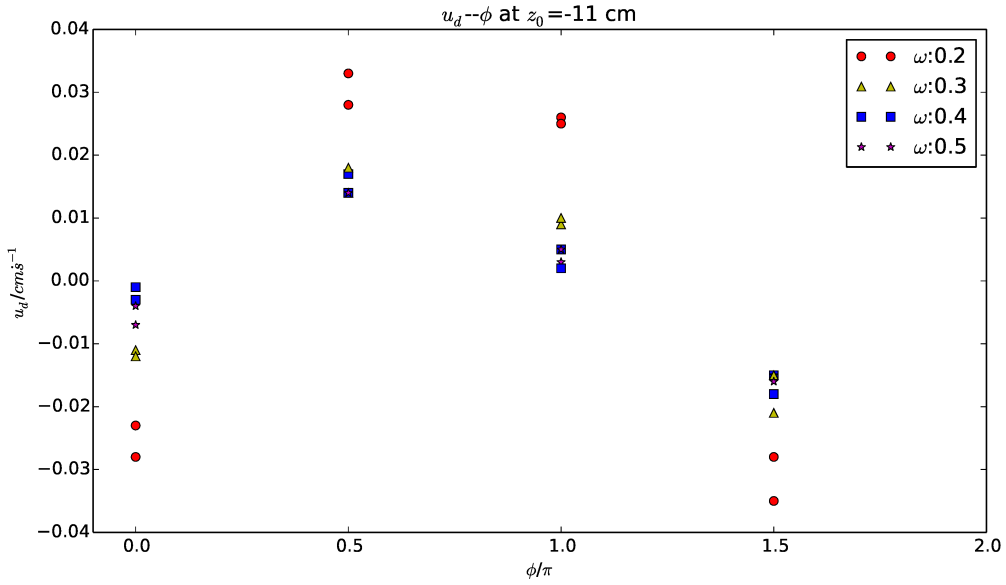

(b) u_d as a function of ϕ at Z_0=-11.0 cm

Figure 3.6: u_d as a function of ϕ at different depths

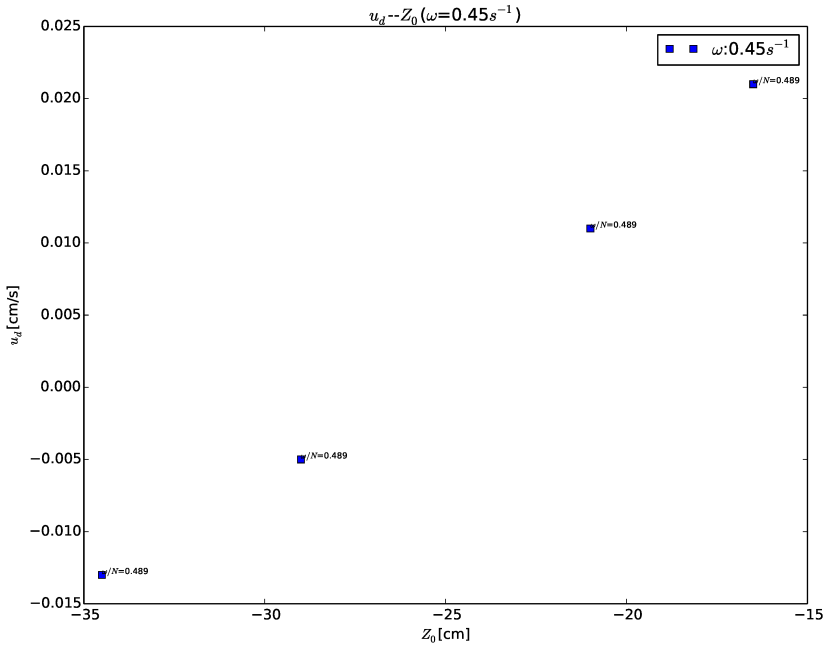

(a) u_d as a function of Z_0

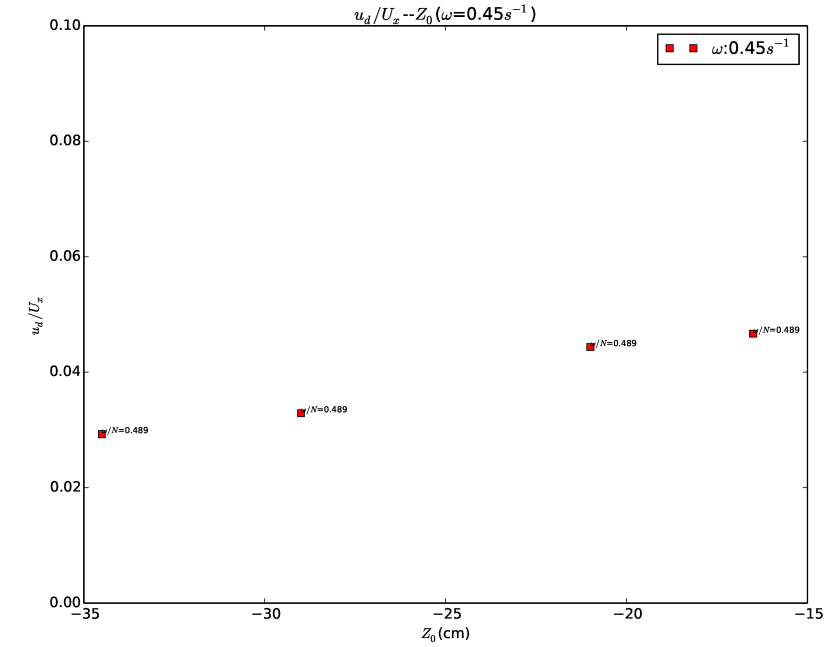

(b) u_d/U_x as a function of Z_0

Figure 3.7: u_d and U_x as a function of depth

u_d. Figure 3.7b shows u_d divided by U_{amp} plot versus Z_0. For Z_0 near 26 cm, the wave field turned out to be different from our theory, U_{amp} is close to 0 in this region and the wave shows some high vertical wave number structure in the middle of the wave generator. The result would be more predictable in this region, if we neglect the data near 26 cm, a reasonable assumption would be that the drift velocity is proportional to U_{amp} when ω/N and U_r remain constant.

The length of our data is not sufficient, so we cannot conclude that u_d is constant over the whole time domain, but in the transient section, we can predict the behaviour of the sphere if we can figure out the dependence of u_d on ω/N and ϕ. From the analysis above, we roughly get the dependence of u_d on ω, ϕ and U_{amp}. Our assumption of the equation form based on the experiment data would be:

$$u_d = CU_{amp}\cos(\phi + \delta\phi)f(\frac{\omega}{N}) \tag{3.3}$$

where U_{amp} is also a function of ω/N, $\delta\phi$ is the phase adjustment because the shift caused by the dispersion of the internal wave, C is a constant and $f(\frac{\omega}{N})$ is a decreasing function that need to be defined. Equation (3.3) is an expression for u_d within the first few wave periods in a mode-1 wave. Whether it is applicable for a long term drift needs more experimental investigation. At higher frequencies, the mixing due to our wave generator enhances the uncertainty of the results. The instability of u_d at ω/N near 0.6 may indicate the change in hydrodynamics of the problem. We will investigate these questions may need to be answered by numerical simulations based on a proper mathematical model in Chapter 4.

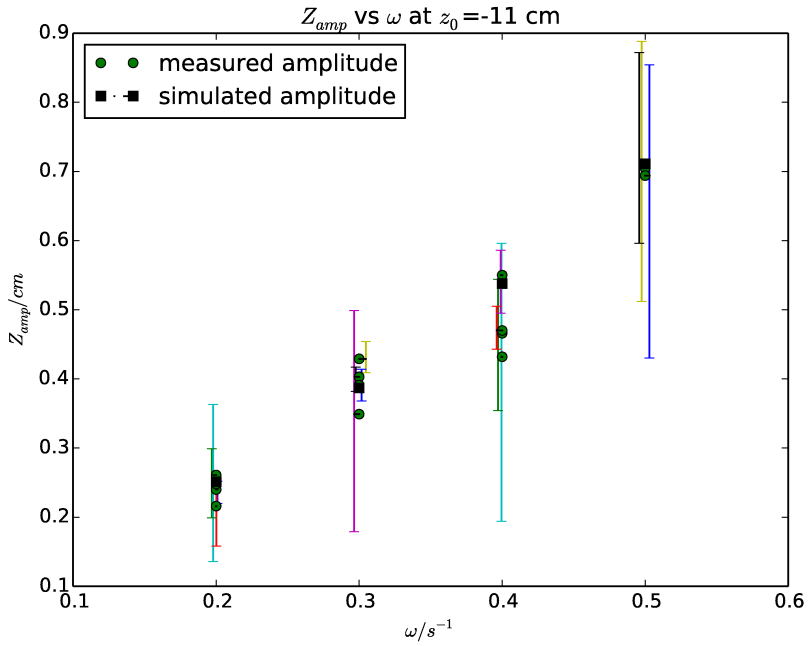

Figure 3.8: Z_{amp} versus ω

3.2 Vertical Motion

Given the restriction of buoyancy and gravity, the vertical motion of the sphere is relatively easy to understand. We have seen in Chapter 2 that the sphere is just oscillating vertically. But the vertical path is not as smooth as the horizontal ones, especially at low frequencies, the paths seem to be irregular from a normal sine curve. As shown in Figure 2.17 , the uneven curve is due to data capture tool and it is pretty high frequency and will not affect the analysis with the frequency limit $\omega < 1\text{s}^{-1}$.

As drift is not able to happen in the vertical motion, we will obtain the amplitude and frequency information of the vertical motion. Figure 3.8 is the amplitude information of vertical displacement Z_{amp} evaluated with the same method as the horizontal velocity amplitude. This time we just do a spline fit to the vertical path data within

the time limits and seek for the peak values. Green dots represents the measured values from the experiments and black dots are the theoretical value calculated from $Z_{amp} = A(\frac{k_x}{k_z})\sin(k_z Z_0)$, which represents the vertical amplitude of the fluid parcel at Z_0. The data is evaluated at Z_0=-11.0 cm. We can see the real data matches the theoretical estimates pretty well. The major vertical motion of a neutrally buoyant sphere can roughly be represented by the fluid motion.

Figure 3.9 gives the spectrum information of the vertical motion with different ω. Although the amplitude information is not accurate due to the superposition of reflected waves, the frequency information still can be useful. From figure 3.9 we can conclude that the vertical motion frequency is determined by the internal wave frequency.

The net force of buoyancy and gravity is an important force in the vertical motion. Other properties of the vertical motion will be studied in our numerical simulation.

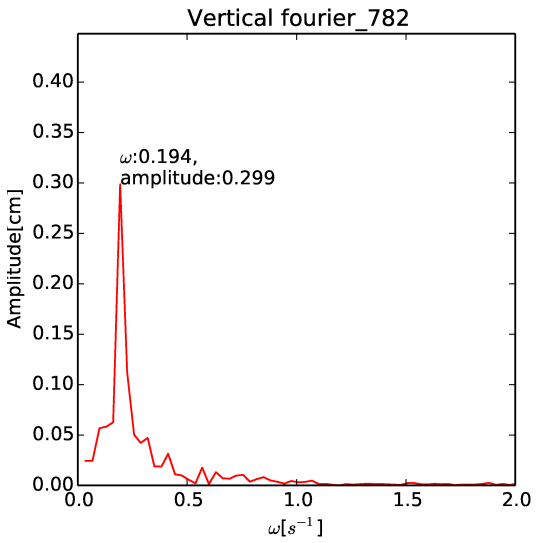

(a) ω=0.2 s^{-1}

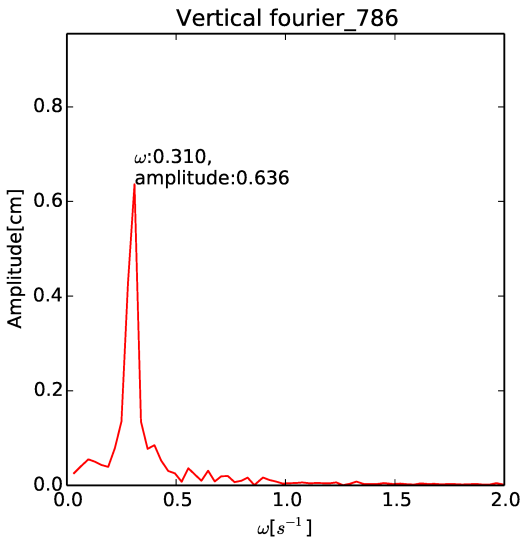

(b) ω=0.3 s^{-1}

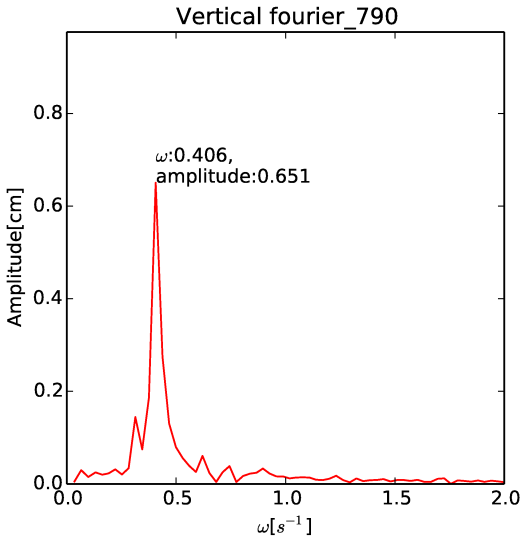

(c) ω=0.4 s^{-1}

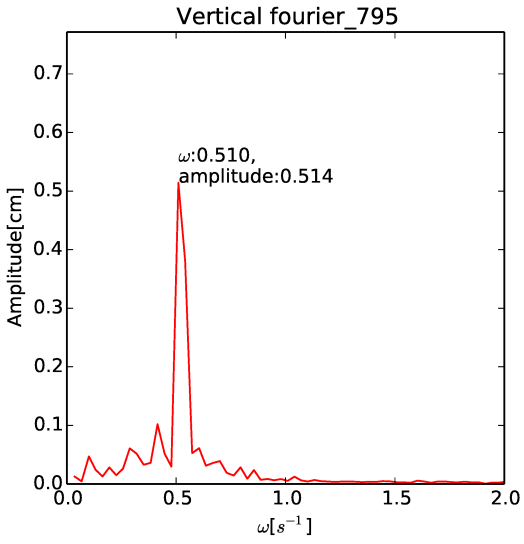

(d) ω=0.5 s^{-1}

Figure 3.9: Fourier spectrum of vertical motion with different ω

Chapter 4

Numerical Simulations

4.1 Morison's Equation and Vfgen

In addition to the lab experiments, we also carried out numerical simulations for the motion of the sphere in a internal wave field. To understand and explain the behaviour of the sphere motion in internal wave field, we need this theoretical support. Morison's equation is used to model the hydrodynamic forces on the sphere. An ordinary differential equation solver named vfgen has been used to solve the motion equations and calculate the necessary parameters.

4.1.1 Morison's Equation

In ocean engineering, the Morison equation can be used to estimate the force on a rigid structure such as offshore platforms in oscillatory flow. The Morison equation, or the MOJS equation named after a combination of its contributors: Morison, O'Brien, Johnson and Schaaf [Sarpkaya, 1986], is a semi-empirical formula consisting of the

inertial force and the drag force, which will bring in two empirical coefficients: the drag coefficient C_D and the inertial force coefficient C_m. We discussed about C_D in Chapter 1. The inertial force coefficient C_m is an empirical value obtained from experiments which have been used to simplify the effect of the inertial force. A relatively simple empirical equation is used to represent the complex dynamics of the object in the flow. The Morison equation for a fixed cylinder in a flow with sinusoidal motion is:

$$F = \frac{1}{2}\rho D C_D U_r |U_r| + \frac{1}{4}\rho \pi D^2 C_m \dot{U}_r \tag{4.1}$$

in which F is the in-line force per unit length on the cylinder, ρ is the density of the fluid, D is the diameter of the cylinder, U_r is the relative velocity of the flow to the cylinder and $\dot{U}_r = \frac{dU_r}{dt}$ is the derivative.

The first term on the right hand side of the equation represents the drag force from the viscosity of the fluid and the second one represents the inertial force. These are the hydrodynamic force due to the flow. The lift force, generated by the vortex as the flow past the cylinder and perpendicular to the flow direction, is not included within the Morison equation. C_D and C_m have a general dependence on some dimensionless numbers such as the Reynolds number which we introduced in Chapter 1, and as well as the Keulegan-Carpenter number also called the period number, representing the ratio of drag force and inertia force. The K_C number is defined as

$$K_C = \frac{UT}{L} \tag{4.2}$$

where U is the amplitude of the flow velocity, T is the period of the flow oscillation and L being the characteristic length of the object. The roughness of the object surface also affects C_D, as it determines the type of viscous force. The dependence of

C_D and C_m on Re and K_C were analyzed by Sarpkaya [1986] for homogeneous fluid and shallow water waves, which is different from our scenario of stratified fluid with internal waves. For our situation, the sphere is neutrally buoyant and supposed to stay on an isopycnal, thus the relative velocity U_r cannot be represented by the flow velocity particularly. We use u to represent the velocity of the flow and U represents the velocity of the sphere. The Morison equation [Sumer and Fredsoe, 2006] for a moving sphere in an oscillatory flow will be

$$F = \rho V \dot{u} + \rho C_a V(\dot{u} - \dot{U}) + \frac{1}{2}\rho C_D A(u - U)|u - U| \tag{4.3}$$

where V represents volume of the sphere, A is the the cross sectional area of the sphere, C_a is the added mass coefficient and C_a=$C_m - 1$. The first term on the right hand side is the Froude−Krylov force, which can be understand as a hydrodynamic pressure induced force from the wave field; the second one is the added mass term and the last one is the hydrodynamic drag force on the sphere.

The empirical added mass for a sphere in homogeneous fluid [Techet, 2005] is given by

$$m_a = \frac{2}{3}\rho\pi R^3 \tag{4.4}$$

where ρ is the density of the fluid and R is the radius of the sphere.

The motion can be described by a 2D system of equations in X and Z directions, as the internal wave field is set to be 2D, and the buoyancy change with depth need to be considered in vertical motion. We suppose the sphere sitting on and oscillating close to an isopycnal where ρ_{fluid}=ρ_{sphere}. So ρ_{sphere} can be replaced by ρ_{fluid} when calculating the mass of the sphere as $m = \rho V = \frac{4}{3}\rho\pi R^3$. Thus the added mass coefficient here we use is C_a=m_a/m=0.5. The added mass m_a is derived under homogeneous condition,

so C_a may not be exactly the same for the situation in stratified fluid with internal waves. Some adjustment of C_a may be applied to the model to get a better result.

To write the horizontal motion equation, we rewrite equation (4.3) and apply the Newton 2nd law as $F = m\dot{U}$, and we will get:

$$m\dot{U} = \rho V\dot{u} + \rho C_a V(\dot{u} - \dot{U}) + \frac{1}{2}\rho C_D A(u - U)|u - U| \tag{4.5}$$

and through some rearrangement, we can get:

$$\dot{U} = \dot{u} + \frac{C_D}{2m(1 + C_a)}\rho A(u - U)|u - U| \tag{4.6}$$

To get this we use the assumptions ρ_{fluid}=ρ_{sphere} from the neutrally buoyant condition. Equation (4.6) can be considered as the model equation. On the right hand side, $\dot{u}$ represents the hydrodynamic pressure for this whole "sphere" with the transient layer around the sphere, and the second term represents the viscous force or drag force. Now the expression for horizontal motion is only be controlled by one parameter: a combination of C_D and C_a. This will make it efficient for the operation of the simulations.

For the motion in Z direction, the control equation is different due to gravity and buoyancy. We have to consider the hydrostatic buoyancy force combined with gravity as a restoring force. We still use equation (4.3) and adding the restoring term, we get:

$$m\dot{W} = \rho V\dot{w} + \rho C_a V(\dot{w} - \dot{W}) + \frac{1}{2}\rho C_D A(w - W)|w - W| - N^2\rho V(Z - \tilde{Z}_0) \tag{4.7}$$

The first three terms are the same as the horizontal equation, and the last term is a combination of buoyancy and gravity written in form of buoyancy frequency

N=$\sqrt{-\frac{g}{\rho_0}\frac{d\rho}{dz}}$. However, the buoyancy term we add is sensitive to the neuturally buoyant condition, which means it also works when the sphere is not at its equilibrium depth. As the internal wave propagates, the fluid will have a vertical motion, which means the isopycnal where the sphere sit also moves up and down. So the initial depth will have a correction as $\tilde{Z}_0$=$Z_0 + z$ where z=$A\frac{k_x}{k_z}\sin(k_z Z_0)\cos(k_x X - \omega t)$ represents the vertical motion of the isopycnal. Through rearrangement we can get:

$$\dot{W} = \dot{w} + \frac{1}{m(1+C_a)}(\frac{1}{2}\rho C_D A(u-U)|u-U| - N^2\rho V(Z-\tilde{Z}_0)) \tag{4.8}$$

With the buoyancy term, the motion of the sphere in vertical will be similar to the fluid parcels. In our experiment, we can see that at low frequencies, there is some other component that makes the motion not monochromatic, which we need to test in the simulation.

4.1.2 Vfgen

Vfgen is a software that generates code for numerical ordinary differential equation (ODE) solvers [Weckesser, 2003], and we use it to solve the dynamic equations (4.6) and (4.8). The ODE solver code is produced with a given programming language through a vector field written in XML. Our ODE solver is based on the GNU Scientific Library.

4.2 Simulation Results

Figure 4.1 is a sample of the simulation output, the simulation has been run for 500s with ω=0.3 s^{-1}, left boundary has been set to be half cosine profile which is the same

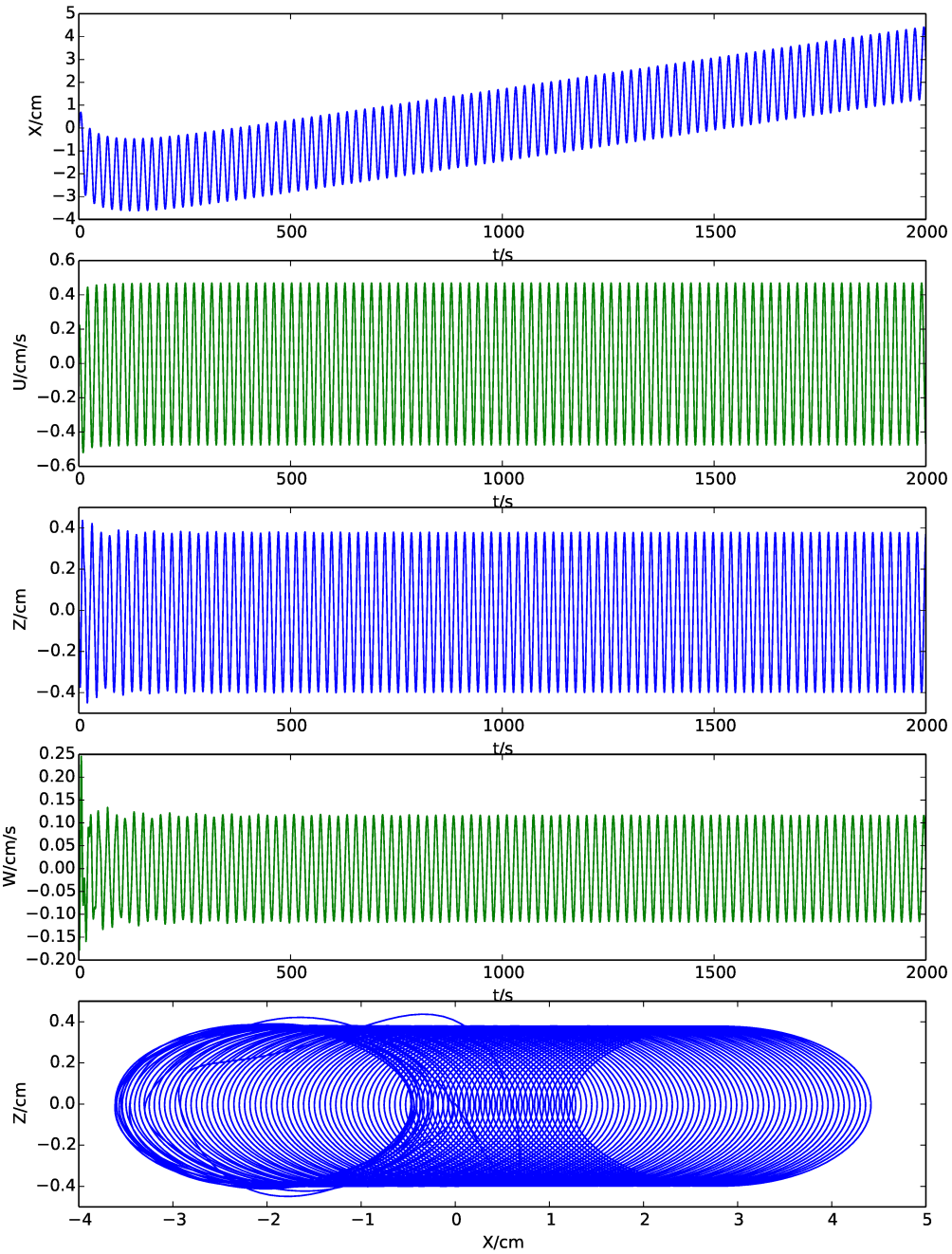

Figure 4.1: Simulation output with ω=0.3 s^{-1}, N=1.001 s^{-1}, Z_0=-11.0 cm

as our wave generator, and the fluid depth is 52.0 cm. The buoyancy frequency of the fluid has been set to be 1.001 s^{-1}. The sphere sits at Z_0=-11.0 cm and X_0=0 cm. We change the initial position X_0 to change the initial relative velocity U_{r0}, which we assume is effectively the same as adjust in initial phase in our experiments. The output file contains information on the path (X,Z) and the velocity (U,W) as a function of time.

4.2.1 Long Term Drift vs Transient Drift

As we can see from figure 4.1, for the horizontal position X, there is a bend around t=100 s where the sphere turned from a leftward drift to a rightward drift. Our experiments gather effective data works within the first 80s for higher frequencies, so the long term drift behaviour can not be recorded as we can not eliminate the reflected internal waves. Figure 4.2 shows the transient and the long term behaviour with different values of X_0, Z_0=-11.0 cm for all the simulations, ω=0.3 s^{-1} and N=1.001 s^{-1}. The initial velocity of the sphere is U_0=0 for every simulation, thus the relative velocity equals the initial velocity of the fluid parcels near the sphere, u_0. From figure 4.2, we find that the transient process is different with different initial conditions. The transient drift velocity is estimated by the green lines, the red lines represent the long term drift. This indicates that there is a stable long term drift for a certain frequency with the same drag and added mass coefficient regardless of the initial conditions. Similar results has been announced by Grotmaack and Meylan [2006] in a theoretical study of the surface wave drift. They studied a similar equation for small floating objects on the surface and conclude that there will be a long term drift velocity which

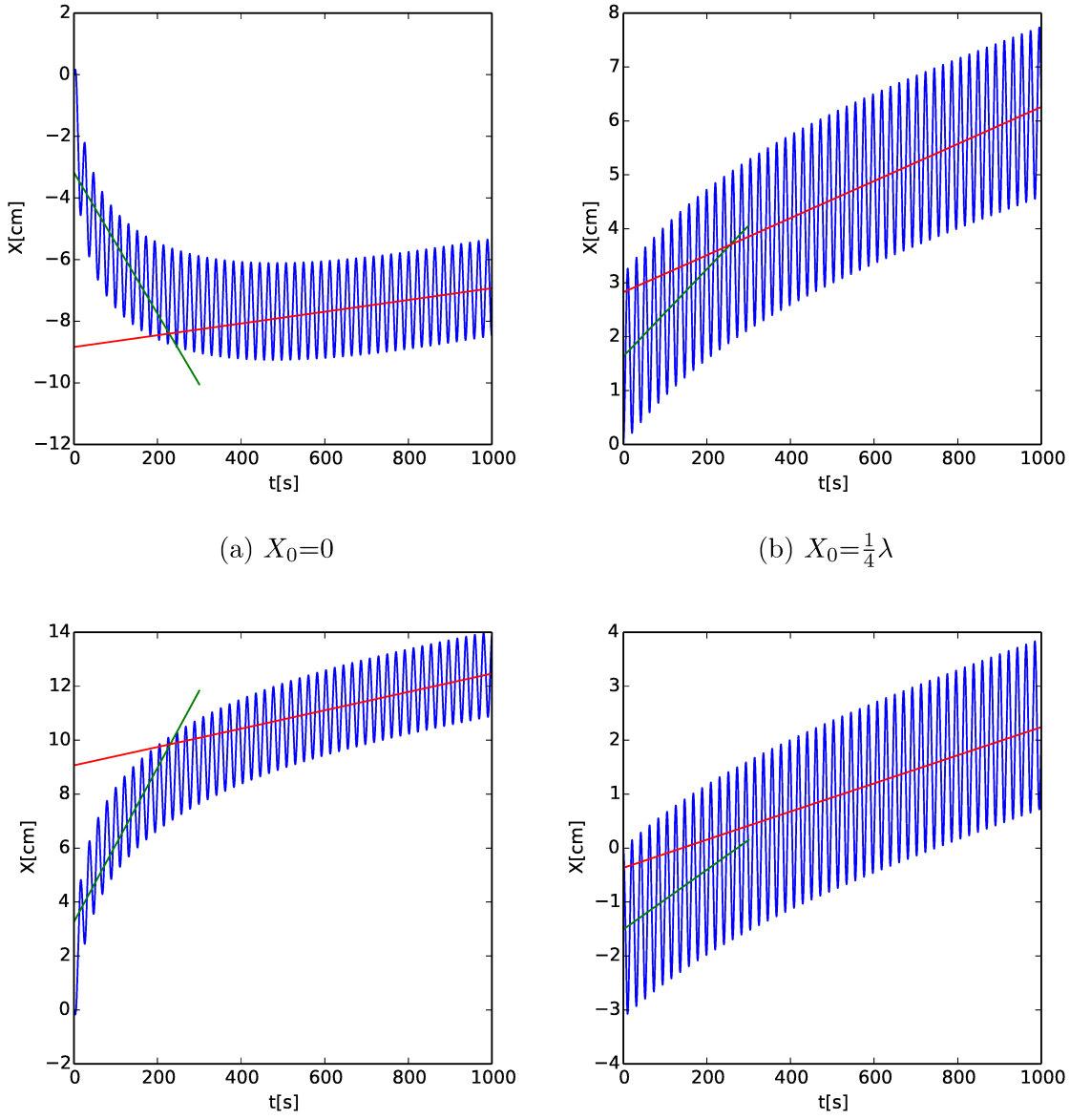

(a) X_0=0

(b) X_0=$\frac{1}{4}\lambda$

(c) X_0=$\frac{1}{2}\lambda$

(d) X_0=$\frac{3}{4}\lambda$

Figure 4.2: A long term drift u_d after an initial transient, λ is the internal wave wavelength

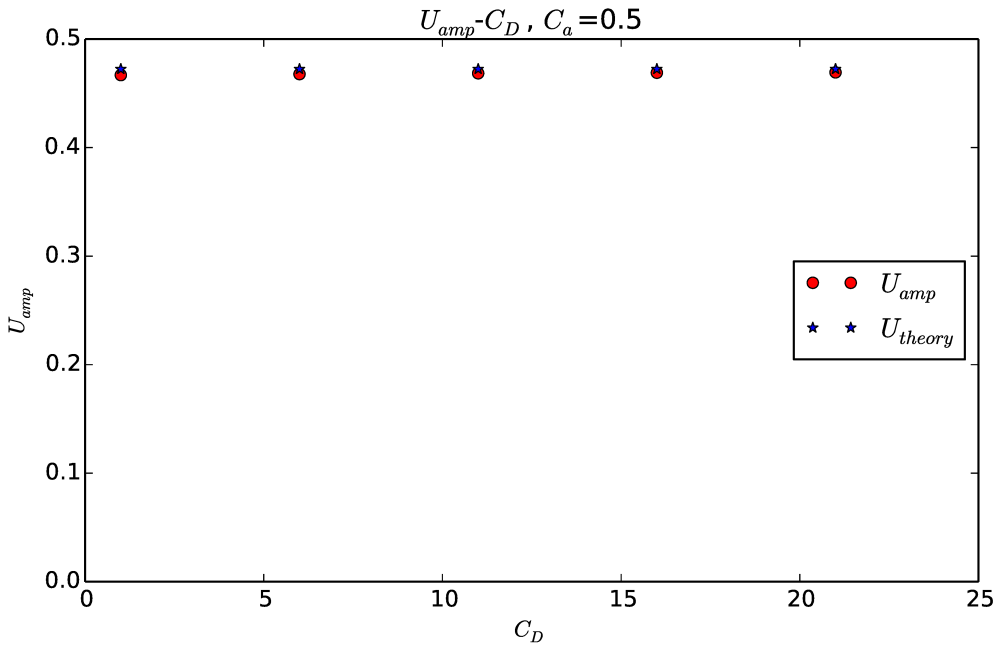

Figure 4.3: U_{amp} vs C_D with constant C_a

depends only on the drag coefficient. For internal waves where there is also vertical structure, this is 2 dimensional problem with a vertical consideration and the wave feature is strongly connected to the forcing frequency and the buoyancy frequency by the dispersion relation. The results are more complicated than for surface wave drift.

4.2.2 U_{amp} vs C_D&C_a

In equations (4.6) and (4.8), $\dot{u}$ and $\dot{w}$ are the internal wave field information and are prescribed, so the only parameter that controls the horizontal variation of U is the combined parameter $\frac{C_D}{1+C_a}$.

Figure 4.3 shows the simulation results of the velocity amplitude of the sphere plot versus C_D. C_a here is set to be a constant with value 0.5, which is the added

mass coefficient in homogeneous fluid, and ω=0.3 s^{-1}, N=1.001 s^{-1}. Thus the value of the combined parameter is controlled by the change of C_D. From figure 4.3 we can see the velocity amplitude of the sphere U_{amp} remains the same as C_D changes, and the value of U_{amp} is the same as the theoretical value U_{theory} which is the velocity amplitude of the fluid parcels. This result agrees with our experiments and shows the main behavior of the sphere is close to the fluid parcels around it. The invariance in value against C_D/C_a indicates that the major horizontal motion of the sphere is controlled by the hydrodynamic pressure term $\dot{u}$. The drift of the sphere is due to the drag term.

4.2.3 u_d vs C_D&C_a

The drift behaviour of the sphere, as a second order motion, is relatively small compared to the general motion of the sphere. As we introduced before, the model gives a long term drift as well as a transient. Our experiments can only show the existence of the transient, which is comparable with the simulation in the transient process in the first few wave periods. For the experimental transient drift, the direction and the value of u_d can be approached though the adjustment of phase and initial velocity in the simulation. The long term drift velocity u_d is another important feature for the sphere, the drift motion usually turns to be stable after ten wave periods. The drift results from the existence of the drag force, and the relation of the drift velocity and C_D along with C_a need to be studied form the model.

Figure 4.4 shows a the transient drift velocity which is within the first 80 s of the motion and the long term drift velocity which is evaluated after 500 s of the motion as

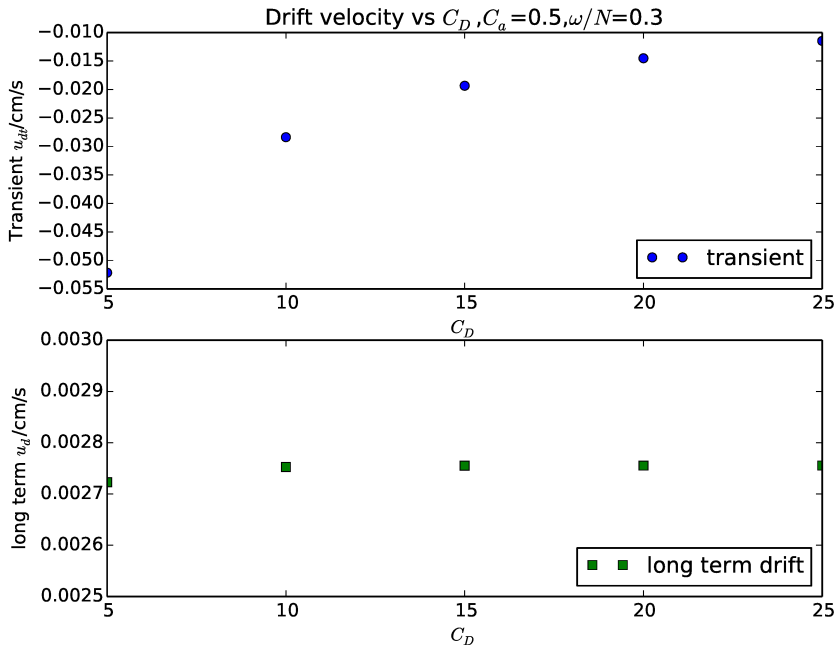

Figure 4.4: u_d vs C_D/C_a

a function of C_D. In all simulations, C_a has been set to 0.5, ω=0.3 s^{-1}, N=1.001 s^{-1}, Z_0=-11.0 cm and X_0=0. As we set C_a to be constant, the change in C_D represents the parameter $\frac{C_D}{1+C_a}$. We use 80 s for the transient process is to keep consistent with our lab experiment. The long term u_d is evaluated with the path data after 500 s when most simulations has finished the transient process. Every simulation has been run for 2000 s and the drift velocity has been evaluated using a linear fit. From figure 4.4, the transient drift velocity u_{dt} shows a strong dependence on C_D, the absolute value of u_{dt} is decreasing as C_D increase. While the long term drift velocity u_d appears to be different from u_{dt}, the long term drift velocity u_d is also related to C_D but the variation in value of u_d is small. Both u_d and u_{dt} show non-linearity in C_D as the control equation (4.6) is non-linear.

From the simulation results, the long term drift velocity u_d depends weakly on C_D at a constant frequency ω, as C_D increase from 5 to 25 by 400%, u_d increased by 6%. The dependence of u_d on $\frac{C_D}{1+C_a}$ is not strong. For the transient drift velocity u_{dt}, the dependence on $\frac{C_D}{1+C_a}$ is much stronger as the value decreased by 67.2% with the same change in C_D. The transient time has a non-linear relation with $\frac{C_D}{1+C_a}$; for smaller $\frac{C_D}{1+C_a}$, the transient will last for a long time.

4.2.4 u_d vs ω&ϕ

From the previous section we have some knowledge of the role that the parameter $\frac{C_D}{1+C_a}$ plays in the simulation. We are more interested in the relation of drift and the characteristic of internal waves, ω/N and the initial velocity or the phase(ϕ) in our experiments.

As introduced in Chapter 1, an internal wave only propagates when $\omega/N < 1$, and the wave structure is determined by ω/N as well. In our experiment and numerical simulations, the vertical wave number is set by the shape of the wave generator and is fixed at $k_z=\frac{\pi}{H}$=0.0604 cm^{-1}, where H=52.0 cm is the height. The dispersion relation will determine the horizontal wave number.

Ermanyuk and Gavrilov [2003] did experiments to measure the force on a sphere oscillating in a stratified fluid. They observed that the drag coefficient C_D and added mass coefficient C_a depend on ω/N. This is of vital importance to our problem as the transient drift is strongly connected with the parameter $\frac{C_D}{1+C_a}$. Their observation gives a increased value of C_D and a decreased value in C_a with ω/N in the range[0,0.5]. We don't have a specific formula for $C_D(\frac{\omega}{N})$ and $C_a(\frac{\omega}{N})$, but it is important to make such

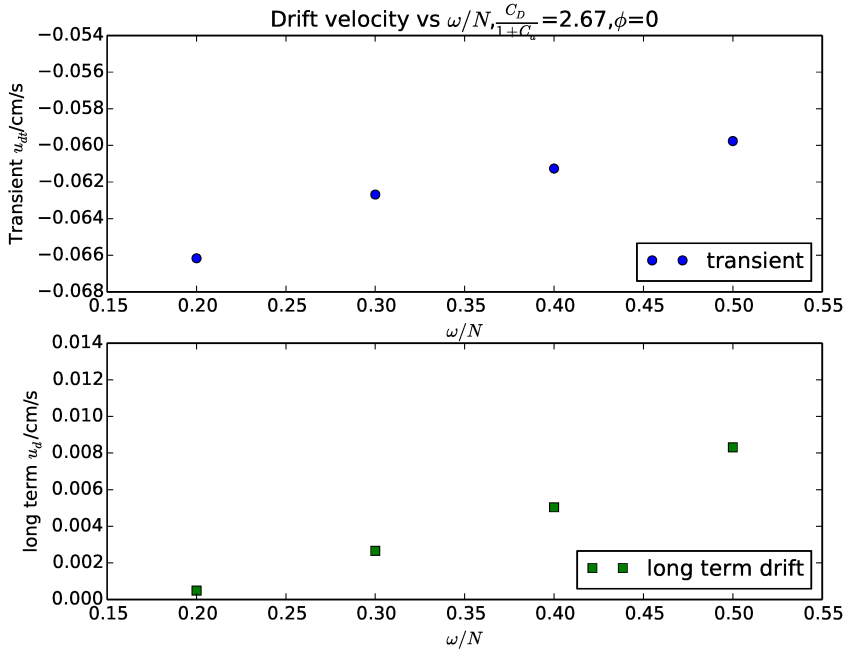

Figure 4.5: u_d vs ω/N with $\frac{C_D}{1+C_a}$=2.67, X_0=0

considerations when matching the model with our experiments. In the simulations to test the relation of u_d to ω/N, we use constant C_D=4 and C_a=0.5, thus the control parameter $\frac{C_D}{1+C_a}$=2.67 remain the same. The sphere sits at X_0=0 and Z_0=-11.0 cm. The simulation results, is shown in figure 4.5, contains both the transient drift velocity u_{dt} and the long term drift u_d. u_{dt} is evaluated in the first 50 s and u_d from behind 1000 s. The total length of each simulation is 3000 s.

Several $X - t$ plots of the simulation is shown in 4.7, with all the spheres start at X_0=0. From figure 4.5 we can see that the long term drift velocity u_d increases in absolute value with the increase of ω/N and the transient drift velocity decreases in absolute value with the increase of ω/N. It is clearly shown in figure 4.7 that the transient time varies sharply with different ω/N, and a higher ratio of ω/N occupies

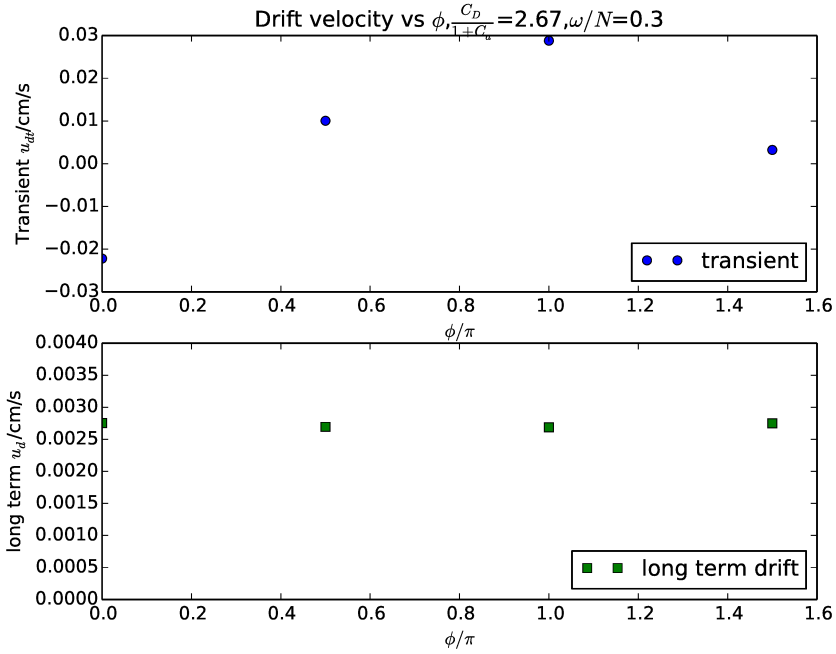

Figure 4.6: u_d vs ϕ with $\frac{C_D}{1+C_a}$=2.67, ω/N=0.3

a shorter transient time. The reliability of evaluating u_{dt} with a linear fit may not be a solid method due to the duration of the transient. On the other side, a increasing trend in u_d on ω/N is also displayed in figure 4.5. We already show in the former section that, the magnitude difference in u_d is 10^{-5} cm/s with the change of $\frac{C_D}{1+C_a}$, while for the variation of ω/N, the magnitude change is 10^{-3} cm/s. Apparently u_d is more sensitive to ω/N than C_D.

Figure 4.6 plots drift versus ϕ which is calculated through different initial position X_0 with ϕ=$\frac{X_0}{\lambda}\pi$, where λ is the horizontal wavelength of the internal wave, ω/N=0.3, C_D=4 and C_a=0.5. As shown in figure 4.2, different values of ϕ will lead to a different initial drift. Properties of the transient process show a great dependence on ϕ. There is a similar distribution of both the transient u_{dt} and the long term u_d against ϕ,

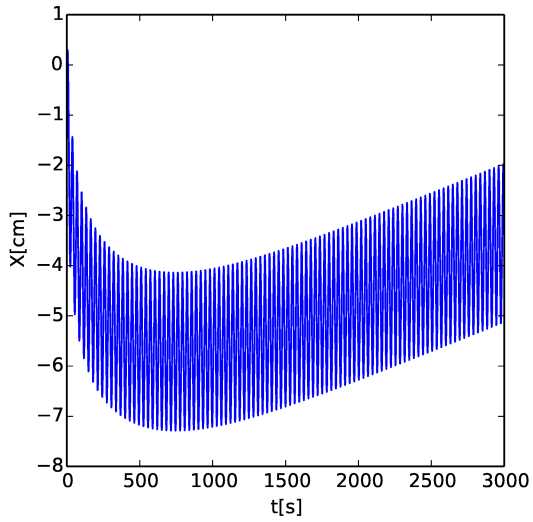

(a) ω/N=0.2

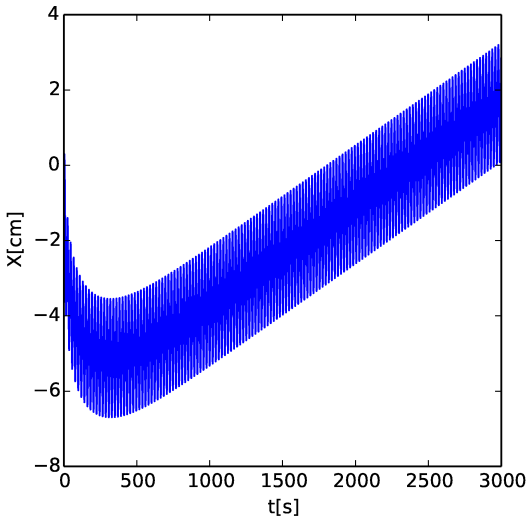

(b) ω/N=0.3

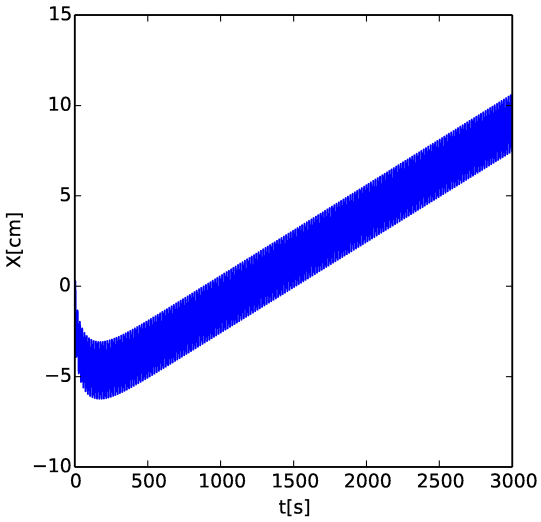

(c) ω/N=0.4

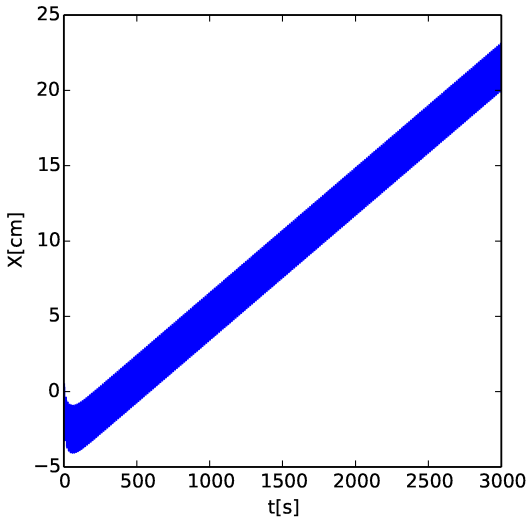

(d) ω/N=0.5

Figure 4.7: X-t with different values of ω/N, $\frac{C_D}{1+C_a}$=4, X_0=0

but the value differs a lot in these two situations. u_{dt} is bouncing between negative and positive values with ϕ, which is similar to figure 3.6 in our experiments, with some phase shift $\delta\phi$. For the long term drift u_d, the bouncing range in absolute value is within 10^{-5} of magnitude, which is negligible compare to the variation caused by frequency change.

4.2.5 Summary of Drift Motion

From the analysis above we can get a clear view of the horizontal drift and its dependence on many parameters. The drift is generated from the non-linearity of the control equation (4.6), especially the drag term. There is a transient process for horizontal motion of the sphere in the internal wave field, Both the transient drift velocity u_{dt} and the long term drift velocity u_d need to be considered.

The initial motion of the sphere is a transient process. It is affected by many parameters, including ω/N, the initial relative velocity represent by initial phase ϕ or the initial position X_0 and the empirical coefficients C_D and C_a. u_{dt} is sensitive to these parameters as seen in the simulation. From the limited duration of our experiments, the data only shows the behavior of the sphere in the transient, which confirms the existence of the initial condition problem in the transient. The comparison of model and experiment results will be done later.

The long term drift velocity u_d depends strongly on ω/N. According to Grotmaack and Meylan [2006], there will be a transient and a long term drift in surface wave drift. The long term drift should be along the wave propagation direction and only affected by C_D and C_a. Our simulation shows that the internal wave drift has some

similarities with the surface wave drift: they both drift to the propagating direction of the wave. In a propagating mode-1 internal wave, c_g and c_p are both related to ω/N by the dispersion relation, and this may lead to a stronger dependence of the long term drift u_d on frequency. Although the initial conditions and empirical coefficients also lead to a variation in u_d, their effects are not as strong as ω/N.

4.2.6 Vertical Motion of the Sphere

Figures 4.8 and 4.9 represent the vertical motion of a sphere with ω=0.3 s^{-1} and ω=0.5 s^{-1}, N is 1.001 s^{-1} for both simulations. The sphere is set initially to be at (X,Z)=(0,-11) cm, and C_D=4, C_a=0.5. We apply Fourier analysis to both Z and W, and the result has been plotted as labeled. In the $Z-t$ graph, the theoretical vertical displacement of the fluid has been marked out with a green line. The $X-Z$ path is showing the spacial information for each simulation.

The sphere can not move far from its neutrally buoyant depth, which means besides the hydrodynamic forces included for horizontal motion, we have a vertical restoring force with the buoyancy frequency N. From Figures 4.8 and 4.9, the vertical displacement amplitude is consistent with the theoretical value of the fluid parcels, for both frequencies, which again shows that the neutrally buoyant spheres have similar major features of motion as the fluid parcel at the same depth. But the vertical path in the transient process is more complicated compared to the horizontal motion. The excess displacement of Z beyond the amplitude limit represents the sphere motion beyond the fluid parcels at the same depth. This indicates the sphere has moved off its isopycnal and buoyancy force starts to drag the sphere back to the equilibrium

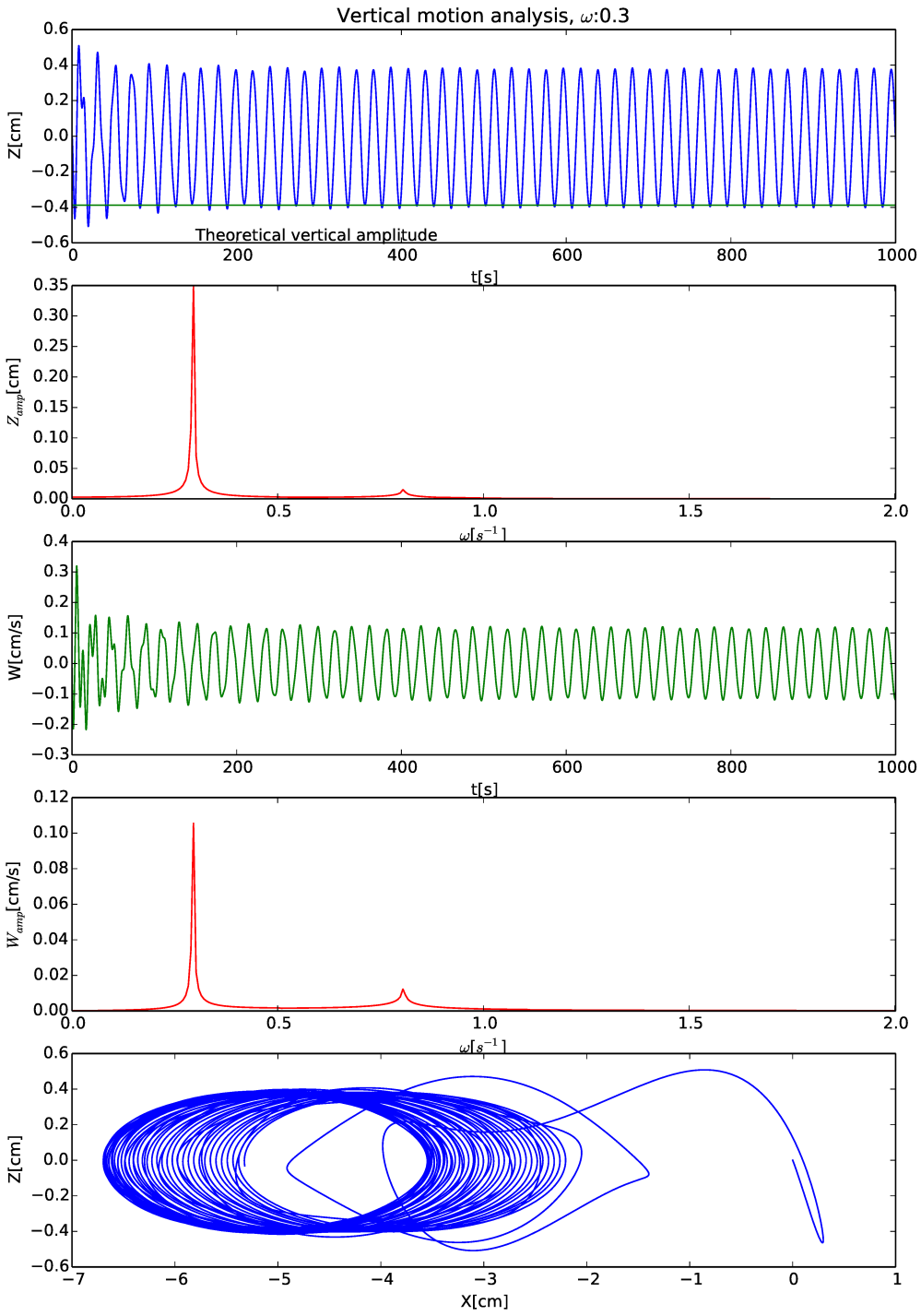

Figure 4.8: Vertical motion information: ω=0.3 s^{-1}

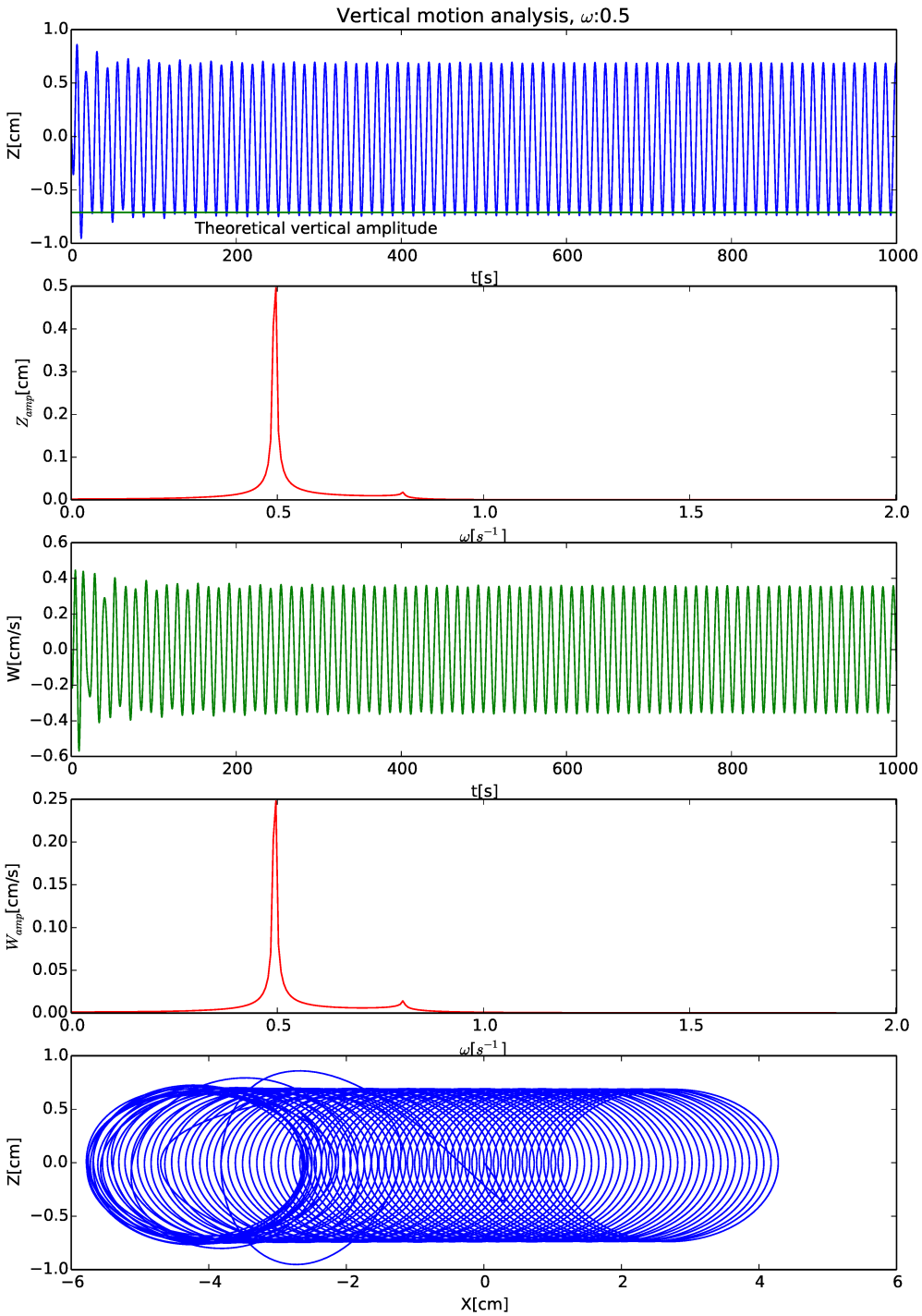

Figure 4.9: Vertical motion information: ω=0.5 s^{-1}

position. Such phenomena are more obvious at low frequencies. The vertical path is not as monotonous sinusoidal as the horizontal path. The path is quasi-periodic and irregular. This is the same for the vertical velocity W.

From the Fourier analysis of Z and W in figures 4.8 and 4.9, there exists a second dominate frequency in the spectrum around $\omega \approx 0.8$ s^{-1} for both frequencies. This second frequency has a stronger signal for lower frequencies. This shows that at lower frequencies, the buoyancy and gravity force are more dominant than at higher frequencies. The irregularity in the vertical displacement is also seen in our experimental data at lower frequencies, but for the limited duration of experiments we are not able to apply Fourier analysis to get amplitude information. In the spectral analysis, we did not see an apparent second dominate frequency above the noise of the data. Given a longer experiment the effect of the buoyancy and gravity force should be observable in the vertical motion of the sphere.

The existence of buoyancy and gravity forces in vertical direction as well as the hydrodynamic forces make the vertical motion of the sphere more complicated than the horizontal one. They both depend on position and relative motion, but the major vertical motion can be described by equation 4.8 as we can see the vertical displacement and velocity are all close to the the theoretical prediction as well as the experimental results.

Chapter 5

Discussion and Conclusions

In the previous chapters, we present experimental results and a numerical study of the internal wave induced drift of neutrally buoyant spheres. In this chapter we are going to discuss more details for both of them. And finally try to get a empirical law for the internal wave drift with the necessary parameters. Thus we can estimate the drift of neutrally buoyant vehicles in the internal wave field with similar scales.

5.1 Discussion

5.1.1 Internal Wave drift versus Surface Wave Drift

The drift behaviour of floating objects has been studied in the past 10 years both theoretically and experimentally. It is a one-dimensional problem and has a relatively complete system equations. The surface wave drift also need to consider the inertial force and the drag force, but as the object that have been used in the experiment and simulation are all very tiny, many assumptions have been made to simplify the

problem. Through theoretical analysis, a transient process and a long term drift exists in the surface wave drift [Grotmaack and Meylan, 2006]. And the experiments done by Huang and Huang [2011] also show that different shapes of objects will have different drift velocities. There is no well agreed upon expression for the surface wave drift velocity as the drift depend on wave heights and the drag coefficients.

For internal waves, the vertical and horizontal scale of the wave is larger than the sphere we use, so it still can be described as small scale objects drifting in internal waves. The internal wave field in our study has a 2-D structure, whether the additional vertical dimension will have an effect on the drift motion or not is a question needs to be answered. And the difference in the empirical coefficients may also have a effect on the drift. The simulation results show a transient drift and a long term drift for the internal wave drift as well.

5.1.2 Comparison of Experiment and Simulation

5.1.2.1 Difference in Internal Wave Field and Phase Correction

In our experiment, the internal wave is propagating from the wave generator to the right end of the tank, and encounter the sphere after distance X_0. When the wave generator is started, the motor needs some time to accelerate, and we may have some error at the initial velocity of the fluid parcel u_0. But as the acceleration time is pretty short (within 1s), so the wave field will become uniform after a quarter wave period, which may have a little effect on ϕ=0 or π where u_0 is at maximum at time zero.

In our simulation, the internal wave field is prescribed over the whole domain, in

which the initial velocity of the fluid u_0 is set by the initial position X_0. There is no delay of u_0 in the simulation, which may cause difference in the first few seconds for the sphere motion.

To match the model and the experiment, one important thing is to match the phase problem, which is represented by ϕ in the experiment and X_0 in the simulation. In the experiment the wave generator is moving in a sine curve as $A\sin(\omega t)$ where A is the amplitude. We define the motion of the left boundary in the simulation as $u = \omega A\cos(k_z Z_0)\cos(k_x X_0 - \omega t)$, thus through an integral we get the horizontal displacement should be $A\cos(k_z Z_0)\sin(\omega t - k_x X_0)$. The way we define phase in simulation will give us negative phase. Thus, we need to adjust the phase to match the results. So the phase we use in the simulation are all negative phase, and the correction is $\phi_{experiment} = \phi_{simulation} \times (-1) + 2\pi$.

5.1.2.2 Transient in the Simulation

As limited by the length of our tank, the reflected waves will affect the motion of the sphere not long after the experiment starts. We only have a limited length of valid data for analysis. Through the analysis we observe a drift velocity which can be roughly described by equation (3.3), the drift of the sphere seems to depend both on ω and ϕ. But the simulation which we can have a long time series shows that in the first few wave periods, the sphere is just a transient process and after that there will be a long term drift as the wave propagates. This is similar to the surface wave drift which was theoretically analysed by Grotmaack and Meylan [2006].

Although the transient process is only a short term behaviour, we have observed it in our experiment and it is still valuable to compare the transient drift velocity

from the experiments and the simulations.

Another important feature of both the experimental and the numerical simulations is the dependence on the empirical coefficients C_a and C_D. These coefficients will be different under different conditions with the changes of non-dimension numbers such as the Reynolds number Re and the Richardson number Ri. Ermanyuk and Gavrilov [2003] measured the force on a sphere oscillating in a stratified fluid and gives their estimation of the added mass coefficient $C_\mu(C_a)$ and drag coefficient $C_\lambda(C_D)$. They observe a decrease in C_a and a increase in C_D in the range $0.2s^{-1} < \omega/N < 0.5s^{-1}$. Thus the combined coefficient in our simulation $\frac{C_D}{1+C_a}$ should have an increasing trend with ω/N. This may explain why in the experiments, the transient drift velocity u_{dt} is decreasing with ω/N in value.

The drag coefficients of small spheres settling in stratified fluid also have been studied [Yick and Torres, 2009], and they give the formula of C_D as a function of Re (to a moderate regime) and Ri:

$$C_D = (\frac{12}{Re} + \frac{6}{1+\sqrt{2Re}} + 0.4)(1 + 1.9Ri^{\frac{1}{2}}) \tag{5.1}$$

which gives a possibility that the drag coefficient can be affected by the stratification as well. Their study is focused on spheres with micrometers of diameter, which will be different from ours, but the change in C_D is important in both situations.

The added mass coefficient C_a is also a very important difference in the experiments and simulations. C_a depends on size of the objects, for very small objects the added mass effect can be neglected. But for our experiments, the sphere is 4 cm in diameter, so C_a will be important for the motion of the sphere. In the model we use C_a=0.5, which is the added mass coefficient of a sphere in homogeneous fluid. For

the sphere in a stratified fluid as well as an internal wave field, only empirically C_a need to be determined by the experiments and the simulation.

The transient process of the sphere is not stable and this makes it hard to evaluate the coefficients from our experiments. Although to get C_a and C_D by comparing the results from the experiments and the simulations will not be accurate, we can still show the correct coefficients will give us a relatively accurate estimate about the motion of the sphere.

Figure 5.1a gives us the transient drift information from the simulation with different values of combined parameter. We can compare figure 5.1 with experimental data of figure 3.5 in chapter 4 where the sphere is at the same depth. The decreasing trend with ω can be created with the chosen of C_D and C_a in Table 5.1. Figure 5.1b plots transient drift velocity u_{dt} versus corrected ϕ from the simulation. The phase in this figure is consistent with our experiment. We also can see a sine curve distribution of u_{dt} on ϕ, but compared to figure 3.6, we can observe a obvious phase shift of the curve. This might be caused by the dispersion of the internal wave as the wave propagates. The difference in group velocity c_g and phase velocity c_p will change the phase information of the leading wave edge when the internal wave reach the sphere. The empirical coefficients in table 5.1 is just a guess for the simulation results to get close to the experiments. It is clear in figure 5.1a that at high ω/N, u_{dt} is tending to become positive (considering the points where ϕ=0), so the transient process may come to an end earlier than at lower frequencies. The uncertainties in u_{dt} are larger for the transient process since it is not stable in time; u_{dt} should be a function of time and finally approach the long term drift velocity u_d for all initial conditions.

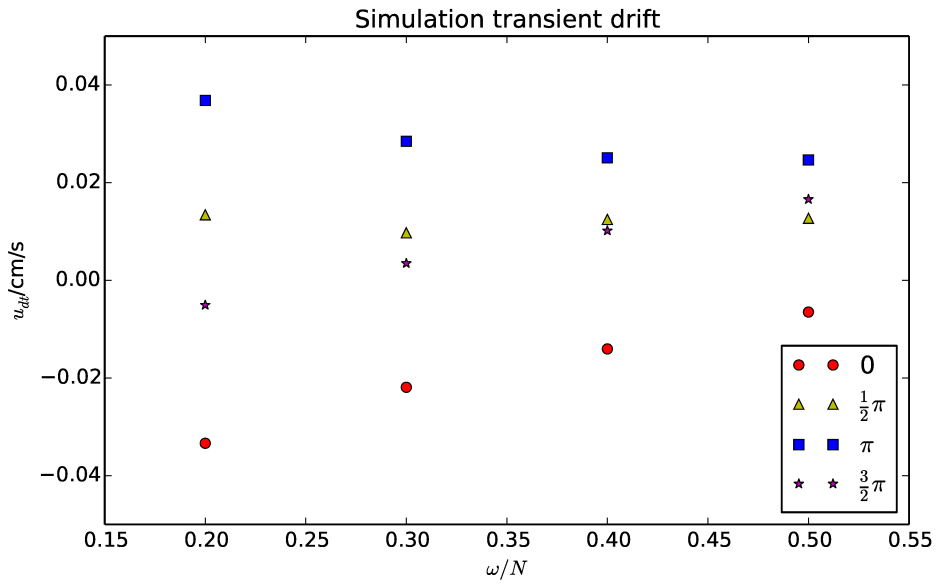

(a) Transient drift velocity vs ω/N

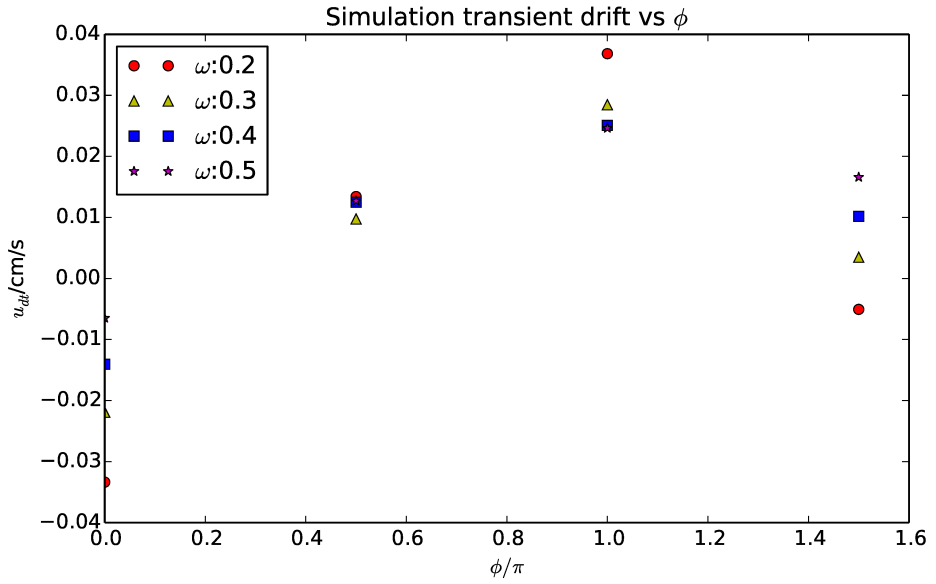

(b) Transient drift velocity vs ϕ

Figure 5.1: Simulation results with different $\frac{C_D}{1+C_a}$ for ω/N at Z_0=-11.0 cm

Table 5.1: Empirical coefficients for ω/N in simulations

$\omega(s^{-1})$	N(s^{-1})	C_D	C_a	$\frac{C_D}{1=C_a}$
0.2	1.0	11	0.5	7.3
0.3	1.0	13	0.5	8.7
0.4	1.0	15	0.5	10
0.5	1.0	17	0.5	11.3

5.1.2.3 Long Term Drift

Compared to the transient drift, the long term drift is a more valuable result from the numerical simulation. Unfortunately our experiment is unable to record the long term drift behaviour, so the result can only be evaluated from the numerical model. In Chapter 4, we analysed the effect of all the parameters on the long term drift velocity in a mode-1 wave. And the conclusion is that the long term drift u_d is mainly affected by the frequency of the internal wave. Although changing in initial conditions and drag coefficient can also lead to a variation in u_d, the magnitude of change can not compare to the change caused by changing ω/N.

Figure 5.2 shows u_d plotted versus ω/N from our simulation, the initial condition problem has a little effect at lower frequencies but at higher frequencies they show great consistency. To determine the dependence of u_d on ω/N, we divide u_d by the horizontal velocity amplitude U_{amp}=$\omega A\cos(k_z Z_0)$, which we believe that u_d should be proportional to U_{amp}, and plot again versus ω/N. As shown in figure 5.3, we see a pretty linear trend. It is possible that the expression $\frac{u_d}{U_amp}$ might be linear in frequency. If we do a linear fit for the data we have, we get the slope of the fit curve

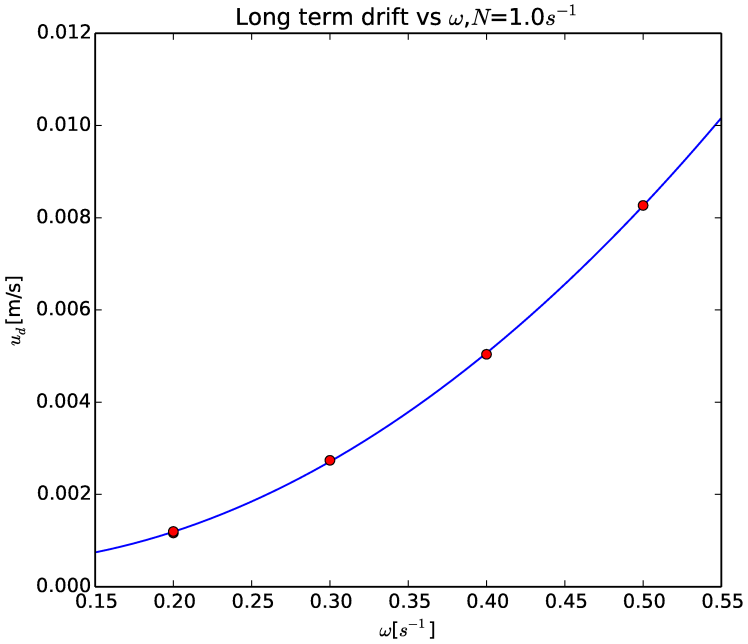

Figure 5.2: Simulated long term drift versus ω at Z_0=-11 cm

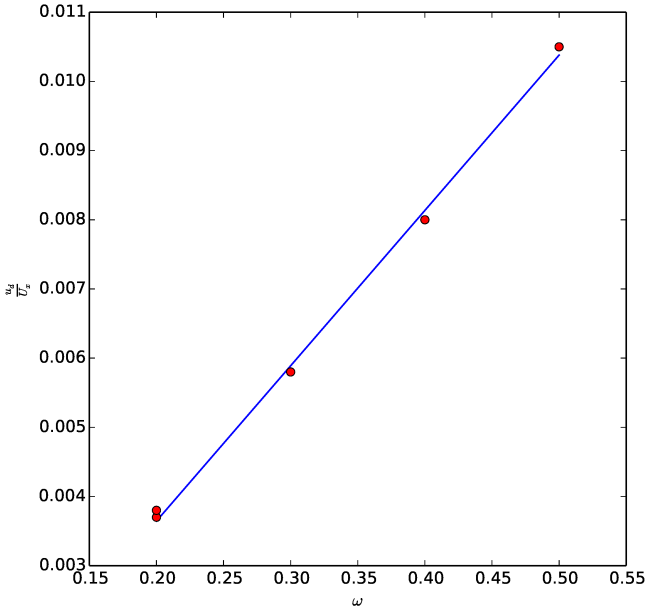

Figure 5.3: $\frac{u_d}{U_{amp}}$versus ω at Z_0=-11 cm

is s=2.24×10^{-2} with an intercept b=-8×10^{-4}. Thus an empirical expression for u_d can be written as:

$$u_d = (C\omega + B)U_{amp} \tag{5.2}$$

If we substitute the expression for U_{amp} and with the assumption that $B \ll C$, we will get a more simple expression for figure 5.2 as:

$$u_d = C\omega^2\tilde{A} \tag{5.3}$$

where $\tilde{A}$ represents the true amplitude which equals to $A\cos(k_z Z_0)$. The dependence on N in equation (5.3) is not obvious as the expression of U_{amp} does not contain N, and in our simulations we set N=1.0s^{-1} for simplification. We are not quite sure whether ω/N or N should act as the variable. But as u_d is strongly related to U_{amp}, we propose equation 5.3 as the empirical estimation for a long term drift velocity of a neutrally buoyant sphere in a mode-1 internal waves.

5.2 Conclusion

In this thesis, we introduced the basic equations about autonomous underwater vehicles and internal waves, including the mechanism of internal waves and the hydrodynamic motion equations of the AUV. To understand an impact of the internal wave field on AUV motion, we choose to study a neutrally buoyant sphere motion in a mode-1 internal wave field.

In the experimental study, we used a 5m long tank and a wave generator to generate a rightward propagating internal wave field, but the reflected waves from the end wall led to a limited length of valid data. Through analysis we found the internal

wave drift phenomena, which was related to many parameters about the internal wave field. For a further understanding of the internal wave drift problem, we apply numerical simulations to the motion of the sphere. To describe the sphere's motion in stratified fluids with internal waves, we use Morison's equation for moving objects in fluid to estimate the hydrodynamic forces on the sphere. Morison's equation is a semi-empirical formula including the added mass coefficient and drag coefficient which are both determined empirically. Using figure out the correct values of these coefficients for the equation is important to describe the motion of the sphere accurately. Through the simulation results, we discovered that the sphere is moving similarly to the fluid parcel at the same location, since there is a transient process which depends on the initial condition of the internal wave field. After the transient, the motion of the sphere is only related to the frequency of the internal waves, as the impact of empirical coefficients and initial conditions are limited compared to the frequency.

With the analysis of the long term drift velocity, we finally get an empirical equation, which the long term drift velocity u_d is connected with the frequency of the internal wave ω and the horizontal velocity maximum value U_{amp}. For a mode-1 internal wave, these two values also have a relation. The final estimation of u_d is given by equation (5.3). Given a spherical AUV of neutrally buoyant in stratified fluid, with a mode-1 internal wave propagating with ω=0.2s^{-1} and an amplitude A=100 m, the velocity amplitude will be U_{amp}=20 m/s, then the estimated drift velocity after the transient will be $u_d = C\omega^2 A$=$0.0224 \times 0.2^2 \times 100$=0.096m/s ≈10 cm/s, and the AUV is drifting in the direction of the internal wave propagates. This mean drift speed is comparable to typical currenty speeds at depth. The internal wave drift is a measurable effect but in operation, an AUV with a thruster would be able to compensate

for this drift at a voyage speed of 2 m/s.

Bibliography

J. C. B.Curtin, Denise M.Crimmins. Autonomous underwater vehicles:trends and transformations. *Marine Technology Society Journal*, pages 65–75, 2005.

B. Cushman-Roisin and J. M. Beckers. *Introduction to Geophysics Fluid Dynamics*. Academic Press Publication, second edition, 2011.

E. V. Ermanyuk and N. V. Gavrilov. Force on a body in a continuously stratified fluid. part 2. sphere. *Journal of Fluid Mechanics*, pages 33–50, 2003.

T. I. Fossen. *Marine Craft Hydrodynamics and Motion Control*. A John Wiley&Sons, Ltd. Publication, first edition, 2011.

C. Garrett and W. Munk. Internal waves in the ocean. *Annu. Rev. Fluid Mech*, pages 339–369, 1979.

R. Grotmaack and M. H. Meylan. Wave forcing of small floating bodies. *Journal of waterway, port, coastal, and ocean engineering*, pages 192–198, 2006.

G. Huang and Z. Huang. Wave-induced drift of small floating objects in regular waves. *Ocean Engineering*, pages 712–718, 2011.

K. W. Ivey and J. Koseff. Density stratication, turbulence, but how much mixing? *Annual Review of Fluid Mechanic*, pages 169–184, 2008.

W. K. Mark Sibenac, Tarun Podder and H. Thomas. Autonomous underwater vehicles for ocean research: Current needs and stater of the art technologies. *Marine Technology Society Journal*, pages 63–72, 2004.

M. J. Mercier, D. Martinand, M. Mathur, L. Gostiaux, T. Peacock, and T. Dauxois. New wave generation. *Journal of Fluid Mechanics*, 657:308–334, 2010.

M. Nahon. A simplified dynamics model for autonomous underwater vehicles. In *Proceedings of Symposium on Autonomous Underwater Vehicle Technology*, 1996.

NASA. Drag in the fluid. `http://www.grc.nasa.gov/WWW/k-12/airplane/dragsphere.html`, 2010.

T. Sarpkaya. Force on a circular cylinder in viscous oscillatory flow at low keulegan-carpenter numbers. *Journal of Fluid Mechanics*, 165:61–71, 1986.

H. H. Shen and Y. Zhong. Theoretical study of drift of small rigid floating objects in wave fields. *Journal of waterway, port, coastal, and ocean engineering*, pages 343–351, 2001.

B. M. Sumer and J. Fredsoe. *Hydrodynamics Around Cylindrical Structures (Advanced Series on Ocean Engineering)*. World Scientific Pub Co Inc, revised edition, 2006.

B. Sutherland. *Internal Gravity Waves*. Cambridge University Press, first edition, 2010. ISBN 978-0-521-83915-0.

H. Sutherland.B.R, Dalziel.S.B and Linden.P.F. Visualization and measurement of internal waves by synthetic schlieren.part 1: Vertically oscillating cylinder. *Journal of Fluid Mechanics*, pages 93–126, 1999.

E. Talley, Pickard. Descriptive physical ocean: An introduction (6th ed.). *Elsevier, Oxford, U.K.*, 2011.

A. Techet. Hydrodynamics: Added Mass. `http://ocw.mit.edu/courses/mechanical-engineerin` 2005. [Online; version 3.0 updated 8/30/2005].

W. Weckesser. Vfgen. `http://www.warrenweckesser.net/vfgen/`, 2003.

C. Wunsch and R. Ferrari. Vertical mixing, energy, and the general circulation of the oceans. *Annu. Rev. Fluid Mech*, pages 281–314, 2004.

K. Y. Yick and C. R. Torres. Enhanced drag of a sphere settling in a stratified fluid at small reynolds numbers. *J. Fluid Mech*, pages 49–68, 2009.

Appendix A

Appendix

A.1 Introduction to 6-DOF Equations

We use a 2D model to introduce the derivation of the mathematical model of the AUV motion equation, but the design and manufacture of an AUV always require a 3D model for more details.

We are going to do a review of the 6-DOF equations of the vehicles. For 6-DOF we have to consider the motion in surge, sway, heave, roll, pitch and yaw. Each degree of freedom has one control equation. If we still put the origin of the body reference frame in the gravity center and make the buoyancy center of the vehicle sits at the same point, the basic motion equations in vector form are

$$\sum \vec{F} = m\dot{\vec{x}} \tag{A.1}$$

and

$$\sum \vec{M} = I_{cm}\dot{\omega} + \omega \times I_{cm}\omega \tag{A.2}$$

which represents the translational and rotational motion controlled by Newton's 2nd

Law and Euler's equation, respectively. $\sum \vec{F}$ is the net external force on the vehicle,m is the mass of the vehicle and $\dot{\vec{x}}$ is the acceleration for the center of gravity of the vehicle in the body-fixed frame and I_{cm} and $\sum \vec{M}$ are the moment of inertia tensor of the vehicle and the net external moment acting on the vehicle. They are all related to the center of gravity of the vehicle. ω is the angular velocity of the vehicle body in the body fixed reference frame.

We have 6 equations with 9 unknowns in the equation above for velocity vector $[u, v, w, p, q, r]^T$ which the former three represents translational velocity and the latter represents angular velocity, and we also have 3 unknowns about the euler angles (θ, ϕ, φ) of each axis in the body-fixed reference frame. The kinematic relations of a rigid body must be considered in the form of a relationship between angular rates $[p, q, r]^T$ and the time rate change of the Euler angles which is given by [Nahon, 1996]

$$\dot{\phi} = p + (\sin\phi \tan\theta)q + (\cos\phi \tan\theta)r \tag{A.3}$$

$$\dot{\theta} = (\cos\phi)q - (\sin\phi)r \tag{A.4}$$

$$\dot{\varphi} = (\sin\phi \sec\theta)q + (\cos\phi \sec\theta)r \tag{A.5}$$

Through all the equations above we can solve for the velocity vector $[u, v, w, p, q, r]^T$ in body fixed reference frame, to get the position information in the earth fixed frame, we need a transformation of the velocity vector in this two coordinator systems, so we need the transformation matrix, to multiply the velocity vector by the matrix we can get the derivatives of the position vector, and through integral, we could get the vector$[\dot{x}, \dot{y}, \dot{z}, \dot{\theta}, \dot{\phi}, \dot{\varphi}]^T$ in the inertial reference frame. The transformation matrix

Nahon [1996] is given by T:

$$T = \begin{vmatrix} T_1 & 0_{3\times3} \\ 0_{3\times3} & T_2 \end{vmatrix} \tag{A.6}$$

$$T_1 = \begin{vmatrix} c\varphi c\theta & -s\varphi c\phi + c\varphi s\theta s\phi & s\varphi s\phi + c\varphi c\phi s\theta \\ s\varphi c\theta & c\varphi c\phi + s\phi s\phi s\theta & -c\varphi s\phi + s\varphi s\theta s\phi \\ -s\theta & c\theta s\phi & c\theta c\phi \end{vmatrix} \tag{A.7}$$

$$T_2 = \begin{vmatrix} 1 & s\phi t\theta & c\phi t\theta \\ 0 & c\phi & -s\phi \\ 0 & s\phi/c\theta & c\phi/c\theta \end{vmatrix} \tag{A.8}$$

In which $s \equiv \sin$, $c \equiv \cos$ and $t \equiv \tan$.

With the transformation

$$[\dot{x}, \dot{y}, \dot{z}, \dot{\theta}, \dot{\phi}, \dot{\varphi}]^T = T[u, v, w, p, q, r]^T \tag{A.9}$$

we are able to obtain the velocity vector of the vehicle in the inertial reference frame. We can integrate the velocity to get the translational position of the vehicle's gravity center. The Euler angles can offer the information for the vehicle's orientation, then we have the information we need for the vehicle in the inertial reference frame. The hydrodynamic force would be calculated in the similar way as in the 2D scenario.

A.2 Added Mass Coefficient in 6-DOF Equation

Here will be a brief introduction on the added mass coefficient in the 6-DOF motion equation of the AUV. The added mass force[Fossen, 2011] opposes the motion can be

added into an equation as:

$$m\ddot{x} + b\dot{x} + kx = F - m_a\ddot{x} \tag{A.10}$$

through rearrangement we can get:

$$(m + m_a)\ddot{x} + b\dot{x} + kx = F \tag{A.11}$$

Where m_a is the added mass coefficient in 1-D motion. Equation 1.24, can be unified to be one general equation, first we define the generalized velocity vector:$\vec{v} = [u, v, w, p, q, r]^T$, and use τ for all the external moments and forces.Fossen [2011]

$$M_{RB}\dot{\vec{v}} + C_{RB}(\vec{v})\vec{v} = \tau \tag{A.12}$$

where M_{RB} is the rigid-body system inertia matrix, $C_{RB}(v)$ is the Coriolis vector term because the vehicle itself is a rotation reference frame. In a 6-DOF equations, the matrix without the added mass is

$$M_{RB} = \begin{bmatrix} m & 0 & 0 & 0 & 0 & 0 \\ 0 & m & 0 & 0 & 0 & 0 \\ 0 & 0 & m & 0 & 0 & 0 \\ 0 & 0 & 0 & I_{xx} & 0 & -I_{xz} \\ 0 & 0 & 0 & 0 & I_{yy} & 0 \\ 0 & 0 & 0 & -I_{zx} & 0 & I_{zz} \end{bmatrix} \tag{A.13}$$

We already reduced many terms using symmetry of the vehicle to simplify the equations. For an arbitrary 6-degree freedom system, the mass tensor is a 6×6

matrix. A general form of the added mass effect would be

$$F = \begin{bmatrix} m_{11} & m_{12} & m_{13} & m_{14} & m_{15} & m_{16} \\ m_{21} & m_{22} & m_{23} & m_{24} & m_{25} & m_{26} \\ m_{31} & m_{32} & m_{33} & m_{34} & m_{35} & m_{36} \\ m_{41} & m_{42} & m_{43} & m_{44} & m_{45} & m_{46} \\ m_{51} & m_{52} & m_{53} & m_{54} & m_{55} & m_{56} \\ m_{61} & m_{62} & m_{63} & m_{64} & m_{65} & m_{66} \end{bmatrix} \begin{pmatrix} \dot{u_1} \\ \dot{u_2} \\ \dot{u_3} \\ \dot{u_4} \\ \dot{u_5} \\ \dot{u_6} \end{pmatrix} \tag{A.14}$$

where each component m_{ij} in the matrix represents the added mass force in ith direction due to the acceleration generated from jth direction. For instance if we take added mass into our equation A.14, then $m_{11} = m - X_{\dot{u}}$ instead of just m, the other terms of m_{ij} will not all be zero and the computation complexity will increase.

The value of these added mass coefficients depend on the shape of the vehicle. For a certain design of an AUV, a group of values will be measured accurately depending on its geometry and weight distribution. The accuracy of such values will be of vital importance to a vehicle for manufacture.

A.3 Motor Frequency Transformation

Table A.1: Motor frequency transformation

rpm	s^{-1}
200	0.1047
382	0.2
478	0.25
573	0.3
669	0.35
764	0.4
860	0.45
955	0.5
1051	0.55
1146	0.6